Improving Device Efficiencies in Organic Photovoltaics through the Manipulation of Device Architectures and the Development of Low-Bandgap Materials

Andrew Hideo Rice

A dissertation

submitted in partial fulfillment of the

requirements for the degree of

Doctor of Philosophy

University of Washington

2013

Reading Committee:

Professor Christine K. Luscombe, Chair

Professor Fumio S. Ohuchi

Professor Guozhong Cao

Program Authorized to Offer Degree:

Materials Science and Engineering

University of Washington

Abstract

Improving Device Efficiencies in Organic Photovoltaics through the Manipulation of Device Architectures and the Development of Low-Bandgap Materials

Andrew Hideo Rice

Chair of the Supervisory Committee:
Professor Christine K. Luscombe
Materials Science and Engineering

Over the past two decades, vast amounts of research have been conducted in the pursuit of suitable organic semiconductors to replace inorganic materials in electronic applications due to their advantages of being lightweight, flexible, and solution-processible. However, before organic photovoltaics (OPVs) can be truly competitive and commercially viable, their efficiencies must be improved significantly. In this examination, we pursue higher efficiency OPVs in two different ways. Our attempts focus on 1) altering the microstructure of devices to improve charge dissociation, charge transport, and our understanding of how these devices function, and 2) tailoring materials to achieve optimal band gaps and energy levels for use in organic electronics.

First, we demonstrate how the vertical morphology of bulk heterojunction (BHJ) solar cells, with an active layer consisting of self-assembled poly(3-hexylthiophene) (P3HT) nanowires and (6,6)-

phenyl C_{61}-butyric acid methyl ester (PCBM), can be beneficially influenced. Most device fabrication routes using similar materials employ an annealing step to influence active layer morphology, but this process can create an unfavorable phase migration where P3HT is driven toward the cathode. In contrast, we demonstrate devices that exhibit an increase in relative fullerene concentration at the top of the active layer by introducing the donor phase as a solid nanowire in the active layer solution and altering the pre-spin drying time. X-ray photoelectron spectroscopy (XPS) and conductive and photoconductive atomic force microscopy (cAFM and pcAFM) provide detailed information about how the surface of the active layer can be influenced; this is done by tracking the concentration and alignment of P3HT and PCBM domains. Using this new procedure, devices are made with power conversion efficiencies surpassing 2%. Additionally, we show that nanowires grown in the presence of the fullerene perform differently than those that are grown and mixed separately; exposure to the nanowire during self-assembly may allow the fullerene to coat nanowire surfaces and influence the photocurrent within the device. Furthermore, because we are able to carefully control the regioregularity of our P3HT, we are able to produce a series of nanowires with regioregularities ranging between 93% and 99%. X-ray diffraction (XRD) shows that as the regioregularity of the polymer increases, the coherent domain size along the long-axis of the nanowires also becomes larger. When organic field effect transistors (OFETs) are made from these materials, the hole mobility of the nanowire films also has a positive correlation with regioregularity. As the domains within the nanowires grow larger, the frequency of domain boundaries decreases, allowing charges to percolate more efficiently along the nanowire.

Additionally, we show that by introducing C_{60} into the active layer of P3HT:PCBM devices, we can modulate the crystal habit of the PCBM domains. Using optical microscopy and UV-vis

absorption spectroscopy, we demonstrate that C_{60} additions alter the crystal morphology and greatly reduce the size of fullerene crystallites that are observed after extended annealing times and under aggressive aging conditions. We also show by fabricating organic field-effect transistors (OFETs) from PCBM:C_{60} blends that the incorporation of C_{60} does not adversely affect the electron mobility in these films. Finally, we show that as C_{60} is incorporated into P3HT:PCBM OPVs, devices become more thermally stable and do not degrade in performance as rapidly as traditional P3HT:PCBM blends.

Lastly, the synthesis of four alternating copolymers using benzo[2,1-*b*;3,4-*b′*]dithiophene (BDP) as the common donor unit is presented. Incorporating BDP, which consists of fused dithiophene units with a benzene ring, into these polymers should produce a low-lying highest occupied molecular orbital (HOMO) energy level. Low-lying HOMO levels are desirable to produce high open circuit voltages (V_{OC}) in organic BHJ photovoltaic devices. The preliminary results of their performance in solar cells, using PCBM as the electron acceptor, is presented. The V_{OC} values follow the expected trend: increasing with decreasing HOMO level of the polymer. High V_{OC} values of 0.81 and 0.82 V have been obtained from two polymers: PBDPBT and PBDPDPP. The highest initial power conversion efficiency (PCE) achieved in these unoptimized devices was 1.11% due to relatively low J_{SC} values. The variation observed in the J_{SC} values between the four polymers is discussed. Device performance is expected to increase with optimization of processing conditions for the devices.

Table of Contents

Page

List of Figures

List of Tables

List of Equations

1. Introduction

1.1. Organic Photovoltaics

As global energy markets have changed significantly since the turn of the century, OPVs have emerged as a promising candidate for the generation of solar power. These devices are advantageous in that they can be manufactured on flexible substrates and employ roll-to-roll processing, which reduces processing costs and increases processing speeds. The key disadvantage of OPVs is that they are currently much less efficient than their inorganic counterparts; while some of the highest reported PCEs for organic systems have surpassed 10%,[1] inorganic devices have displayed efficiencies greater than 40%.[2] It has been determined that efficiencies for large-scale OPVs must be boosted beyond 10% for organic devices to have a chance to be competitive with their inorganic counterparts.[3, 4] Research in this field has largely focused on improving PCEs of devices by either synthesizing new materials to improve band gap conditions/mobilities of materials[5-16] or increasing control over the device microstructure.[17-23]

1.1.1. Materials for Organic Photovoltaics

Interest in organic solar cells first started when it was shown that some conjugated polymers exhibited the photovoltaic effect, but the first OPVs to show any real promise were not developed until the early 1990s.[24-26] Since then, the majority of research on OPVs has largely been based on the synthesis of semiconducting materials that have a delocalized π-conjugated electron system which can 1) absorb a lot of light, 2) create photogenerated charge carriers, and 3) quickly and efficiently transport these charge carriers to generate photocurrent. It is also important that these materials are solution proccessible to allow for large scale, inexpensive fabrication processes to be utilized. As organic electronics continue to progress and evolve, the

synthesis of novel materials to obtain improved properties and better device efficiencies remains as a key driving force for research in this field.

1.1.2. Working Mechanisms of Organic Photovoltaics

The operating principles behind OPVs can be broken down into three steps as follows: 1) incident light is absorbed by the active layer material of the device, which generates an exciton, 2) exciton dissociation occurs *via* the spatial separation of the holes and electrons within the material, and 3) the transportation and collection of these free charges at their corresponding electrodes leading to current generation. If any of these steps is inhibited, the overall efficiency of the device will suffer accordingly.

In order to determine how well an OPV performs, we measure four main parameters. These are 1) the open circuit voltage (V_{OC}), 2) the short circuit current density (J_{SC}), 3) the fill factor (FF), and 4) the power conversion efficiency (η). These values are shown graphically in Figure 1.1.

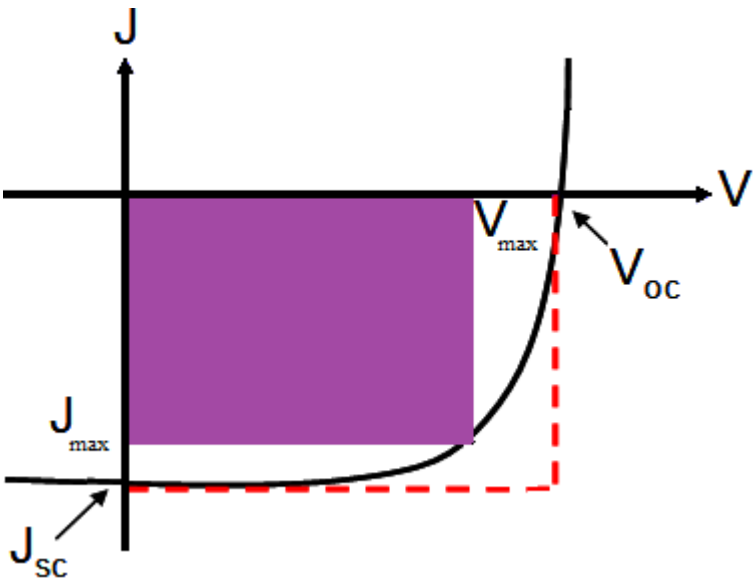

Figure 1.1 Representative J-V curve for an illuminated photodiode.

The open circuit voltage of a device is the point where there is no current flow, the short circuit current is the photo-induced current where the voltage is equal to zero, and the fill factor is the ratio between the maximum power generated by the device (purple rectangle) and the area of the V_{OC} multiplied by the J_{SC} (dotted red rectangle). These three values come together to give us the power conversion efficiency of a device (Equation 1.1), which is simply the ratio between the maximum power generated by the device and the amount of optical power incident to the device.

$$\boldsymbol{PCE = \frac{P_{max}}{P_{incident}} = \frac{V_{OC}J_{SC}FF}{P_{incident}}} \qquad \textbf{Equation 1.1}$$

To obtain more efficient devices, it is desirable for the V_{OC}, J_{SC}, and fill factor to all be maximized.

1.2. Methods to Improve Device Efficiency

In order to overcome some of the challenges listed above, it is necessary to improve upon how we currently make organic devices. This can be done by either altering the device architecture or by changing the materials that we put into the active layer of our device.

1.2.1. Device Architecture

The simplest OPV device structure consists of a single polymer thin film deposited between two electrodes. Due to the fact that only one material is employed in the active layer, these devices are appealing because they are simple to make and their optimization is much less involved. However, because there is only a single semiconductor layer, which is responsible for transporting both holes and electrons, devices using this type of architecture tend to be very inefficient. Because holes and electrons are being transported in the same material, charge transport is slow and the rate of exciton recombination is very high; active layers in these devices

must be made exceedingly thin to try and limit recombination, but then this severely reduces the amount of light that is absorbed which in turn decreases the amount of excitons that are generated.

A more successful device architecture utilizes a bilayer structure. In these devices, two separate donor and acceptor materials are cast to form the active layer, one on top of the other. After light is absorbed and exciton generation has occurred, the exciton has the opportunity to migrate to the acceptor:donor interface where it can dissociate and form free carriers. The bilayer device structure is superior to the single layer device because it utilizes discrete acceptor and donor phases to transport electrons and holes, which can greatly reduce the chance for charge recombination. Also, because two materials are used instead of one, these can be selected such that the absorption ranges are complimentary to one another, allowing a wider spectrum of incident light to be absorbed. However, the efficiency of these devices is still limited due to the relatively low interfacial surface area between the donor and acceptor materials. Unless an exciton is generated very near to the border between the donor and acceptor films, it is likely to undergo recombination, limiting the current in the device.

One of the first large-scale paradigm shifts in the way that OPVs were processed was the development of the BHJ device structure. In this architecture, the active layer of the device is a combination of both the donor and acceptor materials (*e.g.* P3HT and PCBM) co-deposited simultaneously. This allows for improved mixing and can help limit recombination. However, many BHJ devices show lower than expected PCEs due to relatively low charge carrier mobilities. This can be partially remedied by annealing devices above the glass transition temperature of the polymer. This improves device mobility by allowing the polymer chains to align and the π molecular orbitals to stack.[27] Unfortunately, annealing can also cause PCBM to

diffuse through the matrix, yielding potentially undesirable phase segregation and a reduction in the interfacial surface area between the donor and acceptor materials. Heat treatments can also lead to significant overgrowth of the PCBM domains, which can further decrease film quality.[28-30] Therefore, it may be useful to find ways to manipulate the active layer of OPVs to improve their thermal stability or pursue processing methods which omit annealing altogether.

One such method to potentially improve charge mobility and increase continuity of domains in the active layer without annealing is to introduce the donor phase into the active layer as a P3HT nanowire. These nanowires can be easily grown in solution *via* self-assembly. Nanowires are made up of extended polymer backbones stacked along the nanowire "long axis" and of laminated layers of the polymer backbones separated by alkyl side chains.[31, 32] There are several potential benefits to using nanowires. First, their height and width dimensions are similar to exciton diffusion lengths. This may allow more excitons to disassociate successfully, reducing geminate recombination and increasing efficiency. Second, the nanowire structure ensures continuity in the p-type domains. In BHJ cells, some domains are stranded in the middle of the active layer, even after annealing. If domains are not continuous, efficiency suffers. Finally, because the nanowires are present as solid particles suspended in solution, it may be possible to manipulate them to improve the microstructure of the device.

1.2.2. Development of Low-Bandgap Materials

The most powerful strategy to develop low-bandgap conjugated polymers is to incorporate electron-rich donor segments and electron-deficient acceptor segments into the polymer backbone. Because of the push–pull interaction, efficient internal charge transfer (ICT) can take place from the donor to the acceptor upon photoexcitation, leading to a new absorption band at

longer wavelengths.[33] However, developing low-bandgap polymers that exhibit good PCEs is not a simple task; although we can easily tune the bandgap of conjugated polymers using the donor–acceptor approach to produce higher J_{SC}, appropriate molecular energy levels for high V_{OC} and good charge transport are also required for superior donor materials.[34]

Generally, there are two different methods that are used to further improve PCE performance of BHJ polymer solar cells. The first approach is to develop lower bandgap polymers to harvest more influx photons thereby enhancing J_{SC}. However, there are many other factors that can affect $J_{SC,}$ such as the molecular weight of the polymer, the morphology of the blend film, and the charge mobilities within the film.[20, 35] Because numerous factors affect J_{SC}, the resulting value is hard to predict given a certain polymer. Another method to improve efficiency focuses on enhancing V_{OC} by designing polymers with low-lying highest occupied molecular orbital (HOMO) energy levels. Usually, the approach is to design a weak donor in the conjugated polymer backbone, which will help to maintain low HOMO energy levels.[36] With this strategy, V_{OC} values greater than 1 V have been achieved.[37, 38]

2. Controlling Vertical Morphology Within the Active Layer of Organic Photovoltaics Using Poly(3-hexylthiophene) Nanowires and Phenyl-C61-butyric Acid Methyl Ester

2.1. Introduction

As discussed above, one of the simplest ways to affect the active layer structure of a device is through annealing. After active layer deposition, a heat treatment can cause the donor and acceptor phases to reorganize and form larger, more continuous domains. Once optimized, this process can dramatically improve both the microstructure and performance of BHJ devices.[39] However, in traditional BHJ cells, annealing can cause a potentially unfavorable vertical material gradient. The active layers of these devices are typically deposited on top of a poly(3,4-ethylene-dioxylene thiophene):poly(styrene sulfonic acid) (PEDOT:PSS) layer, which serves as a hole transport layer. In this scenario, annealing can produce an active layer with greater concentrations of PCBM toward the "bottom".[40, 41] This segregation is attributed to differences in the surface energies of the components in the system. PCBM has a higher surface energy (37.8 mN/m^2) than P3HT (26.9 mN/m^2).[42] Therefore, more P3HT migrates towards the air:active layer interface, while PCBM becomes concentrated downward. However, the effect of annealing on vertical phase separation is currently under debate; a few recent studies have argued that annealing can produce beneficial increases in the PCBM concentration at the top of the active layer.[43, 44]

In principle, one would prefer higher concentrations of the electron-accepting species at the "top" of the active layer because such a configuration would aid in electron transport to the top electrode and block hole transport to the top surface. Therefore, the material gradient that the

majority of research groups have observed in most P3HT/PCBM systems is unfavorable and may lower the efficiency of the system.

Below, we present an alternative approach to controlling vertical morphology by using a combination of P3HT nanowires and PCBM in the active layer of devices. Using this system, it is possible to manufacture devices with increased PCBM concentration at the top of the active layer. The ability to influence and control the vertical concentration gradient of PCBM and P3HT in the active layer provides a useful tool for optimizing the microstructure and increasing the PCE of OPVs.

2.2. Synthesis

OPVs were made using P3HT nanowires and PCBM as the active layer components. Device fabrication followed a route similar to the whisker method[31] (see appendix, Section 8.1.1), but included an extra processing step to increase active layer thickness. This additional step, referred to here as "pre-spin drying time", is a period of time between the initial application of the active layer solution to substrate and the time when spin-coating is initiated. During this period, the solvent in the solution evaporates, increasing the viscosity of the active layer solution, which should lead to a thicker film upon spin-coating. This processing step will be discussed in greater detail below.

2.3. Results and Discussion

2.3.1. Influence of PCBM on NW Formation and Device Efficiency

2.3.1.1. Photovoltaic Performance

In order to increase control over the active layer morphology of the device, it may be important to understand the effect that PCBM has on P3HT nanowire formation and growth. This effect was investigated by processing films under two different conditions: process A (where PCBM is added to solution before nanowire self-assembly) and process B (where PCBM is added to solution after nanowire self-assembly). Films were made using both of these processes and were characterized and compared to one another. In process A, PCBM has the potential to directly affect nanowire formation; this is not the case in process B. By comparing films made from these two solutions, it may be possible to gain insight into how PCBM affects P3HT nanowires.

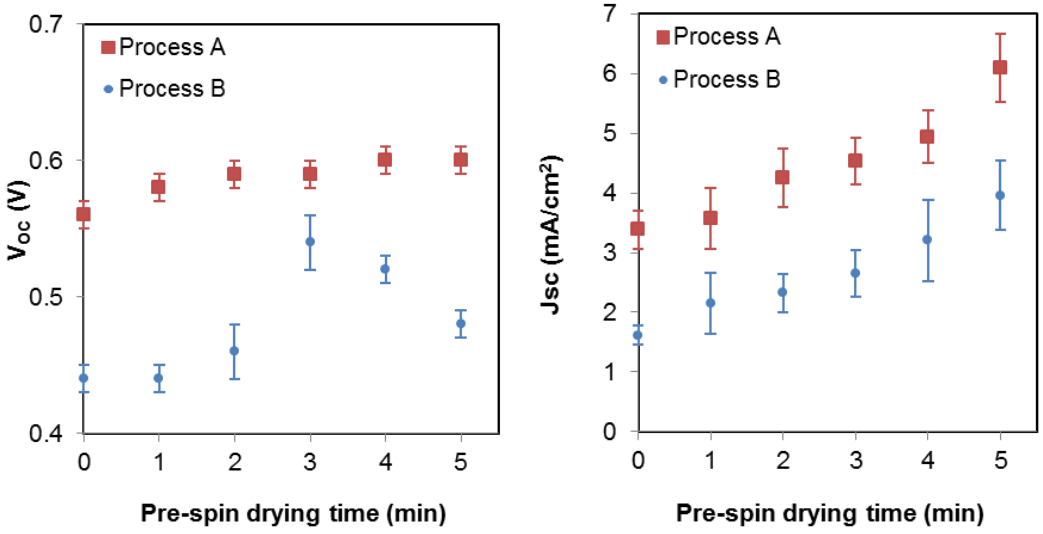

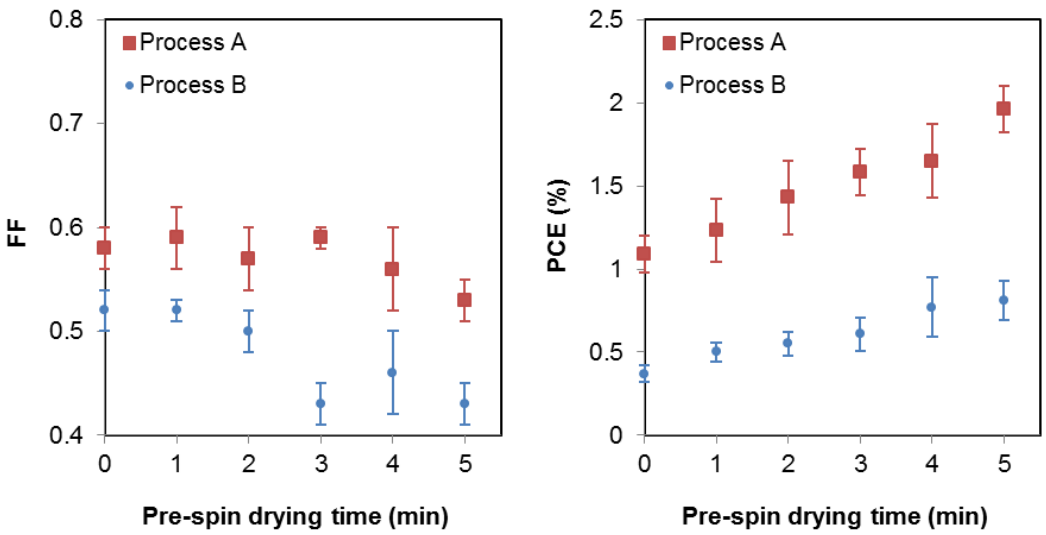

Figure 2.1 Effect of pre-spin drying time on device performance for processes A (PCBM added before nanowire assembly) and B (PCBM added after nanowire assembly). At least 24 devices were tested and averaged under each set of processing conditions. Error bars represent one standard deviation from the mean.

OPVs were made using processes A and B, and their photovoltaic performance was compared (Figure 2.1). This illustrates the effect of the processing condition on photovoltaic properties. The overall trend for device performance is the same in each scenario: efficiencies increase steadily with longer pre-spin drying time. However, the devices made when the PCBM was added after the nanowires had already formed were less than half as efficient as devices where the PCBM was in the solution during nanowire formation. Figure 2.2 provides representative *J*–*V* curves for processes A and B, showing a direct comparison between the two processing conditions.

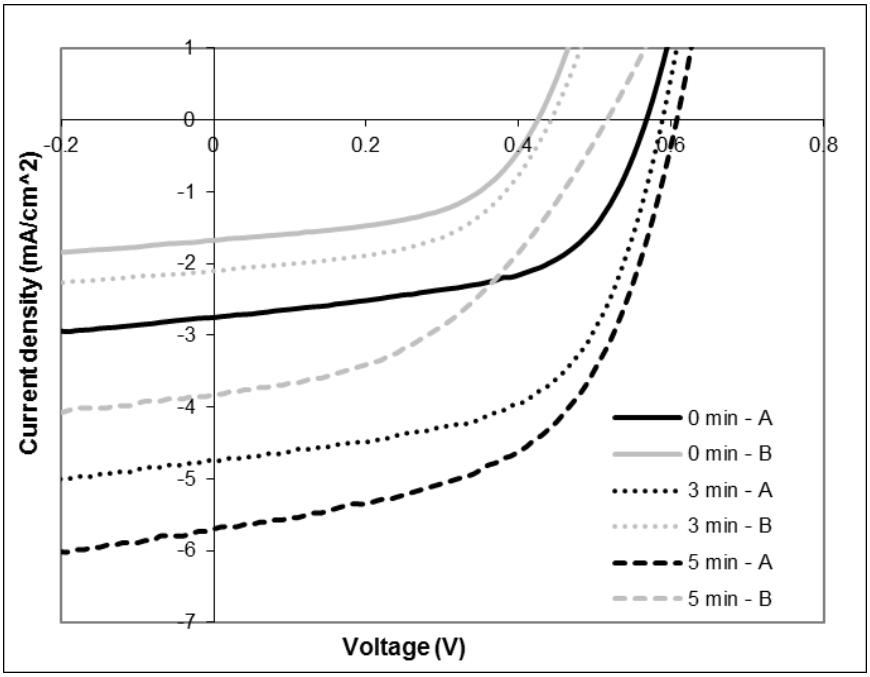

Figure 2.2 Effect of pre-spin drying time (0, 3, and 5 min) and processing condition (A, process A; B, process B) on device performance.

2.3.1.2. Effect of PCBM on Nanowire Size and Morphology

We hypothesize that introducing the PCBM after nanowire formation, as opposed to before, may alter how P3HT and PCBM interact in the active layer. One could speculate that the PCBM may be incorporated into the nanowire structure or could coat the nanowire surfaces during their formation. However, neither possibility seems to be supported by the experimental data available. Using X-ray diffraction (XRD) (see appendix, Figure 8.1), we see no difference between spectra for the P3HT nanowires regardless of whether they are formed in the presence of PCBM or not, suggesting either that any interaction between the PCBM and the nanowires during their formation is along a crystallographic axis not observed in our XRD data (e.g. (001)) or that the PCBM:P3HT interaction occurs at the surface of the nanowires.[45-47] Additionally, we found the size of the nanowires to be the same to within experimental error (Figure 2.3),

regardless of whether PCBM was present during nanowire formation or not, arguing against a coating of PCBM forming around the wires. Varying the pre-spin drying time for each of the processes (between 0 and 5 min) also failed to significantly alter the average nanowire height.

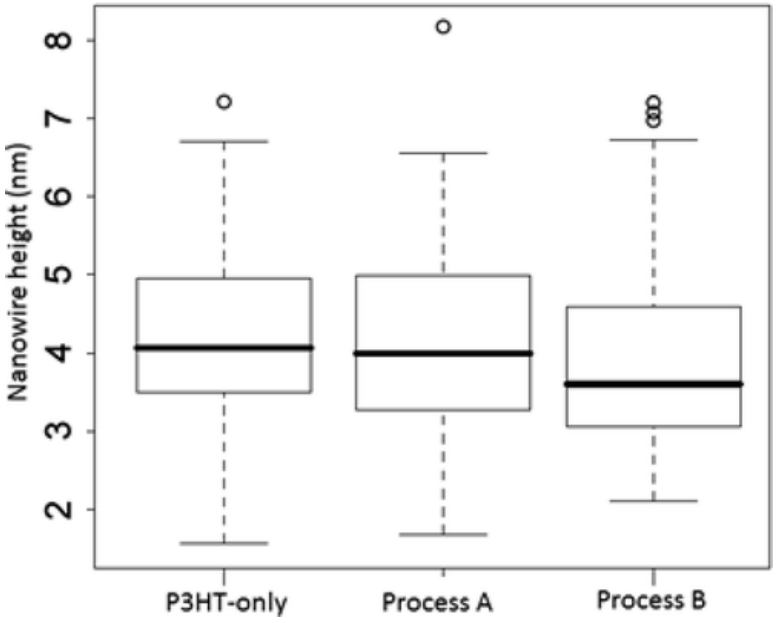

Figure 2.3 Box and whisker plot showing the effect of processing condition on nanowire height. Process A is where the PCBM is added during nanowire formation. Process B is where the PCBM is added to solution after nanowire formation. The nanowire thicknesses appear identical within experimental error, while a PCBM monolayer would be expected to be around 1 nm thick.[48]

2.3.1.3. Conductive and Photoconductive AFM

To study the effect of processing on the devices, we used conductive atomic force microscopy (cAFM) and photoconductive atomic force microscopy (pcAFM) to image the current transport networks in these devices, in order to better understand the changes in performance at the local level. In these experiments, we used cAFM to probe the dark current and pcAFM to probe the short-circuit photocurrent (see appendix, Figure 8.3). In both techniques, the conducting gold tip forms the top contact of a nanoscale solar cell.[49, 50] For these systems, it is expected that in the forward-biased case (where the tip is biased positive, relative to the sample) we observe hole

transport images, while for the reverse-biased case we observe electron transport.[51] Electron injection is possible despite the large barrier at the Au/organic interface in part because the high electric field concentration at the sharp AFM tip facilitates injection. In these images, we expect that the dark hole current will be largest where there are well-connected P3HT nanowire pathways from the top surface to the bottom contact; similarly, we would expect dark electron currents to be largest in areas where there are well-connected PCBM pathways from the top to the bottom. Alternatively, the short-circuit photocurrent images indicate areas where both photogenerated electrons and photogenerated holes can be extracted efficiently through the contacts. We have generated comparable data in previous studies of nanowire-based solar cells.[52]

In addition to analyzing devices with new active layer morphologies, the other critical difference between this investigation and older studies is that we successfully imaged these new films in attractive contact mode, so that we are able to correlate the dark hole, electron, and short-circuit photocurrent over the *same* region of the device with minimal film damage. (see appendix, Figure 8.2) Using cAFM and pcAFM we are able to observe how the two different processes affect local electronic behavior in terms of PCBM−nanowire interaction. Figure 2.4 shows sets of data taken with the same tip for films made with the PCBM added during nanowire formation (process A, Figure 2.4A−D) or added after nanowire formation (process B, Figure 2.4E−H). We made sure to use the same approximate laser intensity to avoid intensity-dependent photocurrent effects.[53] Topographically, the two films are similar in that we observe nanowires of comparable dimensions and density.

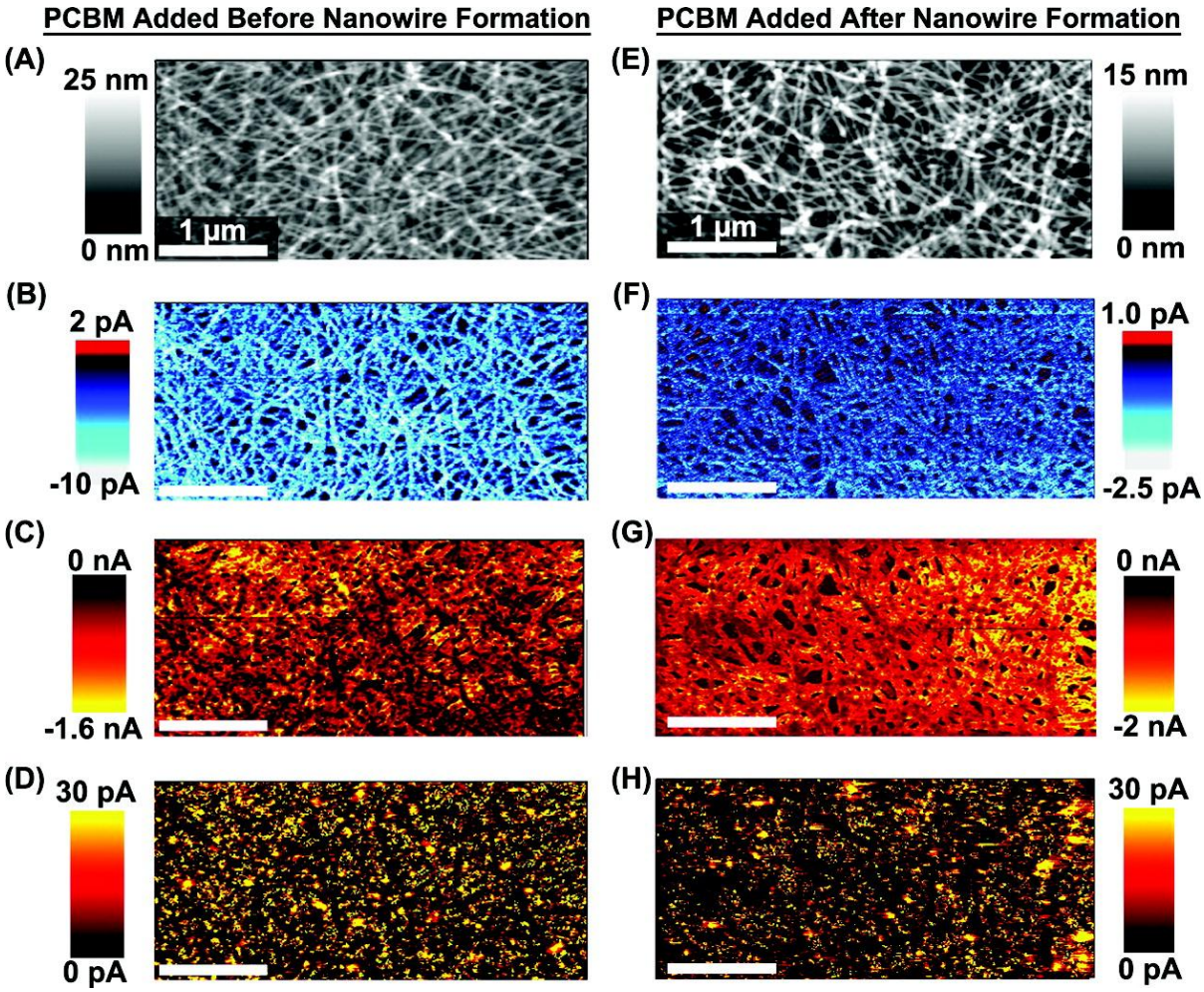

Figure 2.4 Correlated (A) topography, (B) short-circuit photocurrent, (C) dark hole current (+3 V applied to the tip), and (D) dark electron current (−3 V applied to the tip) on a film made with process A, where the PCBM is added during nanowire formation. (E−H) The same correlated images for a film made with process B, where the PCBM is added to the solution after the nanowires have formed. The same AFM tip was used and the laser intensity held constant for both sets of data.

The spatially averaged dark hole current increases significantly when the PCBM is added after nanowire formation (process B). For the process A film in Figure 2.4C, the average dark hole current is −488 pA, while the process B film exhibits an average dark hole current of −622 pA in Figure 2.4G. The spatially averaged dark electron current shows the opposite trend. In Figure 2.4D, the process A film has an average dark electron current of 25 pA, while the process B film in Figure 2.4H has an average dark electron current of 11.7 pA. The pcAFM data measure higher photocurrents in the film made with process A, in good agreement with the macroscopic device

results. The average photocurrent decreases from *ca*. −5.0 pA to *ca*. −1.0 pA when using process B instead of A. The areas of efficient dark transport are not obviously correlated with areas of high photocurrent, similar to that observed for P3HT-PCBM films.[51] The isolated regions of dark electron current in Figure 2.4D and H do not appear to be caused by topographic effects such as the tip pulling on the fibers, as that would cause noticeable film damage and, most likely, significant change in the associated short-circuit photocurrent images (see appendix, Figure 8.2).

These three sets of current data are consistent with the hypothesis that adding the PCBM after nanowire formation (process B) negatively alters the film morphology, possibly through changes in the PCBM−nanowire interaction that inhibit intimate coating of the nanowires. Our photocurrent data are consistent with this interpretation, given the 5× increase in average photocurrent for process A versus process B. A more intimate PCBM coating as in process A might be expected to enhance exciton dissociation at the nanowires and increase the average photocurrent, even though the photocurrent is negative in both films. We interpret the changes in dark current averages to changes in relative PCBM surface concentration and nanowire connectivity. The higher dark electron current in process A implies higher PCBM surface concentration; the higher dark hole current in process B, on the other hand, indicates higher nanowire coverage at the surface and better connectivity to the bottom electrode. The higher electron current and lower hole current in process A are therefore indicative of a preferential morphology for device performance, confirmed through the short-circuit photocurrent data and device measurements in Figures 2.1 and 2.2. The dark current and photocurrent data are self-consistent in terms of the trends exhibited by the change in processing.

2.3.2. Effect of Pre-Spin Drying Time on Device Morphology and Performance

2.3.2.1. Photovoltaic Performance

In addition to observing the effect of PCBM on P3HT nanowire growth, we also further investigated the effects of pre-spin drying time on device morphology and performance. The photovoltaic results for pre-spin drying times up to 5 min are shown in Figure 2.5; at least 24 devices were tested under each set of processing conditions. Devices used in this study were made using process A because this fabrication route produced higher performance solar cells as discussed earlier (Figure 2.2). Devices were also made with longer pre-spin drying times, but the viscosity of the active layer solution increased to the point where consistently good films could no longer be made *via* spin-coating. Device performance peaked at a pre-spin drying time of 5 min.

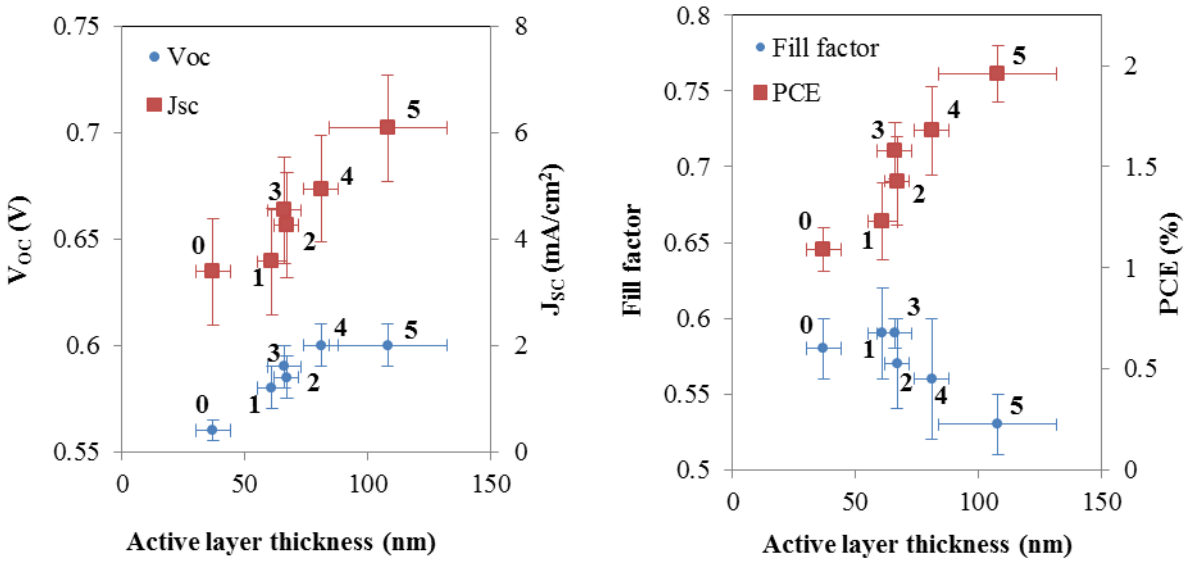

Figure 2.5 Device parameters plotted as a function of active layer thickness. The numbers next to data points represent the pre-spin drying time in minutes. Devices were fabricated using process A. Error bars represent one standard deviation from the mean.

The data in this figure demonstrate that for increasing pre-spin drying times both the J_{SC} and the PCE steadily increase while the V_{OC} remains fairly constant and the fill factor decreases. The rise

in J_{SC} is likely related to the increase in absorption brought about by a thicker active layer, which could lead to a more efficient device. The reduction in fill factor may be caused by the decrease in the shunt resistance of the devices as the pre-spin drying time increases. A lower shunt resistance indicates lower charge extraction efficiency; however, as the absorption of our active layer increases, we should be able to generate significantly more charges, so we still observe an overall increase in device efficiency.

It should be noted that the active layer thickness does not steadily increase with increased pre-spin drying times. Between 1 and 3 min, the active layer thickness remains fairly constant. Improvement in device performance without increased active layer thickness suggests that other factors may be influencing device efficiency. Figure 2.6 shows representative $J-V$ curves from these devices, graphically illustrating the increase in device performance with longer pre-spin drying times.

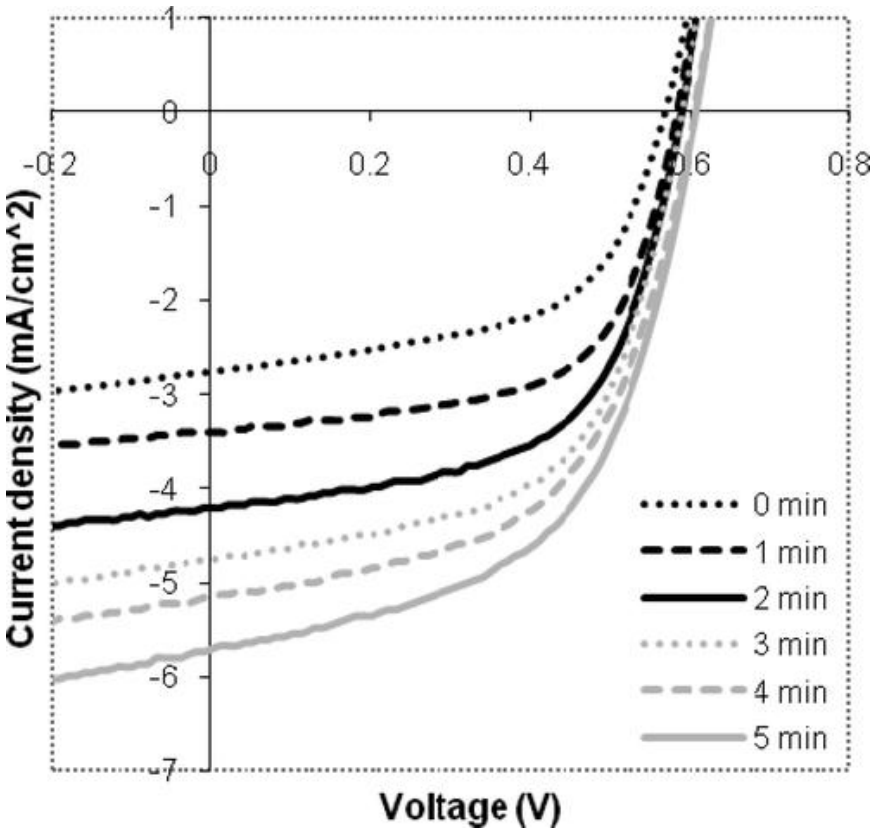

Figure 2.6 Current−voltage curves for devices made with different pre-spin drying times showing the effect of pre-spin drying time on device performance. The 1, 2, and 3 min devices had similar active layer thicknesses, so performance differences between these three may be due to changes in active layer morphology.

2.3.2.2. Conductive AFM

We hypothesize that an increase in pre-spin drying time allows the P3HT and PCBM in the active layer to rearrange and adopt an altered distribution, impacting the microstructure of the device. To test this theory, we used cAFM to image the change in current behavior as a function of pre-spin drying time. Figures 2.7A−C and 2.3A−C show the topography and correlated dark hole and electron current for the film formed with no pre-spin drying time (Figure 2.7) and with a 5 min pre-spin drying time step (Figure 2.8). These conditions correspond to total film thicknesses of ~37 and ~108 nm, shown in Figure 2.5.

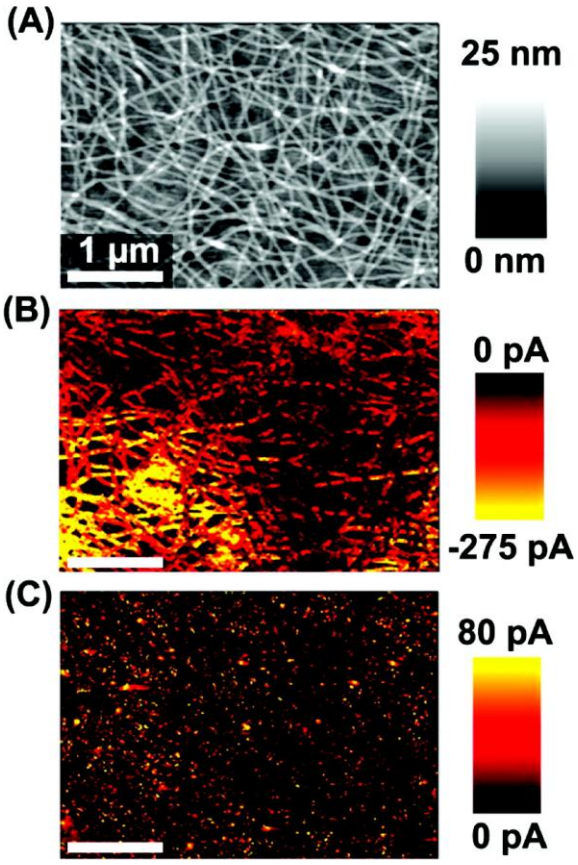

Figure 2.7. Correlated (A) topography, (B) dark hole current (+3 V applied to the tip), and (C) dark electron current (−3 V applied to the tip) on a P3HT nanowire:PCBM film with no pre-spin drying time.

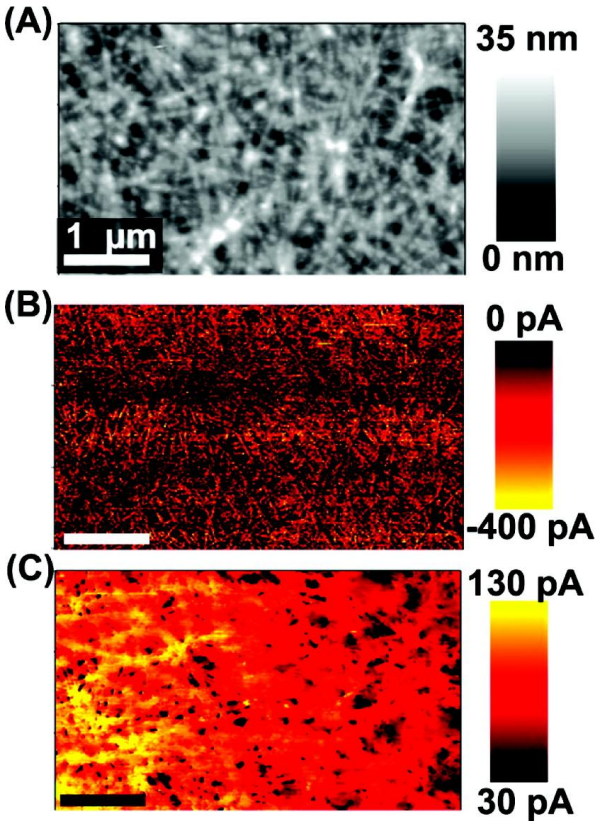

Figure 2.8. Correlated (A) topography, (B) dark hole current (+3 V applied to the tip), and (C) dark electron current (−3 V applied to the tip) on a P3HT nanowire:PCBM film with 5 min pre-spin drying time.

The sets of data were taken with the same tip to avoid undue influence from different tip states. We observe two key features in these data. First, the dark electron current in the 0 min film is significantly less than that in the 5 min film, *despite the fact that the 0 min film is thinner*. The average of the dark electron current is ~9 pA in the 0 min film yet is ~81 pA in the 5 min film. Furthermore, the electron transport image in Figure 2.8C (5 min film) has a nonzero current background as opposed to the isolated hot spots of transport amidst a largely zero current background seen in Figure 2.7C for the zero drying time film (see appendix, Figure 8.3 for histogram data). Second, in terms of dark hole current, we observe areas of "hot" nanowires in the 0 min film (lower left, Figure 2.7B) where the hole current reaches values as high as −1.34 nA, with an average current of −55 pA. The image of the film spin-coated with a 5 min pre-spin

drying time in Figure 2.8B shows that the average hole current has increased to −77 pA, consistent with the expectations of more homogeneous P3HT distribution throughout the active layer, although the change for holes (~1.4× increase) is significantly smaller than the change observed for electron transport (~9× increase).

We interpret both the 9-fold increase in electron dark current with pre-spin drying time and the concomitant transition of the local spatial distribution of electron transport from being "mostly off" in Figure 2.7C to "mostly on" in Figure 2.8C as being associated with both an increase in PCBM connectivity in the film and a significant change in the fraction of PCBM that is exposed (or very near) to the top film/air interface, allowing electrons to be injected from the cAFM tip into the PCBM domains. In this picture, the electron transport hotspots in Figure 2.7C would be consistent with small numbers of PCBM domains that penetrate the P3HT wetting layer on the film surface,[50] while the more uniform electron currents in Figure 2.8C would correspond to a much larger number of exposed or near-surface PCBM domains. That is, we are able to infer from these cAFM data that important changes in both the connectivity and top surface concentration of PCBM are occurring due to the pre-spin drying step.

2.3.2.3. XPS

While the cAFM data are suggestive, the X-ray photoelectron spectroscopy (XPS) data provide clear spectroscopic evidence for this hypothesis. XPS can be used to monitor changes in surface composition in P3HT/PCBM blends by comparing the signature peaks for oxygen-1s (O1s) and sulfur-2p (S2p).[54] The concentration of P3HT scales with the S2p peak, while the concentration of PCBM correlates to the intensity of the O1s peak. The spectra for these two peaks collected from devices with different pre-spin drying times are displayed in Figure 2.9. Care was taken to

ensure that the films were not exposed to air to limit contamination from ambient oxygen. All peaks have been normalized to the signature C1s peak.

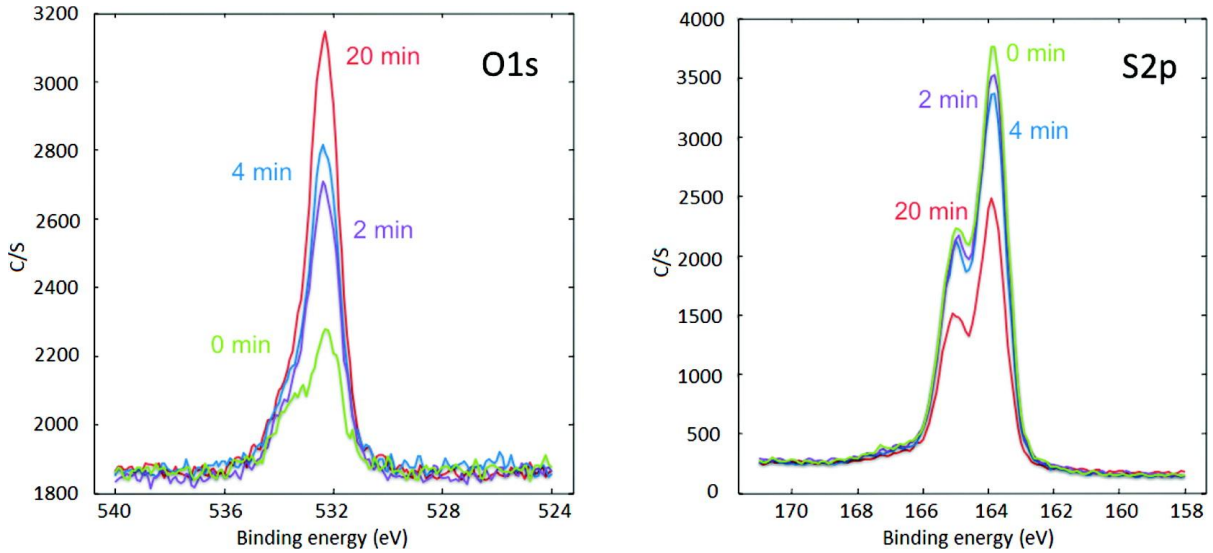

Figure 2.9 XPS spectra (45-degree resolve) of film surfaces at different pre-spin drying times corresponding to the presence of O1s PCBM and S2p P3HT.

These graphs shows that the O1s peak intensity increases and the S2p peak decreases with longer pre-spin drying times, indicating that the P3HT concentration at the film/air interface is decreasing (and the PCBM concentration is increasing) with increasing pre-spin drying time. Attempts to delaminate our films in order to perform XPS on the "bottom" of the active layer, to see if a complementary change in concentration is evident at the film/PEDOT interface, proved to be unsuccessful due to the relatively low thicknesses of many of our films (25−100 nm). However, because the trends observed in Figure 2.9 support our cAFM data, we believe that the observed changes in concentrations are meaningful.

Evidently, changing the length of the pre-spin drying time strongly alters the material gradient in the active layer, providing greater control over the vertical morphology. These changes in vertical morphology have important implications for device optimization. In standard BHJ

device architectures, higher concentrations of the electron-accepting species at the top of the active layer should be preferred because this would aid in electron transport to the top electrode. Therefore, the material gradient that is generated with increased pre-spin drying times should be more favorable, and may contribute to the improved performance we observe in our devices with increasing pre-spin drying times.

2.3.2.4. Potential Causes for Phase Separation

We next discuss possible explanations for the radically different vertical morphology observed in these experiments as compared to P3HT/PCBM blend films without preformed P3HT nanowires. It is possible such behavior could arise if P3HT nanowire films exhibit a significantly different surface energy than normal P3HT films. However, contact angle measurements, corrected for the effects of surface roughness using Wenzel's equation,[55] show that P3HT films containing nanowires and those without nanowires have similar surface energies. Thus, we conclude that the differences in vertical morphology of the P3HT nanowire films must have another explanation.

An alternative hypothesis to explain the phase separation is that the P3HT nanowires are simply settling out of solution during the pre-spin drying time. Unlike traditional active layer solutions, where both the P3HT and PCBM phases are dissolved in solution, the P3HT nanowires are insoluble at room temperature, forming solid particles. Over time, gravity causes these nanowires to sink, leading to an increase in P3HT concentration at the bottom of the vial. If this phenomenon occurs on the substrate during the pre-spin drying time, this would leave behind a PCBM-rich region toward the top of the active layer. Upon spin-coating, this phase separation is effectively frozen within the active layer microstructure, causing the phase segregation that we noticed above.

It was observed that when left at rest in a vial, it took days for the nanowires to noticeably settle out of solution. In this scenario, the volume of solution was 1−2 mL and settling occurred over a distance of >1 cm. However, when the active layer solution is deposited on the device substrate, a much smaller volume is used (60 μL) and the settling distance is much smaller (~0.03 cm). Smaller volumes and shorter settling distances significantly increase the observed sedimentation rate of a suspension. Therefore, it does not seem unrealistic that a noticeable change in P3HT concentration could occur during pre-spin drying times of less than 5 min.

A final hypothesis is that the pre-spin drying time allows for the formation of larger PCBM crystals, which support better connectivity and are more likely to penetrate the top film surface and contribute to the O-1s signal in the XPS measurements.

2.4. Conclusions

We have successfully demonstrated a processing technique based on preformation of P3HT nanowires that can be used to control vertical composition gradients within the active layer of bulk heterojunction solar cells. By using P3HT nanowires and introducing a "pre-spin drying time" step, we are able to increase the amount of PCBM at the top of the active layer. This provides greater control over the device microstructure and can be used to produce more efficient OPVs. Additionally, we showed that PCBM influences the efficiency of P3HT nanowires in OPVs. While the mechanism remains unclear, the presence of PCBM during nanowire formation greatly influences device performance and microstructure and thereby improves device efficiencies; this knowledge represents another tool that could be utilized to create more efficient OPVs.

3. The Effect of Regioregularity on Charge Transport and Coherent Domain Size in P3HT Nanowires

3.1. Introduction

We have shown that introducing P3HT into the active layer as a nanowire is a novel way to improve the processing of OPVs because it allows us to gain increased control over the active layer microstructure. However, there is also the potential to manipulate the nanowires themselves in order to improve intrinsic device properties. One way to go about this is to carefully control/manipulate the polymer before nanowire self-assembly.

In our group, we have demonstrated a strong ability to carefully control the regioregularity of P3HT.[56] This is quite useful because as the regioregularity of polythiophene increases, the electronic properties of the polymer are improved.[57, 58] This improvement is largely caused by improved stacking between polymer chains which can lead to better electronic communication. During P3HT polymerization, three types of coupling products can form. These are shown below in Figure 3.1.

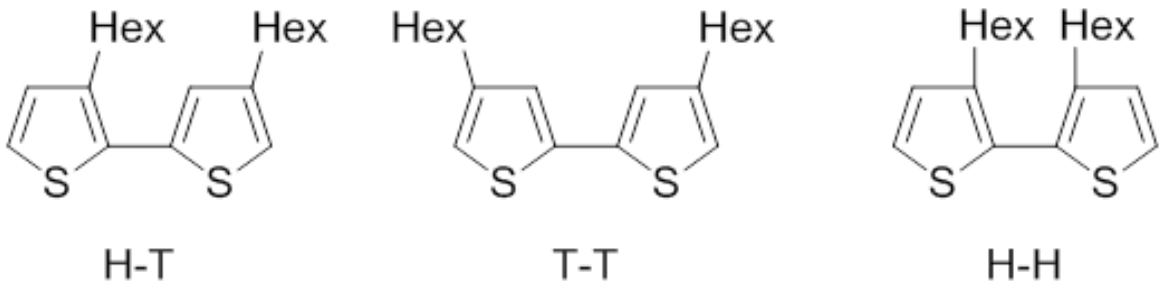

Figure 3.1 Possible coupling products in P3HT.

The desired, regioregular coupling product is the head-to-tail (H-T) conformation. Conversely, the products which lead to a decrease in regioregularity (defect products) are the head-to-head (H-H) and tail-to-tail (T-T) conformations. The steric proximity of the alkyl chains in the H-H and T-T products causes a twist along the polymer backbone which inhibits packing. By synthesizing polymers with limited head-to-head and tail-to-tail defects, we can obtain materials with improved conjugation and electronic properties; we would like to determine how the properties of nanowires are affected by changes the regioregularity of P3HT.

Because we are limiting the coupling defects within our polymers, the size of the domains within the P3HT nanowires may exhibit greater long-range order; this has the potential to improve the charge transport properties of our devices. Below, we discuss how increasing the regioregularity of P3HT in a series of polymer nanowires alters the crystallinity. Using XRD, we show that as the regioregularity of the P3HT increases, the coherent domain size along the nanowire long-axis increases in size. When wires made from varying regioregularities are integrated into the active layer of OFETs, we see a significant increase in the charge transport properties as regioregularity increases. Conversely, when non-nanowire films are made from this same series of polymers, the crystallinity remains largely unchanged as regioregularity increases and the improvement in charge transport is not as significant.

3.2. Synthesis

The high-regioregular polymers used in this study were synthesized using an external initiation method using chlorotoluene as the initiator.[56] Synthesis was carried out by Drs. Matthew Durban and Shane Boyd. The 93% regioregular P3HT was obtained from Reike Metals. Complete synthesis and experimental procedures are discussed in the appendices (Section 8.2.1).

3.3. Results and Discussion

3.3.1. Polymer Characterization

Polymers were characterized with GPC and NMR in order to determine their molecular weight and regioregularity. These results are summarized in Table 3.1.

Table 3.1 Regioregularity, molecular weight, and dispersity for P3HT polymer series.

RR (%)	M_n (kDa)	M_w (kDa)	Đ
93	19	28	1.5
96	18	20	1.1
97	21	23	1.1
98	16	19	1.2
99	20	25	1.2

Slight changes in polymer regioregularity have been shown to profoundly affect P3HT performance, especially at very high levels of regioregularity;[59] therefore, having a series of polymers ranging in regioregularity from 93% to 99% actually represents quite a large range. It should be noted that changes in molecular weight can also influence the properties of P3HT, but these differences are typically observed over significantly larger changes in molecular weight than we have in our study.[60] The 93% regioregular polymer was purchased commercially, which explains the larger dispersity.

3.3.2. Influence of Regioregularity on Nanowire Thin Film Morphology

First, we made and characterized a series of nanowire thin films from the different polymers mentioned above. This was done to see how the film quality and morphology changed as the regioregularity of the P3HT was increased. Representative AFM images for these films are shown below (Figure 3.2).

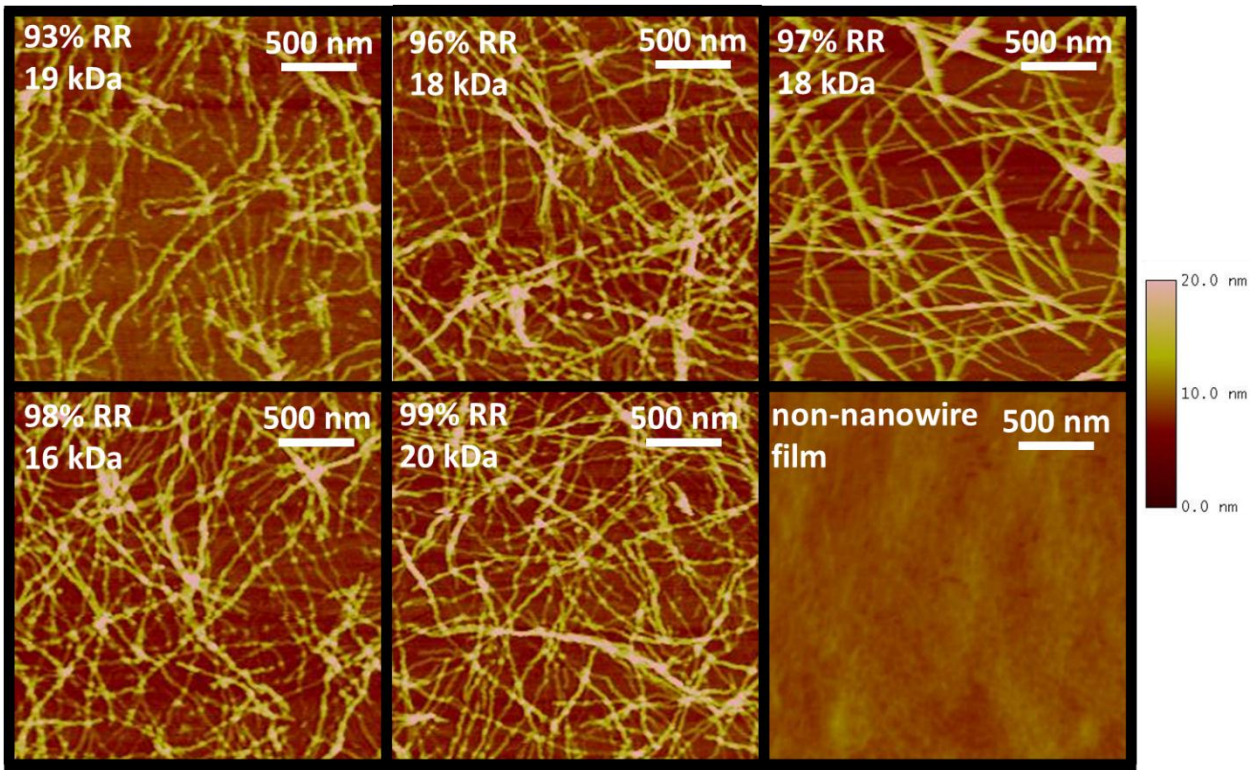

Figure 3.2 AFM height images for nanowire thin films comprised of 93%, 96%, 97%, 98%, and 99% regioregular P3HT. A smooth, featureless, non-nanowire P3HT film (99% RR) is included for comparison.

The quality and morphology of each of these nanowire films appears to be very similar to one another. They all show a tangle of well-defined nanowires which are about 24 nm wide, 5 nm tall, and several microns long. Average values for these nanowires are summarized below (Table 3.2). A population of at least 100 nanowires from each polymer was measured to determine these values.

Table 3.2 Nanowire dimensions for P3HTs with different regioregularities.

RR (%)	M_n (kDa)	M_w (kDa)	Đ	height (nm)	width (nm)
93	19	28	1.5	4.9 ± 1.1	24 ± 2.5
96	18	20	1.1	4.8 ± 1.3	24 ± 4.4
97	21	23	1.1	5.2 ± 1.1	24 ± 3.4
98	16	19	1.2	4.1 ± 1.1	24 ± 3.3
99	20	25	1.2	5.1 ± 1.0	24 ± 2.5

Boxplots for these populations are shown in the appendices (Figure 8.4). There is no clear trend between the regioregularity and the height, width, or surface coverage of the nanowires in the nanowire film. Each polymer appears to produce nanowires of the same dimensions and morphology. Therefore, we would expect any variation in film behavior to be attributed to the different regioregularity of the polymers and not simply changes in the film morphology.

3.3.3. Effect of Regioregularity on the Coherent Domain Size of P3HT-Nanowires

Nanowire films were also made and analyzed by X-ray diffraction in order to observe how the crystallinity of the nanowires change with increased P3HT regioregularity. The XRD spectra for these samples are shown below.

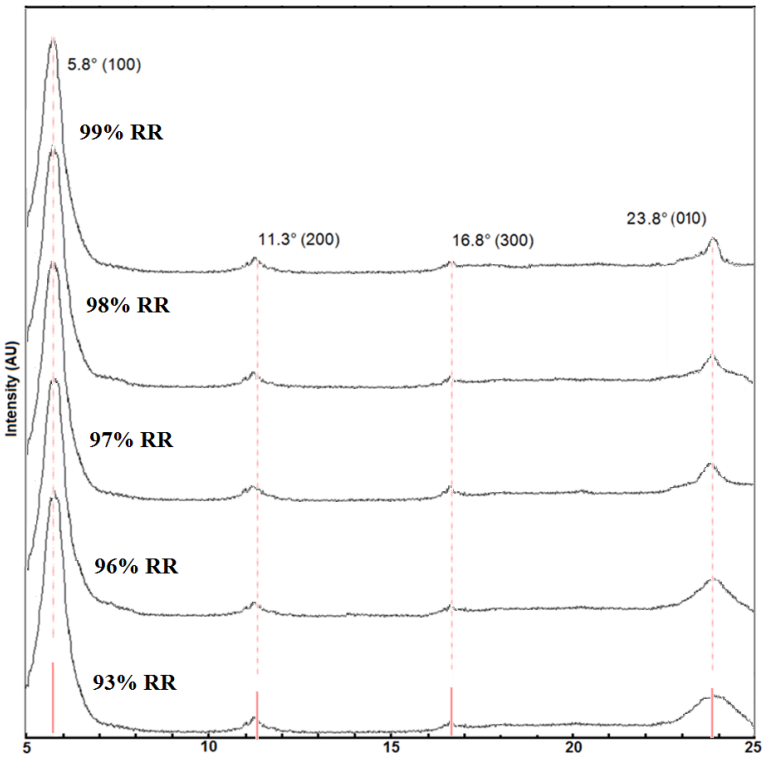

Figure 3.3 XRD spectra for nanowire films made from different P3HT regioregularities.

Looking at these spectra, we can see that neither the (100) peak (at 5.8° 2θ), nor the (010) peak (at 23.8° 2θ) shift their position. However, the peak breadth, particularly for the (010), does vary

with regioregularity. To see how appreciable this change is we can use the Scherrer Equation (Equation 3.1, where K is a dimensionless shape factor, λ is the X-ray wavelength, θ_B is the Bragg angle, and $\Delta\theta$ is the line broadening at half the maximum intensity), to extract information related to the peak breadth, in order to determine the coherent domain size found within the nanowires.

$$\xi \approx \frac{K\lambda}{(\Delta\theta)cos(\theta_B)}$$

Equation 3.1

For P3HT, $\xi_{(100)}$ corresponds to the nanowire domain size perpendicular to the substrate, while $\xi_{(010)}$ corresponds to the nanowire domain size along the long-axis of the nanowire. These values have been calculated and are shown in Table 3.3.

Table 3.3 Summary of unit cell values and coherent domain sizes determined from XRD spectra.

RR (%)	$d_{(100)}$ (nm)	$\xi_{(100)}$ (nm)	$d_{(010)}$ (nm)	$\xi_{(010)}$ (nm)
93	0.17	8.1	0.38	6.2
96	0.17	8.7	0.38	11
97	0.17	8.5	0.38	14
98	0.17	8.7	0.38	21
99	0.17	8.4	0.38	27

This data shows that as the regioregularity of the P3HT increases, there is an accompanying increase in the coherent domain size within the nanowires along the long-nanowire axis. There is no such trend for the $\xi_{(100)}$ domains perpendicular to the substrate surface. As H-H and T-T defects are limited, there are fewer perturbations within the nanowire, which appears to lead to

more long range order of the P3HT. This improvement in order may lead to better charge transport properties within the nanowire films.

3.3.4. Influence of Regioregularity on the Charge Transport Properties Observed in Nanowire OFETs

To test how the electronic properties of the P3HT nanowires are affected by different polymer regioregularities, OFETs were made out of the nanowire films. This electrical characterization is summarized below in Table 3.4.

Table 3.4 Summary of FET characterization of nanowire and non-nanowire films with varying P3HT regioregularity.

RR (%)	film type	V_t (V)	$I_{on}:I_{off}$	μ_h (cm^2/Vs)
93	nanowire	18	10^2	$4.5\times10^{-4} \pm 5.0\times10^{-5}$
96	nanowire	13	10^3	$7.8\times10^{-4} \pm 1.0\times10^{-4}$
97	nanowire	11	10^3	$1.2\times10^{-3} \pm 1.5\times10^{-4}$
98	nanowire	9	10^3	$1.6\times10^{-3} \pm 1.1\times10^{-4}$
99	nanowire	12	10^3	$1.5\times10^{-3} \pm 2.3\times10^{-4}$
93	non-nanowire	6	10^3	$4.0\times10^{-4} \pm 5.0\times10^{-5}$
96	non-nanowire	8	10^3	$5.7\times10^{-4} \pm 7.0\times10^{-5}$
97	non-nanowire	6	10^4	$6.6\times10^{-4} \pm 6.0\times10^{-5}$
98	non-nanowire	9	10^3	$8.0\times10^{-4} \pm 1.2\times10^{-4}$
99	non-nanowire	7	10^3	$8.5\times10^{-3} \pm 1.0\times10^{-4}$

Table 3.4 shows that as the regioregularity of the P3HT increases, the hole mobility increases as well. This supports the idea that increased long-range order in the nanowires leads to better charge transport properties. These high-regioregular wires have fewer domain boundaries, which are known to impeded charge transport, allowing charges to move more efficiently along the long-axis.[35, 61]

In the literature, similar trends have been observed for non-nanowire films of P3HT. As the regioregularity of the polymer increases, the hole mobility also rises. However, the trends observed in these studies seem to be less significant than what is observed above in the nanowire films.[58] To determine whether or not the improvement in hole mobility is more pronounced in nanowire films, we produced a series of non-nanowire films from the same polymers to act as a control. These films were prepared under the same processing conditions as the nanowire films, with the exception that they were cast from pure chloroform as opposed to a combination of anisole and chloroform. The OFET characterization results for the non-nanowire films are shown in Table 3.4. Below, Figure 3.4 graphically depicts the trends between hole mobility and regioregularity for both nanowire and non-nanowire films.

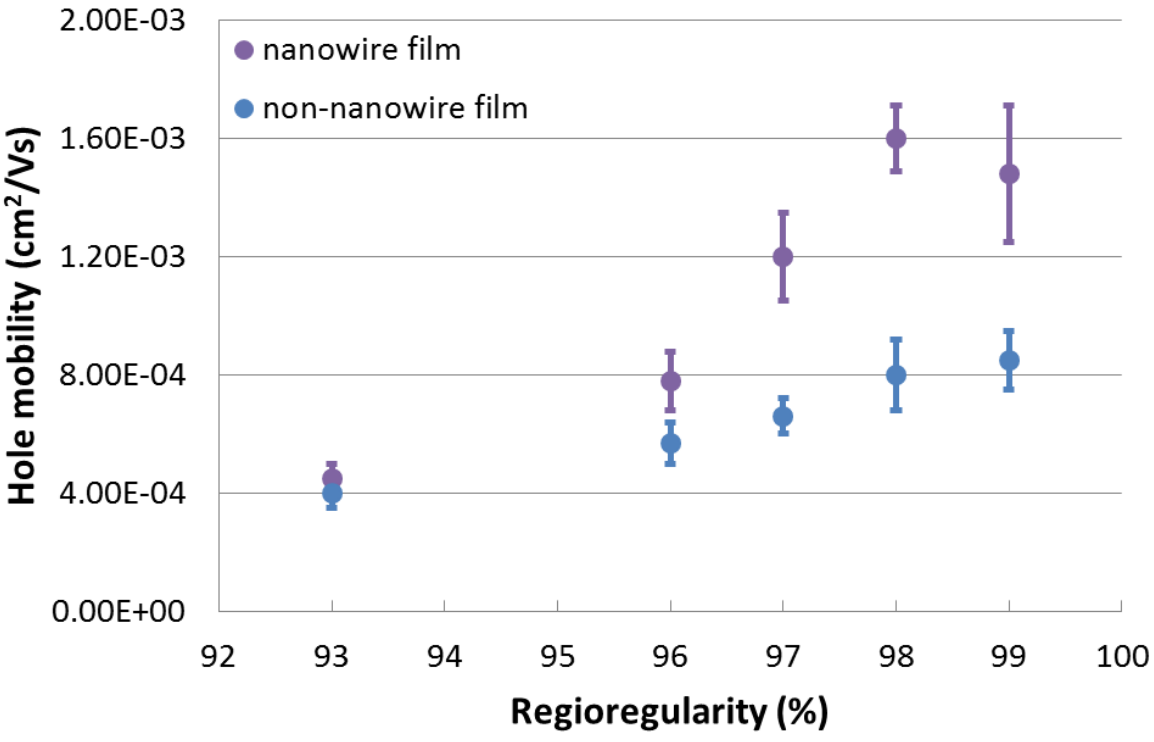

Figure 3.4 Relationship between regioregularity and hole mobility for P3HT nanowire and non-nanowire films. Error bars represent one standard deviation from the mean.

We can see that both nanowire and non-nanowire films experience an increase in hole mobility as the regioregularity of the P3HT increases. However, the increase in performance is much more appreciable in nanowire films (a four-fold improvement) than it is in non-nanowire films (a two-fold improvement). An explanation for this might be related to the fact that non-nanowire P3HT films are generally less ordered than P3HT nanowire films. Because these films are less ordered, the path on which a free charge is transported is likely to be more torturous. When we raise the regioregularity of our P3HT and limit the amount of coupling defects (H-H or H-T), charge transport becomes easier in both the nanowire and non-nanowire films. However, because the nanowires are more ordered to begin with, the improvement in electronic performance is more pronounced in nanowire films; the closer we get to a defect free material, the more impact each individual defect has on performance.

Looking more carefully at our data, we can observe that the hole mobility for the nanowire films plateaus between 98 and 99% regioregularity. If the increase in charge transport properties is related to the increase in coherent domain size, we would not necessarily expect this plateau to occur. In order to elucidate what is happening, we made a series of dilute nanowire films from the same series of polymers. We believe that areas where wires overlap might be acting as charge transfer points where holes might be hopping vertically to a neighboring wire, above or below. If this is occurring, this could adversely affect the hole mobility measured with OFETs, which only measures charge transport parallel to the substrate's surface between the source and drain electrodes. Dilute nanowire films should have fewer nanowires overlapping. This will limit the amount of charge pathways perpendicular to the substrate's surface and help us determine whether the plateau in hole mobility seen in Figure 3.4 is intrinsic to the P3HT nanowires, or if it's an extrinsic effect brought about by the way we are processing and characterizing our films.

Representative AFM height images for standard and dilute P3HT nanowire films are shown in Figure 3.5.

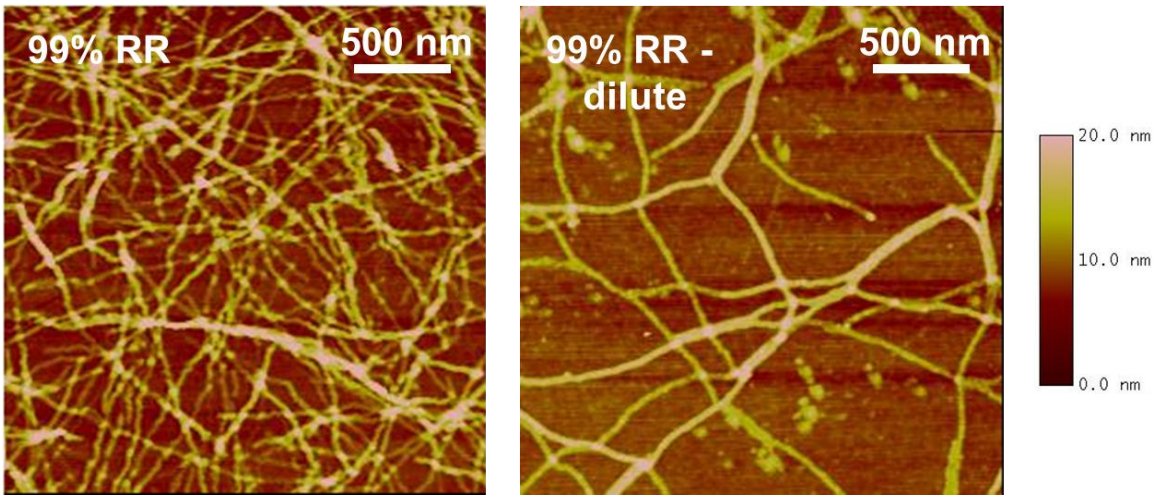

Figure 3.5 Representative AFM height images showing film morphology for standard and dilute P3HT nanowire solutions. Dilute solutions contained one fifth the concentration of P3HT. Nanowire size/shape remain unchanged, while surface coverage is significantly lower for the dilute solution.

From these images, it is readily apparent that the surface coverage for the dilute film is significantly lower than for the standard nanowire film. Surface coverage has been reduced from ~45% to ~15%. There is also a significant decrease in the amount of nanowires overlapping one another. However, the individual nanowires that make up the film remain unchanged in their dimensions. OFETs were made from these dilute nanowire films. The electronic characterization results are shown in Table 3.5.

Table 3.5 Summary of FET characterization of standard nanowire and dilute nanowire films with varying P3HT regioregularity.

RR (%)	film type	V_t (V)	$I_{on}:I_{off}$	μ_h (cm^2/Vs)
93	Nanowire	18	10^2	$4.5\times10^{-4} \pm 5.0\times10^{-5}$
96	Nanowire	13	10^3	$7.8\times10^{-4} \pm 1.0\times10^{-4}$
97	Nanowire	11	10^3	$1.2\times10^{-3} \pm 1.5\times10^{-4}$
98	Nanowire	9	10^3	$1.6\times10^{-3} \pm 1.1\times10^{-4}$

99	Nanowire	12	10^3	$1.5\times10^{-3} \pm 2.3\times10^{-4}$
93	dilute nanowire	22	10^2	$4.1\times10^{-4} \pm 8.0\times10^{-5}$
96	dilute nanowire	18	10^3	$9.2\times10^{-4} \pm 1.6\times10^{-4}$
97	dilute nanowire	23	10^3	$1.4\times10^{-4} \pm 2.2\times10^{-4}$
98	dilute nanowire	17	10^2	$2.0\times10^{-4} \pm 2.5\times10^{-4}$
99	dilute nanowire	20	10^3	$2.1\times10^{-3} \pm 2.6\times10^{-4}$

We can see that the hole mobility for the dilute nanowire films increases as regioregularity increases. Additionally, the hole mobility values are larger for the dilute films than for the standard nanowire films. In addition to increased long-range order, fewer overlapping points between nanowires lead to better charge transport properties in OFETs. This suggests that the hole mobility plateau observed in Figure 3.4 is not in fact caused by an intrinsic limit of the P3HT nanowires. This comparison between standard and dilute nanowire films (shown graphically in Figure 3.6) allows us to reach a better understanding about the real trend between charge transport along the nanowire long-axis and the regioregularity of the P3HT.

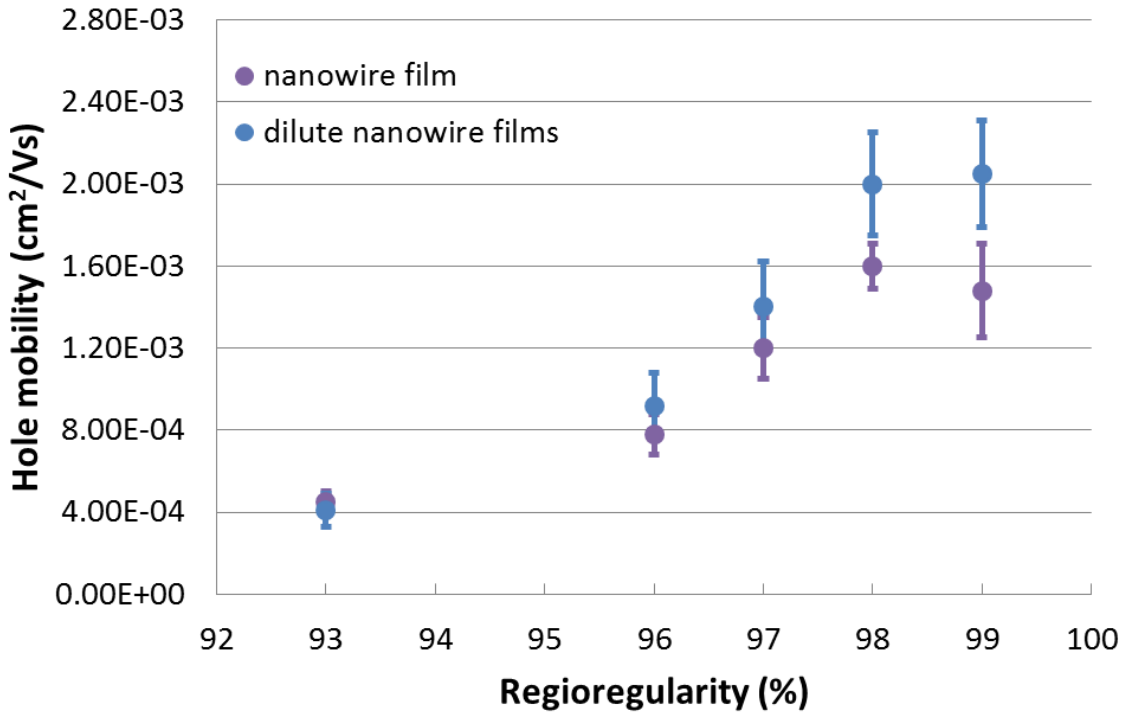

Figure 3.6 Relationship between regioregularity and hole mobility for P3HT nanowire and dilute nanowire films. Error bars represent one standard deviation from the mean.

The quality and uniformity of the dilute films did suffer as a result of the decrease in polymer concentration, leading to an increase in variability. Despite this, the average hole mobility values were still superior compared to the standard nanowire films.

3.4. Conclusion

We have successfully shown that polymer regioregularity affects the long range order of self-assembled P3HT nanowires. Increasing the regioregularity from 93% to 99% increases the coherent domain size of domains along the nanowire long-axis by more than a factor of four. OFET characterization of these nanowire films shows that charge transport properties are improved as polymer regioregularity increases, also by a factor of four; this improvement is not as significant in non-nanowire films made from the same series of polymers. The potential to use these high-regioregular nanowires as the donor material within organic electronics represents an opportunity to boost charge transport within a device, potentially leading to an improvement in device performance.

4. Modification of PCBM Crystallization *via* Incorporation of C_{60} in Polymer:Fullerene Solar Cells

4.1. Introduction

As we've discussed above, the most common active layer materials used in the production of OPVs tend to be highly purified conjugated polymers (like P3HT) and fullerene derivatives (like PCBM). The tendency of these materials to crystallize is viewed as critical to achieving the desired bulk-heterojunction morphology.[62-64] However, it is important that overgrowth of these domains does not occur. During processing, needle-like PCBM crystals can develop inside the polymer:fullerene thin-films to form low aspect ratio, micron-scale crystals if the films are annealed for extended periods of time or at very high temperatures.[28-30] These "overgrown" PCBM crystallites decrease the interfacial area between the donor and acceptor domains, representing a critical degradation pathway that can significantly affect the long-term performance and stability of OPVs.[65, 66] Conversely, it is difficult for conjugated polymers to overgrow and form large, low aspect ratio domains. Instead, they have a tendency to form long, high aspect ratio domains with nanometer-scale cross-sectional dimensions.[67] For these polymers, such as P3HT and poly(3-butylthiophene) (P3BT), this more crystalline phase can have a significantly higher charge carrier mobility when compared to the amorphous phase, analogous to the nanowires that we discussed above.

Crystallization for both the polymer and fullerene components in the solid state occurs at temperatures below their common miscibility point (T_{misc} = 205–290 °C for P3HT and PCBM depending on film composition) and above the glass transition of the polymer phase (T_{glass} = 12 °C).[68, 69] There are no evident thermodynamic phase transitions in P3HT:PCBM blends between

these two temperatures.[69] Phase segregation is therefore a thermodynamically driven process that will likely occur at any point within this temperature region. Nevertheless, the kinetics of the crystallization process will vary significantly with factors such as the environmental temperature, the concentration of dissolved PCBM, the viscosity of the polymer matrix, and even the film thickness. Therefore, because of the simultaneous crystallization process, regardless of the specific thermal treatment, the instantaneous morphology that leads to a particular device performance is only a transient one and will likely continue to evolve with time even when the temperature is lowered. While quenching a film from the annealing temperature to ambient conditions slows the evolution of the film morphology, the polymer:fullerene films are still inherently unstable due to the finite solubility and relatively high mobility of PCBM in the amorphous conjugated polymer domains.[70, 71] Films will continue to slowly evolve over time as the crystallization of both components proceeds. Under typical annealing conditions (120 °C < T_{anneal} < 170 °C), this effect manifests itself as a drop in solar cell performance when longer annealing times are used and PCBM crystal domains overgrow. Performance decreases once the crystal size exceeds the optimal size for ideal bulk heterojunctions because the total interface between donor and acceptor domains decreases with increasing domain size. However, even at modest operating temperatures for polymer solar cells (20 °C < T_{op} < 80 °C), slow structural evolution and performance degradation persists as a result of PCBM crystal growth.[61, 72] This degradation mechanism is not only a practical challenge for the optimization of active layer morphology in OVPs, but also for making devices that have adequate lifetimes (years) under normal operating conditions.

Therefore, there is a great need to improve the thermal stability of polymer:fullerene solar cells. This can be done by controlling the crystallization of the fullerene phase. Several strategies are

currently being pursued in the literature. One approach is the synthesis of compatibilizing agents that function to stabilize the polymer:fullerene interface.[73, 74] For example Tsai *et al.* synthesized a poly(4-vinyltriphenylamine)/P3HT copolymer using quasi-living Grignard metathesis and living anionic polymerization.[75] These molecules have the potential to improve long-term thermal stability as they function like surfactants that prevent further coarsening of the polymer and fullerene phases. However, at this point, more study is needed to understand the specific effects these materials have on the morphology of the active layers. Another approach that has been employed is the synthesis of fullerenes with different substitution moieties. Using novel chemical routes, it is possible to synthesize fullerenes that are not capable of packing into uniform crystals; therefore phase segregation is only driven by the crystallization of the polymer phase. This approach has been recently demonstrated with a new PCBM derivative consisting of 1,2-dihydromethano-[60] PCBM by Li *et al.*[76, 77] This approach is highly desirable for conjugated polymers that crystallize into nanofibers because the final domain size is defined by the dimension of the nanofibrils with the fullerene domain acting like a space-filling glassy matrix. However, in cases where the polymer has a relatively low crystallinity or does not form nanofibers, it is also desirable to have the ability to systematically modify the crystallization of the fullerene phase.[78] While these routes show promise, the synthetic complexity and cost associated these materials is not trivial, limiting their commercial viability at this point.

In this work we show that you can introduce C_{60} into the fullerene phase of P3HT/PCBM solar cells in order to systematically modify the crystal habit of PCBM. The solubility of C_{60} in chlorobenzene is only 6–7 mg/mL and this has limited its use in OPVs. Nevertheless, its use has been demonstrated as a pure n-type material for the fabrication of polymer solar cells *via* optimization of solvent conditions.[79] Because C_{60} is a precursor to PCBM and many other

fullerene derivatives, it also has a much lower associated cost and no additional synthesis requirements, which separates it from the methods described above. We show, using optical microscopy and UV-visible absorption spectroscopy, that this approach alters the crystal morphology and greatly reduces the size of fullerene crystallites observed after very long annealing times and under aggressive aging conditions. We also show, by fabricating OFETs from PCBM:C_{60} blends, that the incorporation of C_{60} does not significantly reduce electron mobility in bulk fullerene films. Finally, we show that when C_{60} is incorporated into the fullerene phase of P3HT:PCBM OPVs, devices are more stable to thermal degradation under annealing temperatures and aggressive aging conditions.

4.2. Results and Discussion

4.2.1. P3HT:PCBM:C_{60} Film Characterization

Optical microscopy images and UV-vis absorption spectra of P3HT:PCBM blends spin-coated on glass and annealed at 150 °C are shown in Figure 4.1A and Figure 4.1B respectively. We used these two characterization techniques to monitor the extent of large-scale crystal overgrowth in the films. Image analysis applied to the microscopy images provided a method to quantify a) the total area occupied by visible crystallites, b) their number, and c) their average size. Specific signatures of PCBM overgrowth can also be seen in the UV-vis absorption spectra in Figure 4.1B. After the spectra are normalized to account for differences in film thickness, there is a clear decrease in absorbance at 336 nm as annealing time increases. This peak is the lowest energy absorption feature for PCBM and its decrease indicates the migration of isolated PCBM molecules in the bulk to large PCBM crystallites. Figure 4.1C shows that this decrease at 336 nm begins around 5 min and corresponds almost exactly with a slight increase in the

absorbance background at higher wavelengths (<650 nm). This is expected; large PCBM aggregates should block or scatter a larger fraction of the incident light at all wavelengths.

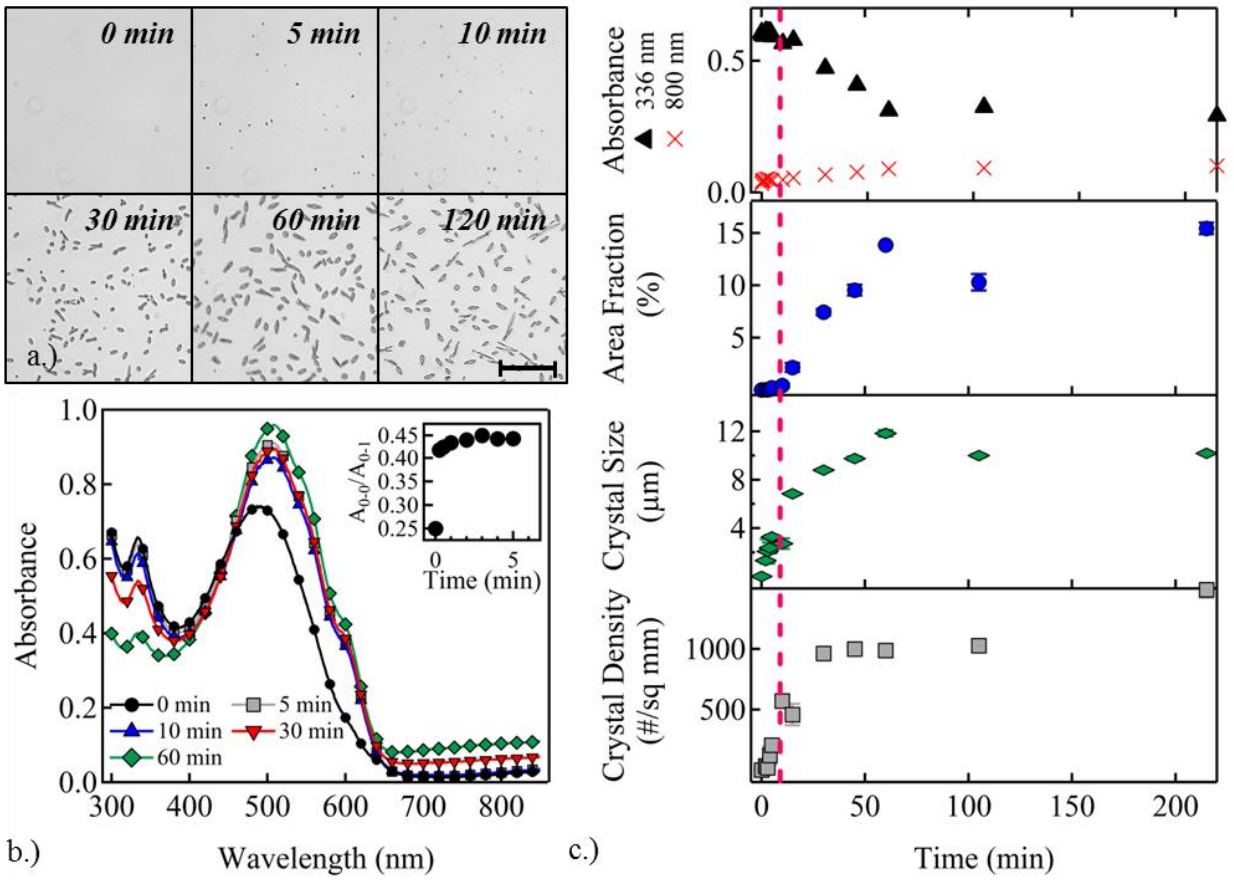

Figure 4.1 a) Optical microscopy images of P3HT:PCBM blends annealed at 150 °C for different times. Scale bar is 100 μm. b) UV-vis absorption spectroscopy of thin films after annealing for different times–inset is the P3HT A_{0-0}/A_{0-1} ratio vs. time. c) Summary of UV-vis absorption and optical microscopy data showing crystallite density, crystallite size, fractional area occupied by the crystallites on the film's surface, and the value of absorbance at λ = 336 nm. The dashed line signifies the formation of visible PCBM aggregates within the film.

Figure 4.1 shows that the growth of micron-sized crystallites began after only 5 min of annealing. At this point, the P3HT has achieved its maximum crystallinity as indicated by the A_{0-0}/A_{0-1} ratio (inset, Figure 4.1B where A_{0-0} = 605 nm and A_{0-0} = 538 nm).[80] Also at this point, the number density and average size of visible crystallites increased rapidly. This also corresponded to a decrease in the PCBM absorption peak at 336 nm. After one hour of annealing, the PCBM

absorption peak at 336 nm stopped decreasing, and a large number of 10 μm crystallites occupied ~15% of the visible film area. The appearance of new micron-sized crystallites slowed at longer annealing times. This is likely a result of the depletion of all of the free PCBM within the bulk of the film. Because optical microscopy is only sensitive to crystals larger than ~1 μm, this analysis does not account for nano-scale PCBM aggregates that are known to form during the early periods of annealing and could still be present even after long periods of annealing.[81] Therefore, these techniques can only quantify a limited region of the kinetics of growth of PCBM crystallites. Grazing incidence small angle X-Ray scattering (GISAXS) measurements were also performed on films to characterize morphological changes occurring at smaller length scales. Typical profiles for bulk heterojunctions containing pure PCBM and mixtures with C_{60} are included in the appendices (Figures 8.5 and 8.6). These results support the existence of a morphological instability occurring in P3HT:PCBM films upon annealing and long term aging. Unfortunately, the exact mechanism of PCBM crystal growth is still a subject of debate and not fully understood. Nevertheless, microscopy and GISAXS data clearly demonstrate the importance of this crystallization process and provide valuable insight regarding the growth of large crystallites in bulk heterojunctions composed of P3HT/PCBM.

Figure 4.1 also shows that, after an initial nucleation period, visible PCBM crystallites grow larger and become more abundant. This growth must occur through the migration of dissolved PCBM from disordered regions of the polymer matrix until the chemical potential of PCBM in the amorphous P3HT is balanced with the chemical potential of PCBM in the crystalline phase. Therefore, the ultimate size and number of micron-sized crystallites observed in these films is a complex function of the solubility and mobility of PCBM in the polymer matrix, the number of nucleation sites, the crystallinity of the polymer within the film, and the film composition.

Therefore, for the addition of C_{60} to the fullerene phase of polymer:fullerene blends to be effective, it must modify the growth kinetics of the fullerene crystallites such that the extent of fullerene overgrowth is reduced.

In order to quantify the extent of overgrowth that occurs when C_{60} is incorporated into the fullerene phase of P3HT:PCBM blends, we also fabricated P3HT:PCBM:C_{60} blends while maintaining a constant P3HT:fullerene weight ratio but varying the PCBM:C_{60} content in the fullerene phase. Figure 4.2a shows the optical microscopy images of P3HT:fullerene films with increasing C_{60} content in the fullerene phase. These films were annealed at 150 °C for 2 h. After applying the same analysis to these images as with pure P3HT/PCBM blends, Figure 4.2b shows the number density and the average size of visible aggregates as a function of PCBM:C_{60} content in the fullerene phase. Scanning electron microscopy images of PCBM:fullerene films annealed at 150 °C for 1 h are also shown in Figure 4.2 to access smaller length scales.

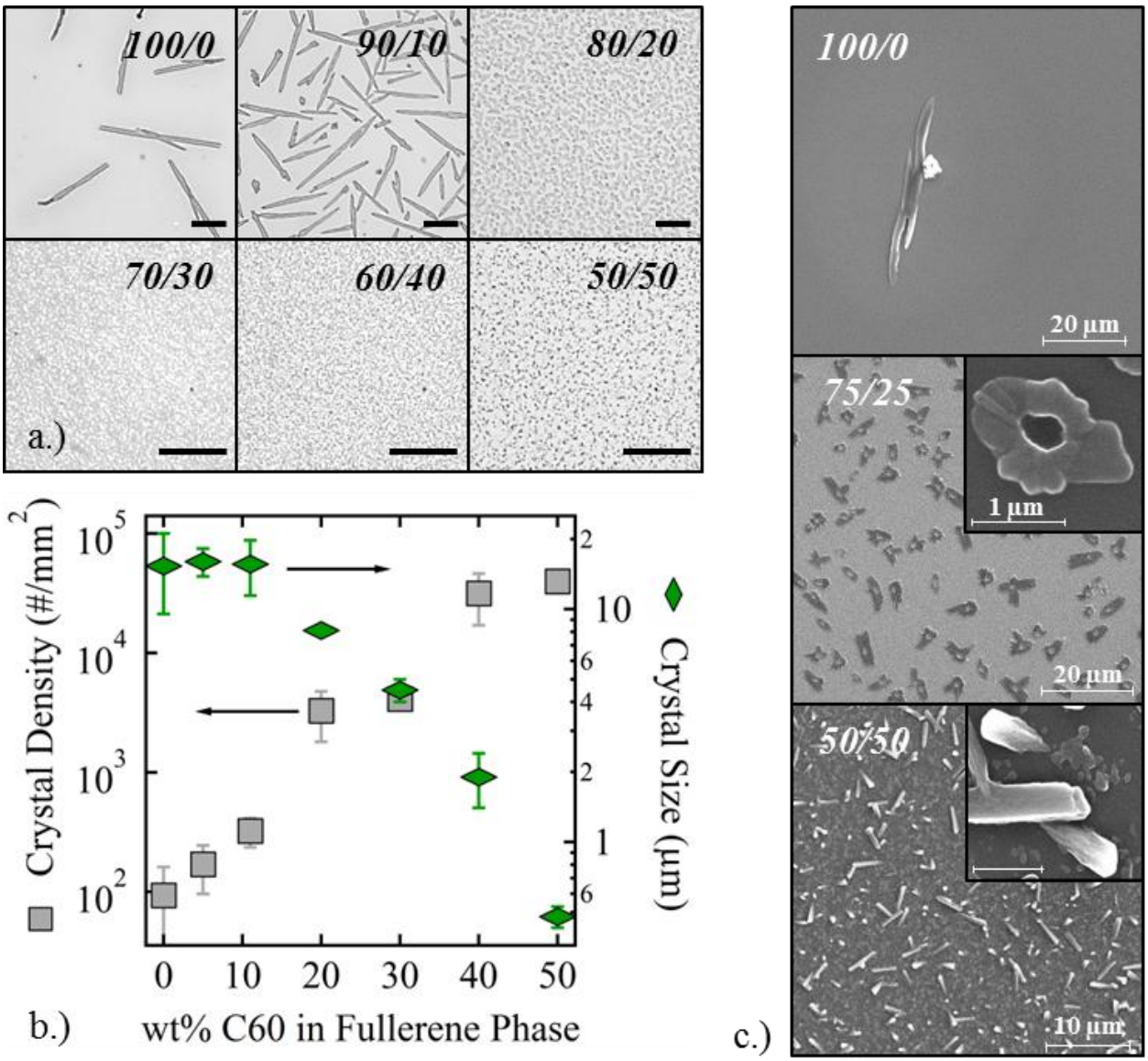

Figure 4.2 a) Optical microscopy images of films with varying PCBM:C_{60} content in the fullerene phase of a P3HT:fullerene film annealed for 2 h at 150 °C. Scale bar is 50 µm. b) Summary of the average crystal size and number of visible "overgrown" crystals at 2 h annealing. c) Scanning electron microscopy images of PCBM:C_{60} films after 1 h annealing at 150 °C on silicon wafers.

These images clearly show that the extent of overgrowth is strongly dependent on the fullerene composition in these films. From the optical microscopy images, it is clear that the presence of C_{60} causes a significant increase in the number density of crystallites while also simultaneously decreasing the average size of the visible overgrown crystals. The SEM images in Figure 4.2c also show that the morphology of the individual crystallites was significantly affected by the

incorporation of C_{60} into the fullerene phase. As the C_{60} content is increased to 25 wt% in the fullerene phase, the crystallites are clearly much less needle-like and instead form disc-like or flower-like structures. As the C_{60} content in the fullerene phase increases to 50 wt%, the apparent crystal size decreases further and the morphology becomes increasingly faceted. The degree to which crystals overgrow also appears to decrease but they tend to form faster during annealing (see Figure 8.7 in the appendices). While films without C_{60} took more than 1 h at 150 °C to reach a fully stabilized morphology, very small quantities of C_{60} in the fullerene phase resulted in extensive crystallization within 5–10 min of annealing at 150 °C. However, once this initial growth ceased, the crystals maintained their smaller size even after very long annealing periods at 150 °C.

In order to test the stability of P3HT:fullerene blends that incorporate C_{60} against accelerated aging conditions, films with varying PCBM:C_{60} content were annealed at 150 °C and then aged at 90 °C. 90 °C is somewhat higher than what might be expected for typical solar-cell operating conditions but it is also lower than typical annealing temperatures. This experiment was also designed to test whether high-temperature annealing alone provided enhanced thermal stability for devices during operation since it had been previously proposed that annealing at higher temperatures stabilized P3HT:PCBM blends.[65] These films were again monitored using optical microscopy as shown in Figure 4.3.

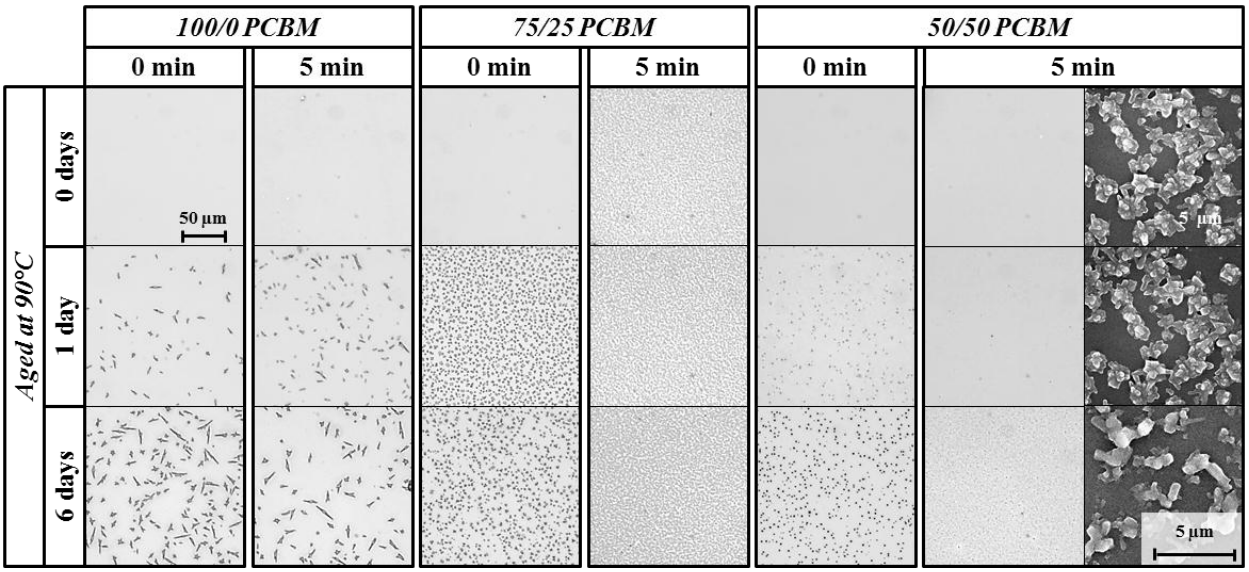

Figure 4.3 Optical microscopy images of films with varying PCBM:C_{60} that have been annealed at 150 °C (for either 0 or 5 min) and aged at 90 °C (for 0, 1, and 6 days). The right-most column shows scanning electron microscopy images of the 50/50 films annealed for 5 min and aged for varying times.

In order to better resolve small crystallites, SEM images were also taken for samples corresponding to the optical microscopy images of films annealed for 5 min at 150 °C and then aged at 90 °C. UV-visible absorption spectra were also obtained for these films and are presented in Figure 4.4 along with the analysis of crystal sizes for each film. After 6 days of aging at 90 °C, the P3HT:fullerene films with 100:0 PCBM:C_{60} composition in the fullerene phase resulted in the same final aggregate size of ≈10 µm regardless of the annealing condition. This observation is contrary to some reports claiming that high temperature annealing stabilizes P3HT:PCBM blends to crystal overgrowth.[41] Interestingly, annealing the 50:50 PCBM:C_{60} blend did make the films significantly more stable to overgrowth when compared to films that were not annealed before aging. Aging the P3HT:fullerene blends with 50:50 PCBM:C_{60} for 6 days resulted in crystals with an average size of 3 µm if they were not annealed first. However, identical films subjected to just 5 min of annealing at 150 °C resulted in ≈300 nm crystals after 6 days of aging. This represents an order of magnitude difference in crystal size when devices are annealed.

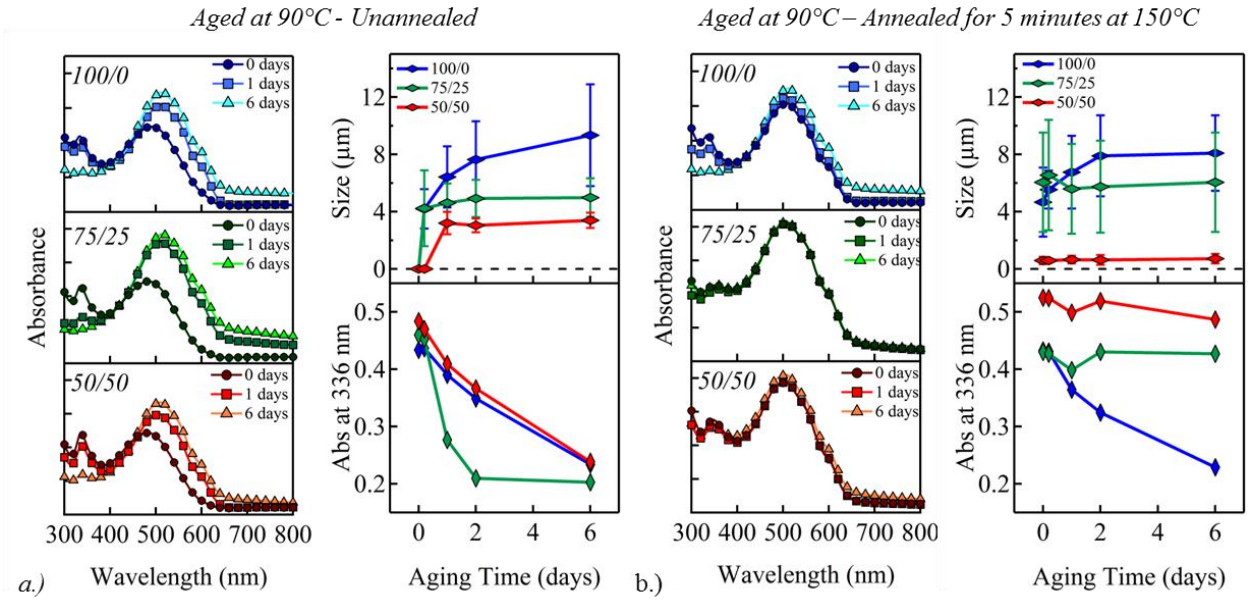

Figure 4.4 A) P3HT:fullerene films with varying PCBM:C_{60} content aged at 90 °C without annealing. B) P3HT:fullerene films with varying PCBM:C_{60} content annealed for 5 min at 150 °C and then subsequently aged at 90 °C.

The UV-Vis absorption spectra shown in Figure 4.4 provide further insight into the crystal overgrowth observed in Figure 4.3. Regardless of the composition of the fullerene phase, the absorption peak at 336 nm decreased and the average crystal size increased as a function of aging time when the films were not annealed. Therefore, aggregates large enough to be fully opaque to the spectrometer were forming throughout the films. For the annealed 100:0 PCBM:C_{60} film, the absorbance behavior was very similar to when it was not annealed. This is not surprising considering that the long-time scale of PCBM overgrowth leaves plenty of free PCBM to continue to diffuse to growing crystallites when no C_{60} is present. For the annealed 75:25 PCBM:C_{60} film, after 5 min of annealing, large aggregates have already formed on the surface and the absorbance at 336 nm has already decreased. Therefore, aging the film at 90 °C had very little effect on the crystal size and absorbance at 336 nm. This was also the case for the 50:50 PCBM:C_{60} films. Interestingly, the absorbance at 336 nm stayed relatively constant even when

compared when the film was not annealed. This verifies that the crystallites formed in this film are sufficiently small so that they are still transparent to the spectrometer and they are also more stable to further growth than films that do not incorporate C_{60}. The intermediate compositions shown in Figure 4.2b were also evaluated using this methodology and found to be consistent with the general trend that smaller, more numerous aggregates exhibit improved thermal stability.

4.2.2. PCBM:C_{60} Organic Field-Effect Transistors (OFETs)

To this point, our work has focused primarily on characterizing the extent of overgrowth of PCBM crystallites from P3HT:fullerene films after different thermal treatments with varying PCBM:C_{60} composition in the fullerene phase. This characterization showed that, at higher C_{60} loadings, PCBM crystal overgrowth is reduced and the morphology is modified. Results also suggest that this approach could lead to more thermally stable OPVs. However, for this approach to be viable, the modification of the morphology of the fullerene phase must occur without a significant reduction of the electron transport properties in the fullerene phase. To test the effect of the addition of C_{60} on the electron mobility of the PCBM phase, we fabricated OFETs from PCBM:C_{60} solutions with varying C_{60} content (no P3HT). Figure 4.5a shows the measured field-effect mobility and threshold voltage from these devices, while Figure 4.5b shows representative current–voltage (I–V) curves for each set of processing conditions.

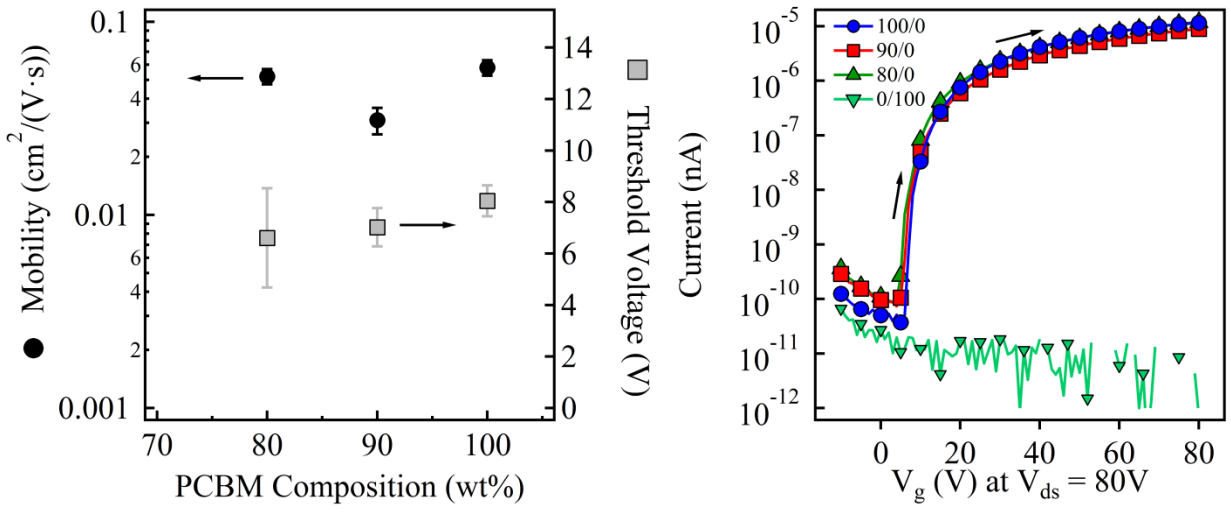

Figure 4.5 A) Electron mobility and threshold voltage as a function of PCBM composition. B) Forward sweep of transfer curve for OFETS made from PCBM:C_{60} blends of different composition.

Overall, the electron mobility decreases slightly with the addition of C_{60} to PCBM with values of 0.05 cm^2/V s in pure PCBM and 0.03–0.04 cm^2/V s in the PCBM/C_{60} mixtures. This observation is not surprising given that prior theoretical work has also shown little effect of different polycrystalline structures on the electron mobility of pure C_{60} transistors.[82] The poor performance of the 0:100 PCBM:C_{60} devices is a result of poor film adhesion to the substrate. In fact, films prepared with PCBM content below ≈75 wt% did not form films of sufficient quality to be tested using this approach. These measurements reveal small variations in the electron mobility values of a pure PCBM:C_{60} phase. However, as mentioned previously, electron mobility is also a complex function of the interconnectivity that exists between different fullerene domains, their orientation, size, and shape. This is also equally true for the hole mobility corresponding to P3HT domains within bulk heterojunction devices. Generally, mobility measurements on P3HT:PCBM blends result in one order of magnitude reductions in the electron and hole mobility values with respect to measurements in the pure materials.[83] Therefore, the OFET measurements that we present here are only meant to characterize potential

reductions in mobility that could occur within pure fullerene domains; these values are not representative of the effective mobility that is measured in a bulk heterojunction device. The charge carrier mobility values in solar cells are affected by many other parameters and this makes it very difficult to isolate and characterize each contribution independently.

4.2.3. P3HT:PCBM:C_{60} Organic Photovoltaics

The morphological studies of the effects of C_{60} additions into the fullerene phase of P3HT:PCBM blends have, to this point, been based on experiments conducted on 'free' films coated on glass/SiO_2. There are a number of studies that show that the presence of a top electrode on P3HT/PCBM active layers can significantly affect the kinetics of PCBM diffusion and also modify the extent of vertical phase segregation.[40, 42] Therefore, it is difficult to directly infer device performance from without a confining top electrode. In order to test whether the incorporation of C_{60} into the fullerene phase of P3HT:fullerene films really yields thermally stable OPVs, we have fabricated devices with an aluminum electrode evaporated onto the active layer before applying the thermal treatment. The performance of the OPVs was then tested after different annealing treatments. The first treatment consisted of an annealing time study at 150 °C. As shown in Figure 4.6a, the 100:0 PCBM/C_{60} devices show the best peak power conversion efficiency, 3.3% ± 0.3%, after 10 min of annealing. The 75:25 PCBM:C_{60} and 50:50 PCBM:C_{60} devices' peak efficiencies occurred after only 5 min of annealing and had values of 2.5% ± 0.4% and 2.2% ± 0.3% respectively. However, the performance achieved for the 50:50 PCBM:C_{60} devices after annealing for 120 min was still 91% of its original value whereas the performance of the 100:0 PCBM:C_{60} devices were already at 68% of their peak performance. We also performed an aging study where devices annealed for 5 min at 150 °C were subsequently placed at an elevated temperature (90 °C) for a longer time and tested periodically to evaluate

performance. The results of this test are shown in Figure 4.6c and further broken down in Figure 4.7.

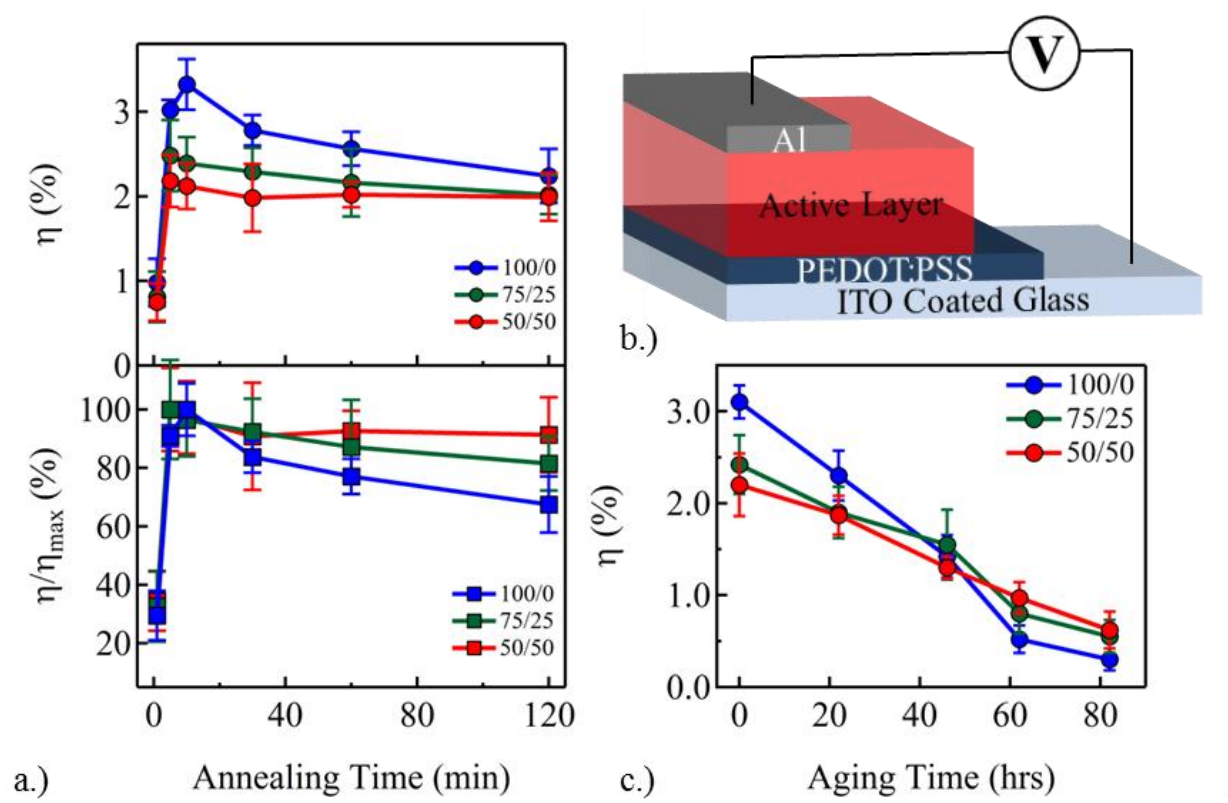

Figure 4.6 a) Efficiency and normalized efficiency of P3HT:fullerene devices with varying C_{60} content as a function of annealing time. b) Schematic of OPVs fabricated for this study. c) Efficiency of P3HT:fullerene devices with varying C_{60} content as a function of aging time after being annealed for 5 min at 150 °C.

After 80 h of aging, significant degradation of performance of all devices in the study was observed. The 100:0 PCBM:C_{60} devices' performance degraded 90% from 3.2% ± 0.2% to 0.3% ± 0.2%. Comparing these results to the devices incorporating C_{60}, the 75:25 PCBM:C_{60} devices degraded 78% from 2.4% ± 0.4% to 0.6% ± 0.2%, and the 50:50 PCBM:C_{60} devices degraded 71% from 2.2% ± 0.3% to 0.7% ± 0.2%. Therefore, under extreme accelerated aging conditions, the 50:50 PCBM:C_{60} devices did show a significant improvement over the 100:0 PCBM:C_{60} devices both in terms of relative performance to its peak efficiency and also in final efficiency.

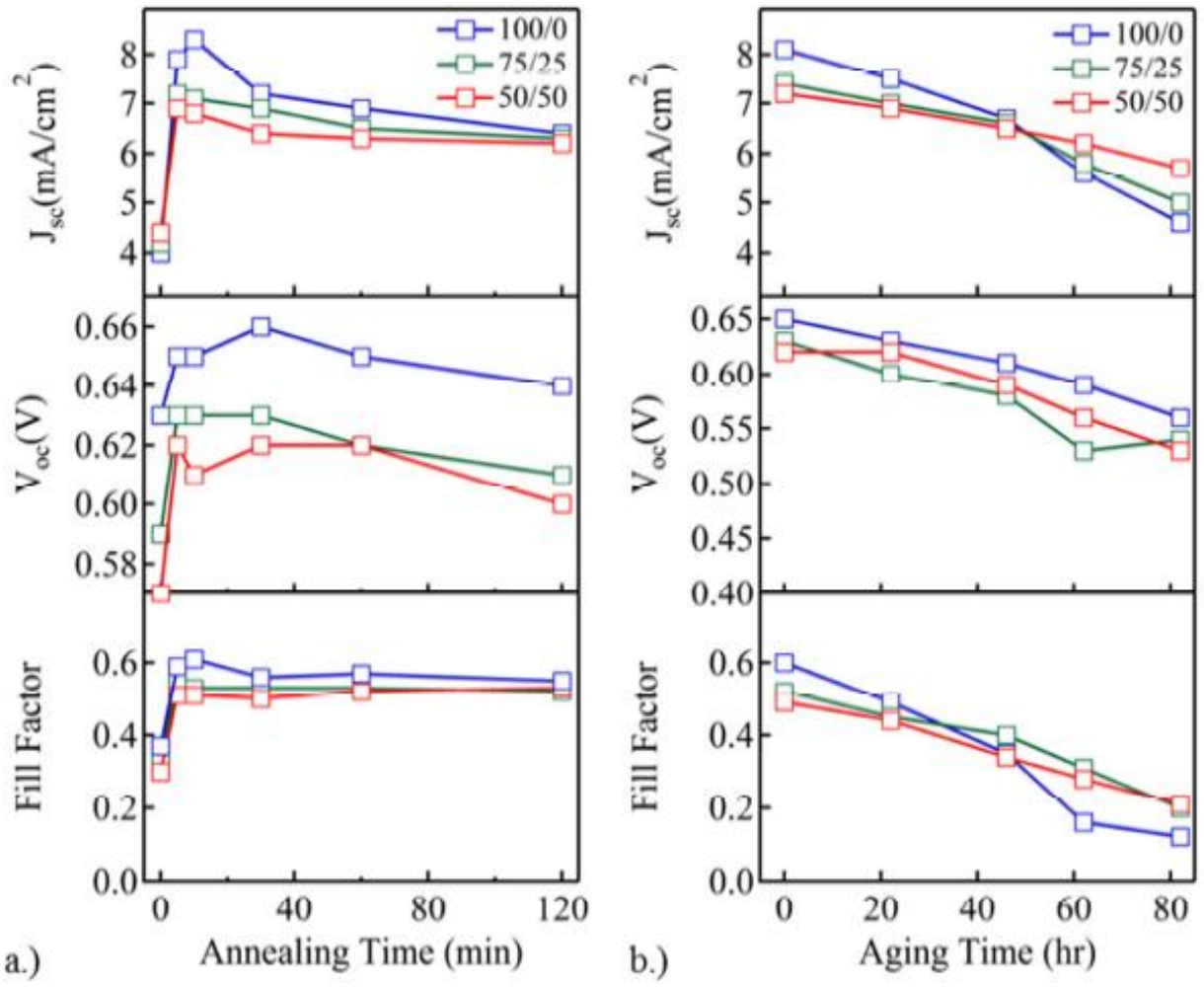

Figure 4.7 Short circuit current (J_{sc}), open circuit voltage (V_{oc}), and the fill factor for P3HT:fullerene blends with varying PCBM/C60 content that were a.) annealed at 150°C and b.) annealed for 5 minutes and then aged at 90°C.

The device performance data shown in figures 4.6 and 4.7 demonstrates that C_{60} incorporation into the fullerene phase of P3HT:PCBM solar cells can be used to improve the thermal stability of devices under accelerated aging conditions. The performance characteristics of P3HT:PCBM:C_{60} devices are also consistent with the observations made of open-faced films that were annealed and aged under similar thermal conditions. Particularly relevant is the absorbance of the PCBM peak at 336 nm. The 50:50 PCBM:C_{60} blend maintained a relatively constant absorbance that was greater than 100:0 PCBM:C_{60} films after extended periods of annealing and

aging. In both cases, the maintenance of this peak is correlated to improved relative performance and in the case of aging, an overall better absolute efficiency. This suggests that the smaller crystal size formed in the 50:50 PCBM:C_{60} films observed with microscopy is also maintained in devices with confining electrodes that were made with the same composition. Therefore, the improvement relative to the pure PCBM films is likely caused by an increase in the interface between P3HT and PCBM and possibly by a prevention of mechanical damage to the devices as a result of very large aggregate growth. It is important to note that the devices fabricated here were prepared using the same optimized conditions for P3HT/PCBM solar cells without C_{60} incorporation. Therefore, the efficiency of devices incorporating PCBM/C_{60} devices could potentially be further optimized to improve the peak efficiencies achieved in these studies. Furthermore, it may be possible to also utilize other fullerene mixtures (C_{60}, C_{70}, $PC_{61}BM$, $PC_{71}BM$ and others) to further reduce the driving force to form crystals without affecting the electron mobility of the fullerene phase. This is the subject of ongoing research.

4.3. Conclusions

In this work, we characterize the effects of C_{60} incorporation into the fullerene phase of P3HT:PCBM active layers as a simple approach to modify the growth of micron-sized PCBM crystallites. We find that the incorporation of even small amounts of C_{60} had a dramatic effect on the nucleation and growth of PCBM crystallites. Increasing the amounts of C_{60} in the bulk heterojunction films was also found to systematically modify the fullerene crystal size and morphology. We also showed that the P3HT:fullerene active layers that incorporated 50:50 PCBM:C_{60} in the fullerene phase had a greater thermal stability under aggressive aging conditions if they were annealed for a short time at 150 °C. We also fabricated OPVs that incorporate different amounts of C_{60} in their active layers and found that, under aggressive aging

conditions, the addition of C_{60} offered improvements on the thermal stability of devices when compared to devices fabricated without C_{60} incorporation. From open-film studies of P3HT:PCBM:C_{60} blends, it appeared that the improved stability was a result of a faster nucleation process that resulted in a larger number of much smaller fullerene crystallites. The size of fullerene crystallites ranged from 200 nm to 10 μm depending on the C_{60} loading and the crystallization conditions. Based on this work, we demonstrated that using mixtures of fullerenes in OPVs is a simple approach to improving the thermal stability of organic devices.

5. Benzo[2,1-b;3,4-b']dithiophene-Based Low Bandgap Polymers for Photovoltaic Applications

5.1. Introduction

Currently, efficiencies up to 5% have been achieved using poly[2-methoxy-5-(3′,7′-dimethyloctyloxy)-1,4-phenylene vinylene] (MDMO-PPV) and P3HT as the donor material and the soluble fullerene derivative PCBM as the acceptor.[84, 85] These material combinations are used in some of the most researched, best understood OPVs systems. However, further improvement of MDMO-PPV- or P3HT-based devices is difficult because of intrinsic absorption limit.[86] Therefore, developing low-bandgap polymers to capture more solar photons provides an alternative approach for achieving higher PCEs.[13-15, 87, 88]

Benzo[2,1-*b*;3,4-*b*′]dithiophene (BDP) is a 2,5-connected dithiophene derivative that is fused with a benzene ring. The benzene core decreases the electron richness of the flanked bithiophene unit, which provides a low-lying HOMO energy level.[89, 90] The extended π system also helps to form highly ordered films that facilitate charge-carrier transport. Recently, Müllen *et al.* reported a series of BDP-containing polymers which exhibit a relatively high charge: up to 0.5 $cm^2\ V^{-1}\ s^{-1}$.[91] The combination of the low-lying HOMO level and the high hole mobilities make BDP-containing polymers particularly attractive for OPVs. In our work, in an attempt to improve upon existing BDP-containing polymers, several typical electron-deficient heterocycles were selected as acceptor units within the polymer backbone to decrease the bandgap of the materials and to tune the energy levels. The chosen structures of the polymers are shown in Figure 5.1.

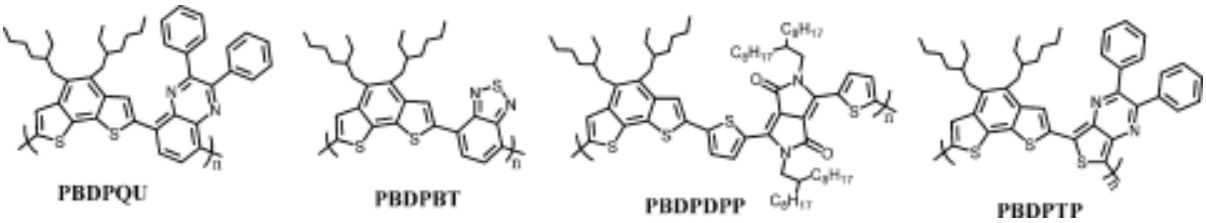

Figure 5.1 Structure of BDP-based copolymer with different building blocks.

Here, we report on the characterization and preliminary OPV performances of four BDP-containing alternating polymers. The goal of this work is to identify a trend in performances within a particular series of polymers.

5.2. Synthesis

Synthesis of these polymers was completed by Dr. Mingjian Yuan.[16]

5.3. Results and Discussion

5.3.1. Optical and Electrochemical Properties

The photophysical characteristics of the polymers were investigated by UV–vis absorption spectroscopy in dilute chloroform solutions and as spin-coated films on quartz substrates. Figure 5.2 shows the absorption spectra of the PBDPQU, PBDPBT, PBDPDPP, and PBDPTP in chloroform and as a thin film on substrates.

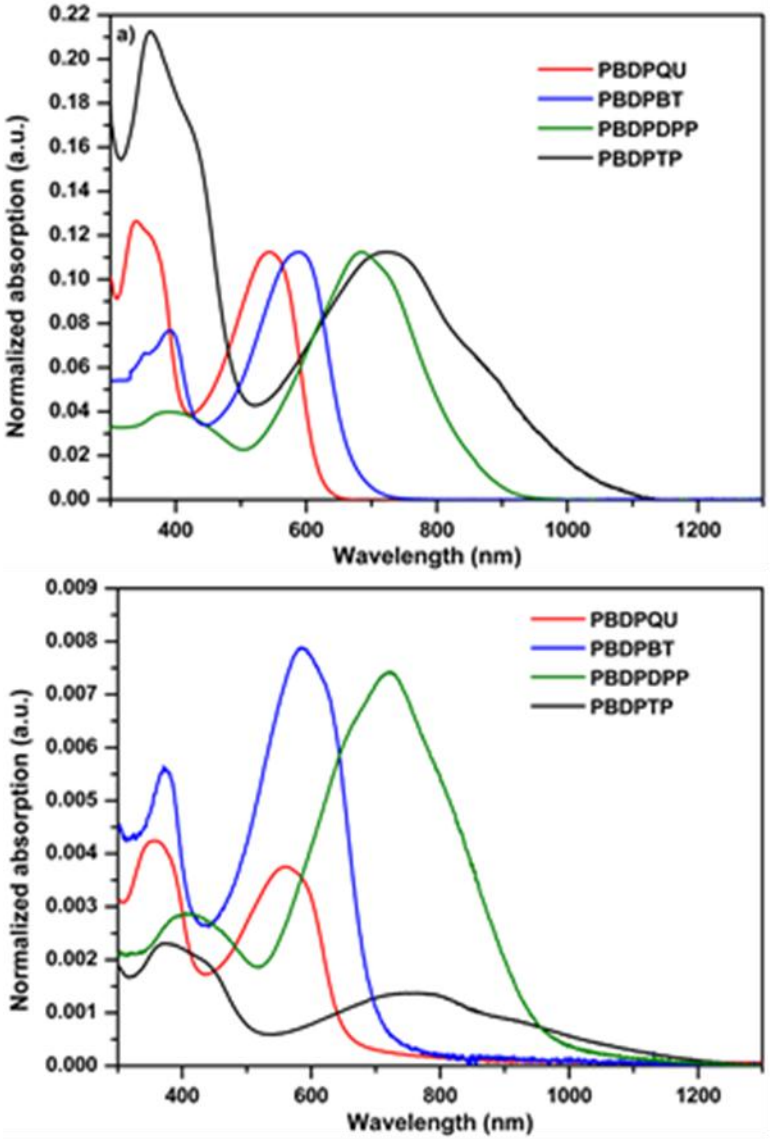

Figure 5.2 UV–vis absorption spectra of polymers in (a) dilute $CHCl_3$ and (b) thin films on quartz substrates. In (a) absorption is normalized by the corresponding λ_{max} at the longer wavelength, and in (b) absorption is normalized by thin film thickness.

As shown in Figure 5.2a, all the absorption spectra in dilute chloroform show two absorption bands. Each polymer has an absorption band located between 300 and 500 nm with a second broad absorption band from 500 to 1100 nm. Absorption spectra of these four polymers extend into the near-infrared (NIR) region, and the peaks are located at 722, 685, 584, and 544 nm for PBDPTP, PBDPDPP, PBDPBT, and PBDPQU, respectively. The long-wavelength absorption

bands are due to the ICT process between the BDP moiety and the electron-accepting QU, BT, DPP, and TP units. The trend in increasing values of the λ_{max} in the absorption spectra has been observed before in other donor:acceptor systems, where the trend was ascribed to increasing acceptor strengths (QU < BT < DPP < TP).[92] From Figure 5.2b, it can be seen that all four polymers show extended absorption edges in thin films in the NIR region, which can be attributed to the more aggregated configuration formed in the solid state. The corresponding absorption edges can be used to calculate the optical bandgap for each polymer. This data is summarized in Table 5.1.

Table 5.1 The UV–vis Absorption, Electrochemistry Data, Optical Gap, Electrochemical Bandgap of BDP-Based Copolymers, and the Calculated HOMO Level for Corresponding Comonomer.

Co-polymer	UV-Vis absorption			Optical	Electrochemistry Data			Co-monomer
	$\lambda_{max\text{-}sol}$	$\lambda_{max\text{-}film}$	$\lambda_{onset\text{-}film}$	E_g	HOMO	LUMO	E_g	Calculated HOMO
PBDPQU	544 nm	562 nm	693 nm	1.79 eV	-5.16 eV	-3.34 eV	1.82 eV	-5.54 eV
PBDPBT	584 nm	593 nm	734 nm	1.69 eV	-5.30 eV	-3.53 eV	1.77 eV	-5.72 eV
PBDPDPP	685 nm	725 nm	961 nm	1.29 eV	-5.21 eV	-3.60 eV	1.61 eV	-5.68 eV
PBDPTP	722 nm	791 nm	1148 nm	1.08 eV	-5.01 eV	-3.63 eV	1.38 eV	-5.24 eV

The bandgap was also measured from electrochemical cyclic voltammetry (CV). This analysis was also completed by Dr. Mingjian Yuan.[16] Bandgaps measured using CV were slightly larger than those obtained from the absorption spectra; this same phenomenon has been observed previously with other BDP-based copolymers.[10, 77] The optical bandgap was effectively lowered using the donor–acceptor approach, which should improve the light harvesting when the polymers are used in photovoltaic devices.

The HOMO and LUMO levels are included in Table 5.1 and illustrated graphically in Figure 5.3.

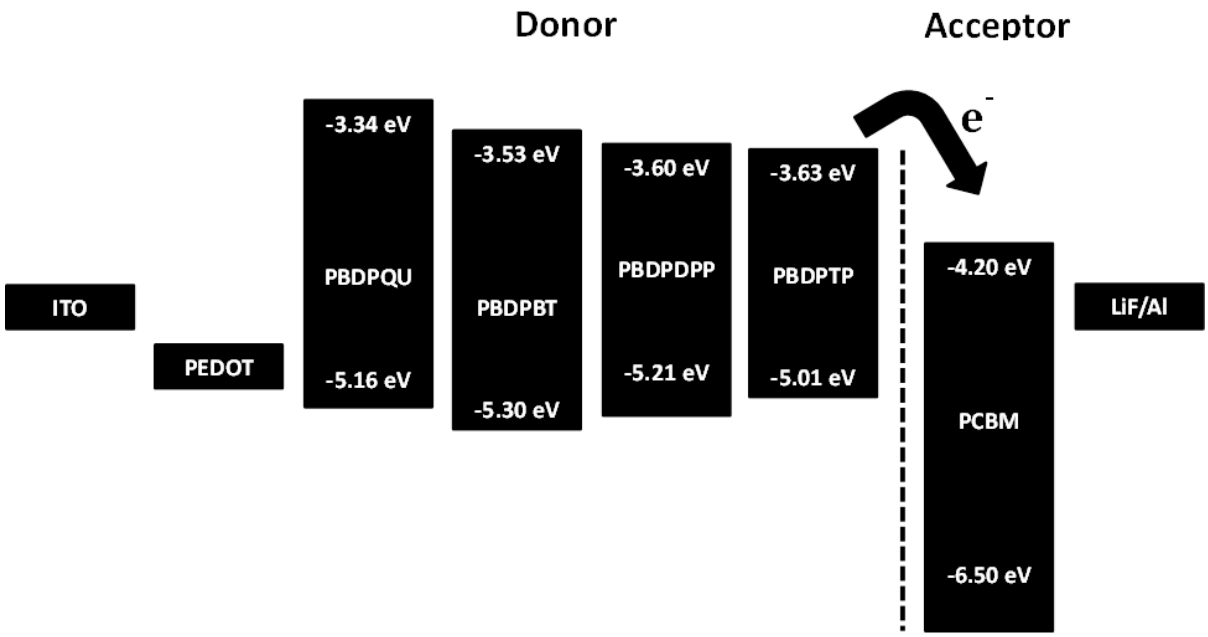

Figure 5.3 Energy level diagrams for PBDPQU, PBDPBT, PBDPDPP, and PBDPTP.

As previously mentioned, the low-lying HOMO levels of these donor polymers are essential for achieving large V_{OC} values in photovoltaic devices because the V_{OC} is closely related to the energy difference between the HOMO of the electron-donor polymer and the LUMO of the electron-acceptor. From these results, we can see that bridging various acceptor units with intrinsically different electron-accepting capabilities to the BDP moiety allows for moderate modulation of the bandgap and energy level of the resulting polymers. Also, we conclude that both a low HOMO level and a low bandgap were obtained from the BDP-based copolymers confirming the theoretical calculations we obtained for the model compounds; these offer a chance to obtain improved V_{OC} and J_{SC} in OPV devices.

5.3.2. Photovoltaic Properties

BHJ solar cells were fabricated using PBDPTP, PBDPDPP, PBDPBT, or PBDPQU and either $PC_{71}BM$ or $PC_{61}BM$ to determine the photovoltaic properties of the polymers. Processing

conditions for these devices, are similar to procedures used in the literature for other low-bandgap polymers,[90, 92] but it is important to remember that these conditions have not been optimized for the materials used in this study. At least 24 devices were analyzed for each polymer under the specified processing conditions. Reported values are the mean results generated from these tests. Figure 5.4 shows representative *J–V* curves for all eight systems. Full photovoltaic properties are summarized in Table 5.2.

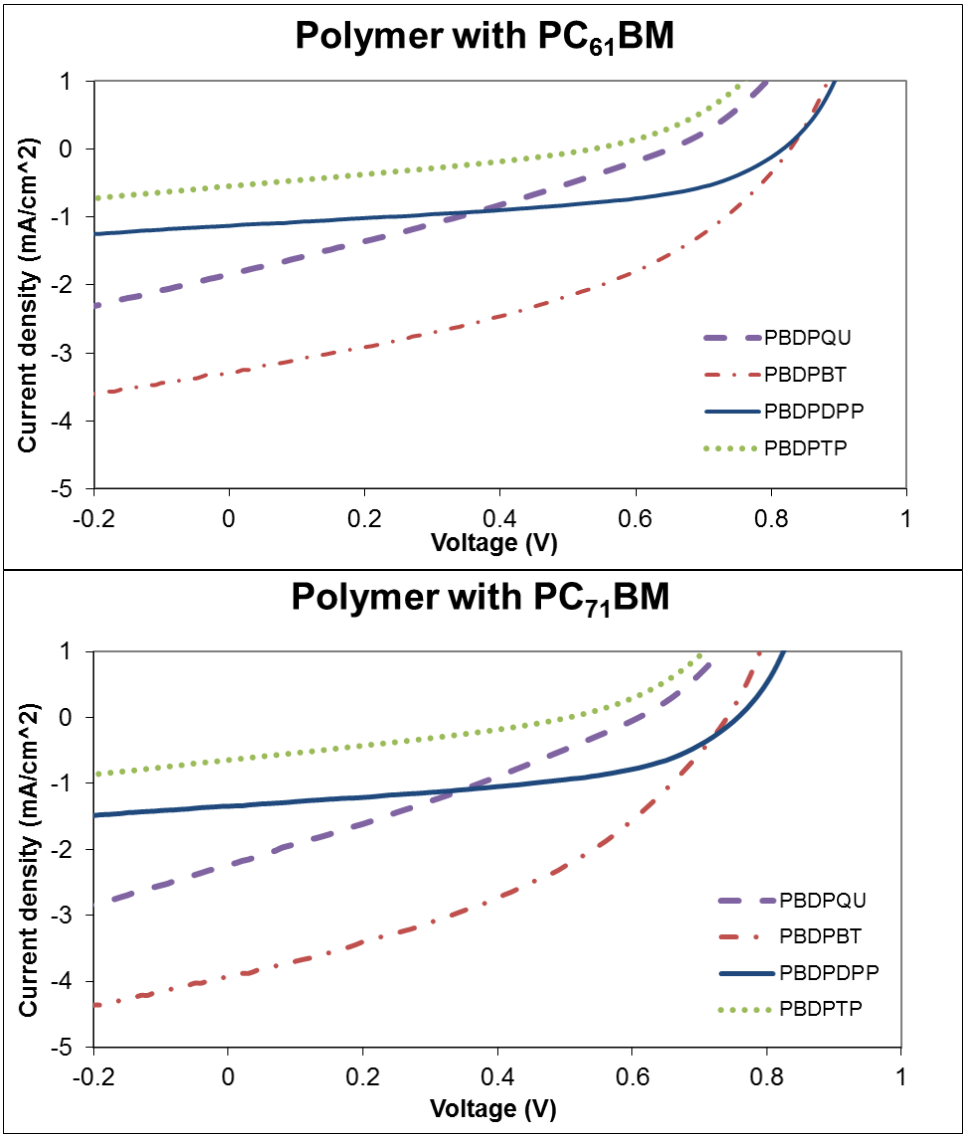

Figure 5.4 Representative J–V curves for devices made with PBDPQU, PBDPBT, PBDPDPP, and PBDPTP and either $PC_{61}BM$ or $PC_{71}BM$.

Table 5.2 Photovoltaic Properties of BDP-Based Polymer/PCBM Devices.

Donor	Acceptor	V_{OC} (V)	J_{SC} (mA/cm^2)	FF	PCE (%)
PBDPQU	$PC_{61}BM$	0.65 ± 0.02	1.84 ± 0.23	0.28 ± 0.02	0.33 ± 0.08
PBDPBT	$PC_{61}BM$	0.81 ± 0.01	3.24 ± 0.41	0.39 ± 0.02	1.04 ± 0.11
PBDPDPP	$PC_{61}BM$	0.82 ± 0.02	1.13 ± 0.18	0.47 ± 0.04	0.43 ± 0.12
PBDPTP	$PC_{61}BM$	0.54 ± 0.02	0.50 ± 0.12	0.30 ± 0.03	0.08 ± 0.03
PBDPQU	$PC_{71}BM$	0.61 ± 0.03	2.24 ± 0.21	0.29 ± 0.02	0.39 ± 0.09
PBDPBT	$PC_{71}BM$	0.75 ± 0.02	3.93 ± 0.44	0.38 ± 0.03	1.11 ± 0.10
PBDPDPP	$PC_{71}BM$	0.76 ± 0.01	1.35 ± 0.20	0.47 ± 0.02	0.48 ± 0.08
PBDPTP	$PC_{71}BM$	0.50 ± 0.02	0.65 ± 0.10	0.29 ± 0.02	0.09 ± 0.02

Each of these devices exhibits a relatively low fill factor, with none surpassing 0.47. This poor performance is likely caused by the lack of optimization of our devices. It has been shown that both annealing conditions and active layer thickness significantly impact the fill factor of a device;[93] neither of these processing steps was optimized in this study. Greater optimization of processing would likely lead to a significant impact in measured fill factors and device performance.

The V_{OC} obtained from the device measurements using $PC_{61}BM$ are 0.65 V for PBDPQU, 0.81 V for PBDPBT, 0.82 V for PBDPDPP, and 0.54 V for PBDPTP. The order of the V_{OC} values is in good agreement with the HOMO energy level of the polymers. It is worth mentioning that the V_{OC} is close to the difference between the HOMO energy level of the polymer and the LUMO level of PCBM after correcting for an expected voltage loss of around 0.2 V at each electrode because of band bending.[94] The high V_{OC} of PBDPBT and PBDPDPP (0.81 and 0.82 V,

respectively) is indicative that BDP plays an important role in lowering the HOMO level of the polymer, which is also in agreement with the results from the CV measurements.

Out of this series of polymers, PBDPBT devices were found to have the highest J_{SC} values, averaging 3.24 mA cm^{-2}. This J_{SC} value, combined with a fill factor of 0.39 and a V_{OC} of 0.81 V, yielded an overall PCE of 1.04%. The J_{SC} values for PBDPQU, PBDPDPP, and PBDPTP were considerably lower, leading the efficiency to be 0.33, 0.43, and 0.08%, respectively.

As expected, devices with $PC_{71}BM$ have significantly improved J_{SC} values, with values increasing by at least 20% for each of the four polymers. This is likely due to an increase in absorption by the acceptor material. The use of $PC_{71}BM$ as a substitute for $PC_{61}BM$ has been shown to increase J_{SC} by up to 50%.[95] Conversely, the V_{OC} between devices with $PC_{71}BM$ and $PC_{61}BM$ seems to demonstrate a systematic decline of about 8%. This effect has been demonstrated in the literature and is largely caused by the slightly lower LUMO of $PC_{71}BM$ compared with $PC_{61}BM$ (−3.75 eV vs. −3.70 eV).[96] PBDPBT again produced the best performing device, with efficiencies above 1.1% when combined with $PC_{71}BM$. The relatively high V_{OC} of PBDPBT demonstrates the efficacy of adding a weak donor group to reduce the HOMO level.

The V_{OC} of the devices are close to what we would expect based on the polymer HOMO levels calculated above. However, the variations in J_{SC} are more difficult to explain. It is well known that the device performance can be drastically affected by differences in morphology. However, our atomic force microscopy (AFM) phase images (Figure 5.5) show no discernible difference between the four devices. Domains for both the acceptor and donor are on the order of 10 nm. Films obtained from devices made with $PC_{71}BM$ were also similar in morphology for each of the

four polymers. This indicates that differences in domain sizes are not likely to have caused the variations in J_{SC} shown in Table 5.2, and that the differences in J_{SC} are more likely due to the optoelectronic properties of the polymers.

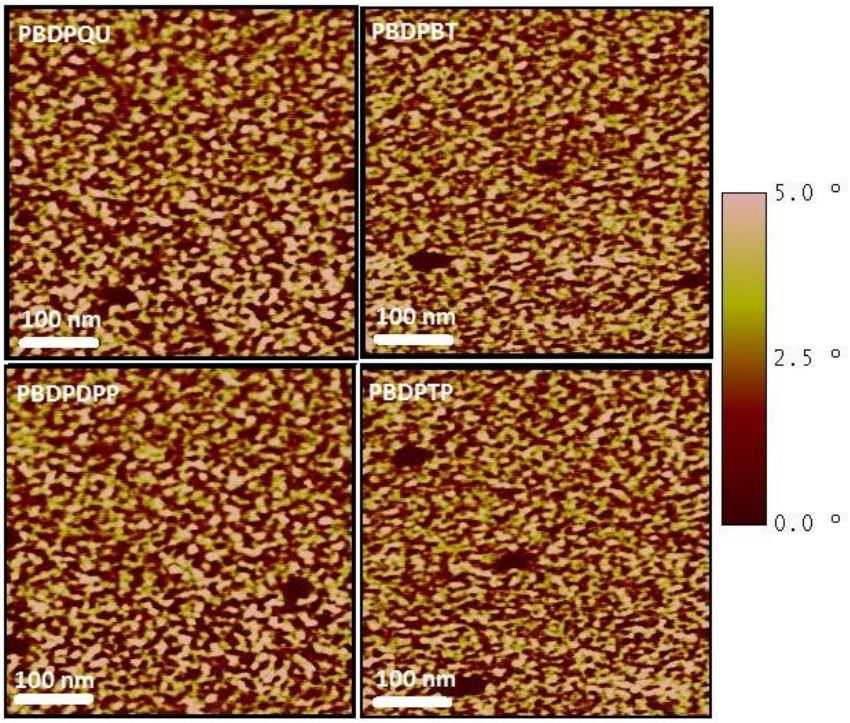

Figure 5.5 Phase images of OPV surfaces showing polymer and PCBM domain sizes.

The basic operational principles for OPVs are the following: (i) light absorption followed by exciton formation; (ii) exciton dissociation; and finally (iii) charge collection. To identify the differences in OPV performance between the four polymers, we looked into the variations in each different step between the four polymers.

5.3.2.1. Light Absorption

Based on the bandgap of the polymers alone, one would expect the lowest bandgap material PBDPTP to provide the highest J_{SC} and either PBDPQU or PBDPBT to provide the lowest J_{SC}.

However, that is clearly not the case. Figure 5.2b shows the UV–vis thin film spectra of the four polymers normalized based on film thickness. The spectra demonstrate that, as a thin film, PBDPTP absorbs significantly less light than any of the other polymers. A lower absorption coefficient will inhibit exciton formation and hinder device performance. We believe that the reason PBDPTP shows low light absorption is due to bulky substituents causing significant twist to occur along the polymer backbone; the bulky substituents as well as the twisted backbone would decrease the packing density of the polymer chains in the film leading to lower light absorption. PBDPQU, which has the same substituents, also shows low light absorption. Conversely, PBDPBT demonstrates large absorption across the entire visible light spectra. This comparatively high absorption likely contributes to the superior efficiencies exhibited by PBDPBT.

5.3.2.2. Exciton Dissociation

Exciton dissociation at the donor–acceptor interface can be affected by two factors: (i) morphology of the active layer and (ii) the LUMO offset between the two materials. As mentioned above, all four polymers had similar morphologies so morphology is unlikely to be playing a role in the J_{SC} variation observed. As for the LUMO offset, it has been reported that a 0.3-0.4 eV difference is required for exciton dissociation to take place.[97] With the LUMO levels of the polymers lying in the range of −3.34 to −3.63 eV and the LUMO level of $PC_{61}BM$ around −4.2 eV, exciton dissociation is expected to be occurring efficiently in all devices.

5.3.2.3. Charge Transport

Organic field-effect transistors (OFETs) were fabricated and tested in an attempt to determine the hole mobility of each of the four polymers. These are unoptimized devices that were fabricated in an attempt to enable a comparison of mobilities. Unfortunately, we were only able to obtain measurable films for two of the four polymers (PBDPDPP and PBDPTP). The films made from PBDPQU and PBDPBT lacked adequate surface coverage, making accurate mobility measurements impossible. We attempted adding an octydecyltrichlorosilane layer to the substrate before film deposition, but that failed to improve film coverage. We also tried adding small amounts of chloroform (1 and 5 vol %) to the solution before spin coating, but this also created uneven films. Both techniques have previously been shown to sometimes improve polymer film morphology for OFET testing.[98] Successful electrical characterization of PBDPDPP and PBDPTP is shown in Table 5.3.

Table 5.3 Electrical Characterization of BDP-Based Polymers.

Polymer	μ ($cm^2\ V^{-1}\ s^{-1}$)	$I_{on/off}$	V_t (V)
PBDPDPP	2.5×10^{-5} ($\pm\ 0.8 \times 10^{-5}$)	10^4	40
PBDPTP	6.6×10^{-6} ($\pm\ 1.0 \times 10^{-6}$)	10^3	60

The mobility exhibited by PBDPDPP is about four times higher than the mobility measured in PBDPTP. These numbers correlate well with the J_{SC} values obtained from OPVs. Table 5.2 shows that the J_{SC} of PBDPDPP is more than twice that of PBDPTP. This suggests that higher mobilities may be contributing to larger J_{SC} and improved device performance. Additionally, although we failed to obtain measurements from PBDPBT, we would expect this polymer to possess a relatively high mobility – at least as high as PBPDPP. Both PBDPBT and PBPDPP have structural advantages when compared with the other polymers in this study. The planar

conformation of the BT and DPP group and the calculated planar conformation of the polymer backbone all suggest that PBDPBT and PBPDPP should have superior mobility.

When all of the device results are analyzed jointly, it becomes relatively clear why the polymers performed as they did. PBDPBT was the poorest performing polymer; in addition to a relatively low V_{OC}, poor light absorption and low charge mobility combined to yield low PCE. PBDPQU produced devices which were the next worse. This polymer also had a low V_{OC}, but absorbed significantly more light than PBDPBT, which likely lead to its superior J_{SC}. PBDPDPP was the second highest performing material. In this case, high V_{OC} and fill factor were tempered by relatively low J_{SC} and charge mobility to limit efficiency. Finally, PBDPBT produced the best devices; a high V_{OC}, largest light absorption, and a planar polymer structure combined to produce the best polymer in this series.

5.4. Conclusions

We have successfully synthesized four alternating copolymers based on BDP as the common unit. Theoretical calculations and experimental results both support the idea that the benzene cores decrease the electron richness of flanked bithiophene units, leading to a low-lying HOMO energy level. Successfully lowered HOMO energy levels led to high open circuit voltages of BHJ photovoltaic devices fabricated from blends of these polymers with PCBM. The comparison of the absorption of the polymers and charge mobility allowed us to explain the trend observed in the relative device performance. Although the above J_{SC} values are somewhat low, these, and overall device performance, can be dramatically improved by optimizing the processing techniques during device fabrication. Donor:acceptor blend ratios, material concentrations, solvent selection, device thicknesses, and annealing conditions all can influence device

performance and must be taken into consideration when attempting to fabricate high-performance OPVs. Once these variables are fully optimized, we believe that PBDPBT could represent a promising candidate for high-performance, low-bandgap photovoltaics; future studies will focus on the optimization of PBDPBT-related structures and their devices.

6. Future Work

6.1. Observing the Effect of Regular Alignment of Nanowires within the Active Layer on Charge Transport in P3HT Nanowire Films

Another project that could further elucidate the charge transport behavior in the P3HT nanowires discussed in Chapter 3 would be to observe how alignment of the nanowire films affects the hole mobility within the films. Groups have shown that they can successfully align the nanowires within their nanowire films through a combination of substrate abrasion and directional solvent evaporation.[99] They have demonstrated that a nanowire film, which would otherwise lack any degree of directionality, can be processed such that the nanowires become very well aligned, parallel to one another. These nanowire films also demonstrated a 100% increase in mobility once the nanowires were aligned. This type of film morphology might have the potential to almost entirely eliminate nanowire overlapping, which would allow us to probe deeper into how nanowire regioregularity and hole mobility are related. It could also allow us to avoid the poor film quality we observed when we made dilute nanowire films.

6.2. Incorporation of High Regioregular P3HT Nanowires into OPVs

Finally, these high-regioregular P3HT nanowires should be incorporated into the active layer of OPVs. We have shown that these wires have superior charge transport capabilities when compared to lower regioregularity nanowires. However, the main direction of charge transport for these nanowires (which we measured with our OFETs) is parallel to the substrate's surface, along the long-axis of the nanowires. In OPVs, due to the architecture is traditionally used, charge transport is more important in the direction which is perpendicular to the device surface. Determining how much the short circuit current density and overall device efficiency are

affected/improved once high-regioregular P3HT nanowires are included in the active layer of a device would indicate the effectiveness of utilizing these materials in OPV applications.

7. References

1. You, J. B.; Dou, L. T.; Yoshimura, K.; Kato, T.; Ohya, K.; Moriarty, T.; Emery, K.; Chen, C. C.; Gao, J.; Li, G.; Yang, Y., A polymer tandem solar cell with 10.6% power conversion efficiency. *Nature Communications* **2013,** *4*.
2. Barnett, A.; Kirkpatrick, D.; Honsberg, C.; Moore, D.; Wanlass, M.; Emery, K.; Schwartz, R.; Carlson, D.; Bowden, S.; Aiken, D.; Gray, A.; Kurtz, S.; Kazmerski, L.; Steiner, M.; Gray, J.; Davenport, T.; Buelow, R.; Takacs, L.; Shatz, N.; Bortz, J.; Jani, O.; Goossen, K.; Kiamilev, F.; Doolittle, A.; Ferguson, I.; Unger, B.; Schmidt, G.; Christensen, E.; Salzman, D., Very High Efficiency Solar Cell Modules. *Progress in Photovoltaics* **2009,** *17* (1), 75-83.
3. Tipnis, R.; Bernkopf, J.; Jia, S. J.; Krieg, J.; Li, S.; Storch, M.; Laird, D., Large-area organic photovoltaic module-Fabrication and performance. *Solar Energy Materials and Solar Cells* **2009,** *93* (4), 442-446.
4. Dennler, G.; Scharber, M. C.; Brabec, C. J., Polymer-Fullerene Bulk-Heterojunction Solar Cells. *Advanced Materials* **2009,** *21* (13), 1323-1338.
5. Muhlbacher, D. S., M.; Morana, M.; Zhu, Z. G.; Waller, D.; Gaudiana, R.; Brabec, C., High Photovoltaic Performance of a Low-Bandgap Polymer. *Adv. Mater.* **2006,** *18*, 2884-2889.
6. Thompson, B. C.; Kim, Y. G.; McCarley, T. D.; Reynolds, J. R., Soluble narrow band gap and blue propylenedioxythiophene-cyanovinylene polymers as multifunctional materials for photovoltaic and electrochromic applications. *Journal of the American Chemical Society* **2006,** *128* (39), 12714-12725.
7. Wong, W. Y.; Wang, X. Z.; He, Z.; Chan, K. K.; Djurisic, A. B.; Cheung, K. Y.; Yip, C. T.; Ng, A. M. C.; Xi, Y. Y.; Mak, C. S. K.; Chan, W. K., Tuning the absorption, charge transport properties, and solar cell efficiency with the number of thienyl rings in platinum-containing poly(aryleneethynylene)s. *Journal of the American Chemical Society* **2007,** *129* (46), 14372-14380.
8. Blouin, N.; Michaud, A.; Gendron, D.; Wakim, S.; Blair, E.; Neagu-Plesu, R.; Belletete, M.; Durocher, G.; Tao, Y.; Leclerc, M., Toward a rational design of poly(2,7-carbazole) derivatives for solar cells. *Journal of the American Chemical Society* **2008,** *130* (2), 732-742.
9. Chen, C. P.; Chan, S. H.; Chao, T. C.; Ting, C.; Ko, B. T., Low-bandgap poly(thiophene-phenylene-thiophene) derivatives with broaden absorption spectra for use in high-performance bulk-heterojunction polymer solar cells. *Journal of the American Chemical Society* **2008,** *130* (38), 12828-12833.
10. Hou, J. H.; Chen, H. Y.; Zhang, S. Q.; Li, G.; Yang, Y., Synthesis, Characterization, and Photovoltaic Properties of a Low Band Gap Polymer Based on Silole-Containing Polythiophenes and 2,1,3-Benzothiadiazole. *Journal of the American Chemical Society* **2008,** *130* (48), 16144.
11. Wang, E. G.; Wang, L.; Lan, L. F.; Luo, C.; Zhuang, W. L.; Peng, J. B.; Cao, Y., High-performance polymer heterojunction solar cells of a polysilafluorene derivative. *Applied Physics Letters* **2008,** *92* (3), -.
12. Wienk, M. M.; Turbiez, M.; Gilot, J.; Janssen, R. A. J., Narrow-bandgap diketo-pyrrolo-pyrrole polymer solar cells: The effect of processing on the performance. *Advanced Materials* **2008,** *20* (13), 2556.
13. Chen, H. Y.; Hou, J. H.; Zhang, S. Q.; Liang, Y. Y.; Yang, G. W.; Yang, Y.; Yu, L. P.; Wu, Y.; Li, G., Polymer solar cells with enhanced open-circuit voltage and efficiency. *Nature Photonics* **2009,** *3* (11), 649-653.

14. Park, S. H.; Roy, A.; Beaupre, S.; Cho, S.; Coates, N.; Moon, J. S.; Moses, D.; Leclerc, M.; Lee, K.; Heeger, A. J., Bulk heterojunction solar cells with internal quantum efficiency approaching 100%. *Nature Photonics* **2009,** *3* (5), 297.
15. Qin, R. P.; Li, W. W.; Li, C. H.; Du, C.; Veit, C.; Schleiermacher, H. F.; Andersson, M.; Bo, Z. S.; Liu, Z. P.; Inganas, O.; Wuerfel, U.; Zhang, F. L., A Planar Copolymer for High Efficiency Polymer Solar Cells. *Journal of the American Chemical Society* **2009,** *131* (41), 14612.
16. Yuan, M. J.; Rice, A. H.; Luscombe, C. K., Benzo[2,1-b;3,4-b ']dithiophene-Based Low-Bandgap Polymers for Photovoltaic Applications. *Journal of Polymer Science Part a-Polymer Chemistry* **2011,** *49* (3), 701-711.
17. Rice, A. H.; Giridharagopal, R.; Zheng, S. X.; Ohuchi, F. S.; Ginger, D. S.; Luscombe, C. K., Controlling Vertical Morphology within the Active Layer of Organic Photovoltaics Using Poly(3-hexylthiophene) Nanowires and Phenyl-C-61-butyric Acid Methyl Ester. *Acs Nano* **2011,** *5* (4), 3132-3140.
18. Coakley, K. M.; McGehee, M. D., Conjugated polymer photovoltaic cells. *Chemistry of Materials* **2004,** *16* (23), 4533-4542.
19. Blom, P. W. M.; Mihailetchi, V. D.; Koster, L. J. A.; Markov, D. E., Device physics of polymer : fullerene bulk heterojunction solar cells. *Advanced Materials* **2007,** *19* (12), 1551-1566.
20. Thompson, B. C.; Frechet, J. M. J., Organic photovoltaics - Polymer-fullerene composite solar cells. *Angewandte Chemie-International Edition* **2008,** *47* (1), 58-77.
21. Gunes, S.; Neugebauer, H.; Sariciftci, N. S., Conjugated polymer-based organic solar cells. *Chemical Reviews* **2007,** *107* (4), 1324-1338.
22. Giridharagopal, R.; Ginger, D. S., Characterizing Morphology in Bulk Heterojunction Organic Photovoltaic Systems. *Journal of Physical Chemistry Letters* **2010,** *1* (7), 1160-1169.
23. Groves, C.; Reid, O. G.; Ginger, D. S., Heterogeneity in Polymer Solar Cells: Local Morphology and Performance in Organic Photovoltaics Studied with Scanning Probe Microscopy. *Accounts of Chemical Research* **2010,** *43* (5), 612-620.
24. Tang, C. W., 2-Layer Organic Photovoltaic Cell. *Applied Physics Letters* **1986,** *48* (2), 183-185.
25. Yu, G.; Zhang, C.; Heeger, A. J., Dual-Function Semiconducting Polymer Devices - Light-Emitting and Photodetecting Diodes. *Applied Physics Letters* **1994,** *64* (12), 1540-1542.
26. Sariciftci, N. S.; Braun, D.; Zhang, C.; Srdanov, V. I.; Heeger, A. J.; Stucky, G.; Wudl, F., Semiconducting Polymer-Buckminsterfullerene Heterojunctions - Diodes, Photodiodes, and Photovoltaic Cells. *Applied Physics Letters* **1993,** *62* (6), 585-587.
27. Yang, X. N.; Loos, J.; Veenstra, S. C.; Verhees, W. J. H.; Wienk, M. M.; Kroon, J. M.; Michels, M. A. J.; Janssen, R. A. J., Nanoscale morphology of high-performance polymer solar cells. *Nano Letters* **2005,** *5* (4), 579-583.
28. Swinnen, A.; Haeldermans, I.; Vanlaeke, P.; D'Haen, J.; Poortmans, J.; D'Olieslaeger, M.; Manca, J. V., Dual crystallization behaviour of polythiophene/fullerene blends. *European Physical Journal-Applied Physics* **2006,** *36* (3), 251-256.
29. van Bavel, S. S.; Sourty, E.; de With, G.; Loos, J., Three-Dimensional Nanoscale Organization of Bulk Heterojunction Polymer Solar Cells. *Nano Letters* **2009,** *9* (2), 507-513.
30. Zhokhavets, U.; Erb, T.; Hoppe, H.; Gobsch, G.; Sariciftci, N. S., Effect of annealing of poly(3-hexylthiophene)/fullerene bulk heterojunction composites on structural and optical properties. *Thin Solid Films* **2006,** *496* (2), 679-682.

31. Samitsu, S.; Shimomura, T.; Heike, S.; Hashizume, T.; Ito, K., Effective Production of Poly(3-alkylthiophene) Nanofibers by means of Whisker Method using Anisole Solvent: Structural, Optical, and Electrical Properties. *Macromolecules* **2008,** *41* (21), 8000-8010.
32. Kim, D. H.; Park, Y. D.; Jang, Y.; Kim, S.; Cho, K., Solvent vapor-induced nanowire formation in poly(3-hexylthiophene) thin films. *Macromolecular Rapid Communications* **2005,** *26* (10), 834-839.
33. Campbell, A. J.; Bradley, D. D. C.; Antoniadis, H., Dispersive electron transport in an electroluminescent polyfluorene copolymer measured by the current integration time-of-flight method. *Applied Physics Letters* **2001,** *79* (14), 2133-2135.
34. Cheng, Y. J.; Yang, S. H.; Hsu, C. S., Synthesis of Conjugated Polymers for Organic Solar Cell Applications. *Chemical Reviews* **2009,** *109* (11), 5868-5923.
35. Nam, S.; Lee, S.; Lee, I.; Shin, M.; Kim, H.; Kim, Y., Nanomorphology-driven two-stage hole mobility in blend films of regioregular and regiorandom polythiophenes. *Nanoscale* **2011,** *3* (10), 4261-4269.
36. Zhang, F. L.; Jespersen, K. G.; Bjorstrom, C.; Svensson, M.; Andersson, M. R.; Sundstrom, V.; Magnusson, K.; Moons, E.; Yartsev, A.; Inganas, O., Influence of solvent mixing on the morphology and performance of solar cells based on polyfluorene copolymer/fullerene blends. *Advanced Functional Materials* **2006,** *16* (5), 667-674.
37. Andersson, L. M.; Zhang, F. L.; Inganas, O., Stoichiometry, mobility, and performance in bulk heterojunction solar cells. *Applied Physics Letters* **2007,** *91* (7).
38. Gadisa, A.; Mammo, W.; Andersson, L. M.; Admassie, S.; Zhang, F.; Andersson, M. R.; Inganas, O., A new donor-acceptor-donor polyfluorene copolymer with balanced electron and hole mobility. *Advanced Functional Materials* **2007,** *17* (18), 3836-3842.
39. Huang, Y. C.; Liao, Y. C.; Li, S. S.; Wu, M. C.; Chen, C. W.; Su, W. F., Study of the effect of annealing process on the performance of P3HT/PCBM photovoltaic devices using scanning-probe microscopy. *Solar Energy Materials and Solar Cells* **2009,** *93* (6-7), 888-892.
40. Campoy-Quiles, M.; Ferenczi, T.; Agostinelli, T.; Etchegoin, P. G.; Kim, Y.; Anthopoulos, T. D.; Stavrinou, P. N.; Bradley, D. D. C.; Nelson, J., Morphology evolution via self-organization and lateral and vertical diffusion in polymer: fullerene solar cell blends. *Nature Materials* **2008,** *7* (2), 158-164.
41. Jo, J.; Na, S. I.; Kim, S. S.; Lee, T. W.; Chung, Y.; Kang, S. J.; Vak, D.; Kim, D. Y., Three-Dimensional Bulk Heterojunction Morphology for Achieving High Internal Quantum Efficiency in Polymer Solar Cells. *Advanced Functional Materials* **2009,** *19* (15), 2398-2406.
42. Germack, D. S.; Chan, C. K.; Hamadani, B. H.; Richter, L. J.; Fischer, D. A.; Gundlach, D. J.; DeLongchamp, D. M., Substrate-dependent interface composition and charge transport in films for organic photovoltaics. *Applied Physics Letters* **2009,** *94* (23).
43. Yu, B. Y.; Lin, W. C.; Wang, W. B.; Iida, S.; Chen, S. Z.; Liu, C. Y.; Kuo, C. H.; Lee, S. H.; Kao, W. L.; Yen, G. J.; You, Y. W.; Liu, C. P.; Jou, J. H.; Shyue, J. J., Effect of Fabrication Parameters on Three-Dimensional Nanostructures of Bulk Heterojunctions Imaged by High-Resolution Scanning ToF-SIMS. *Acs Nano* **2010,** *4* (2), 833-840.
44. Parnell, A. J.; Dunbar, A. D. F.; Pearson, A. J.; Staniec, P. A.; Dennison, A. J. C.; Hamamatsu, H.; Skoda, M. W. A.; Lidzey, D. G.; Jones, R. A. L., Depletion of PCBM at the Cathode Interface in P3HT/PCBM Thin Films as Quantified via Neutron Reflectivity Measurements. *Advanced Materials* **2010,** *22* (22), 2444.
45. Merlo, J. A.; Frisbie, C. D., Field effect transport and trapping in regioregular polythiophene nanofibers. *Journal of Physical Chemistry B* **2004,** *108* (50), 19169-19179.

46. Nagamatsu, S.; Takashima, W.; Kaneto, K.; Yoshida, Y.; Tanigaki, N.; Yase, K., Backbone arrangement in "friction-transferred" regioregular poly(3-alkylthiophene)s. *Macromolecules* **2003,** *36* (14), 5252-5257.
47. Yonemura, H.; Yuno, K.; Yamamoto, Y.; Yamada, S.; Fujiwara, Y.; Tanimoto, Y., Orientation of nanowires consisting of poly(3-hexylthiophene) using strong magnetic field. *Synthetic Metals* **2009,** *159* (9-10), 955-960.
48. Qiao, R.; Roberts, A. P.; Mount, A. S.; Klaine, S. J.; Ke, P. C., Translocation of C-60 and its derivatives across a lipid bilayer. *Nano Letters* **2007,** *7* (3), 614-619.
49. Coffey, D. C.; Reid, O. G.; Rodovsky, D. B.; Bartholomew, G. P.; Ginger, D. S., Mapping local photocurrents in polymer/fullerene solar cells with photoconductive atomic force microscopy. *Nano Letters* **2007,** *7* (3), 738-744.
50. Hamadani, B. H.; Jung, S. Y.; Haney, P. M.; Richter, L. J.; Zhitenev, N. B., Origin of Nanoscale Variations in Photoresponse of an Organic Solar Cell. *Nano Letters* **2010,** *10* (5), 1611-1617.
51. Pingree, L. S. C.; Reid, O. G.; Ginger, D. S., Imaging the Evolution of Nanoscale Photocurrent Collection and Transport Networks during Annealing of Polythiophene/Fullerene Solar Cells. *Nano Letters* **2009,** *9* (8), 2946-2952.
52. Xin, H.; Reid, O. G.; Ren, G. Q.; Kim, F. S.; Ginger, D. S.; Jenekhe, S. A., Polymer Nanowire/Fullerene Bulk Heterojunction Solar Cells: How Nanostructure Determines Photovoltaic Properties. *Acs Nano* **2010,** *4* (4), 1861-1872.
53. Reid, O. G.; Xin, H.; Jenekhe, S. A.; Ginger, D. S., Nanostructure determines the intensity dependence of open circuit voltage in plastic solar cells. *Journal of Applied Physics* **2010**.
54. Wagner, C. D.; Riggs, W. M.; Davis, L. E.; Moulder, J. F.; Muilenberg, G. E., (2nd Ed.), Handbook of XPS, Physical Electronics. Eden Prairie, MN, 1979.
55. Wenzel, R. N., Resistance of solid surfaces to wetting by water. *Industrial and Engineering Chemistry* **1936,** *28*, 988-994.
56. Bronstein, H. A.; Luscombe, C. K., Externally Initiated Regioregular P3HT with Controlled Molecular Weight and Narrow Polydispersity. *Journal of the American Chemical Society* **2009,** *131* (36), 12894.
57. Mauer, R.; Kastler, M.; Laquai, F., The Impact of Polymer Regioregularity on Charge Transport and Efficiency of P3HT:PCBM Photovoltaic Devices. *Advanced Functional Materials* **2010,** *20* (13), 2085-2092.
58. Sirringhaus, H.; Brown, P. J.; Friend, R. H.; Nielsen, M. M.; Bechgaard, K.; Langeveld-Voss, B. M. W.; Spiering, A. J. H.; Janssen, R. A. J.; Meijer, E. W.; Herwig, P.; de Leeuw, D. M., Two-dimensional charge transport in self-organized, high-mobility conjugated polymers. *Nature* **1999,** *401* (6754), 685-688.
59. Snyder, C. R.; Henry, J. S.; DeLongchamp, D. M., Effect of Regioregularity on the Semicrystalline Structure of Poly(3-hexylthiophene). *Macromolecules* **2011,** *44* (18), 7088-7091.
60. Choi, D.; Jin, S.; Lee, Y.; Kim, S. H.; Chung, D. S.; Hong, K.; Yang, C.; Jung, J.; Kim, J. K.; Ree, M.; Park, C. E., Direct Observation of Interfacial Morphology in Poly(3-hexylthiophene) Transistors: Relationship between Grain Boundary and Field-Effect Mobility. *Acs Applied Materials & Interfaces* **2010,** *2* (1), 48-53.
61. Bertho, S.; Janssen, G.; Cleij, T. J.; Conings, B.; Moons, W.; Gadisa, A.; D'Haen, J.; Goovaerts, E.; Lutsen, L.; Manca, J.; Vanderzande, D., Effect of temperature on the

morphological and photovoltaic stability of bulk heterojunction polymer: fullerene solar cells. *Solar Energy Materials and Solar Cells* **2008,** *92* (7), 753-760.
62. Brabec, C. J.; Sariciftci, N. S.; Hummelen, J. C., Plastic solar cells. *Advanced Functional Materials* **2001,** *11* (1), 15-26.
63. Hoppe, H.; Sariciftci, N. S., Organic solar cells: An overview. *Journal of Materials Research* **2004,** *19* (7), 1924-1945.
64. Moule, A. J.; Meerholz, K., Controlling morphology in polymer-fullerene mixtures. *Advanced Materials* **2008,** *20* (2), 240.
65. Ma, W. L.; Yang, C. Y.; Gong, X.; Lee, K.; Heeger, A. J., Thermally stable, efficient polymer solar cells with nanoscale control of the interpenetrating network morphology. *Advanced Functional Materials* **2005,** *15* (10), 1617-1622.
66. Bull, T. A.; Pingree, L. S. C.; Jenekhe, S. A.; Ginger, D. S.; Luscombe, C. K., The Role of Mesoscopic PCBM Crystallites in Solvent Vapor Annealed Copolymer Solar Cells. *Acs Nano* **2009,** *3* (3), 627-636.
67. Lim, J. A.; Liu, F.; Ferdous, S.; Muthukumar, M.; Briseno, A. L., Polymer semiconductor crystals. *Materials Today* **2010,** *13* (5), 14-24.
68. Muller, C.; Ferenczi, T. A. M.; Campoy-Quiles, M.; Frost, J. M.; Bradley, D. D. C.; Smith, P.; Stingelin-Stutzmann, N.; Nelson, J., Binary organic photovoltaic blends: A simple rationale for optimum compositions. *Advanced Materials* **2008,** *20* (18), 3510.
69. Zhao, J.; Swinnen, A.; Van Assche, G.; Manca, J.; Vanderzande, D.; Van Mele, B., Phase Diagram of P3HT/PCBM Blends and Its Implication for the Stability of Morphology. *Journal of Physical Chemistry B* **2009,** *113* (6), 1587-1591.
70. Chen, D. A.; Nakahara, A.; Wei, D. G.; Nordlund, D.; Russell, T. P., P3HT/PCBM Bulk Heterojunction Organic Photovoltaics: Correlating Efficiency and Morphology. *Nano Letters* **2011,** *11* (2), 561-567.
71. Treat, N. D.; Brady, M. A.; Smith, G.; Toney, M. F.; Kramer, E. J.; Hawker, C. J.; Chabinyc, M. L., Interdiffusion of PCBM and P3HT Reveals Miscibility in a Photovoltaically Active Blend. *Advanced Energy Materials* **2011,** *1* (1), 82-89.
72. Voroshazi, E.; Verreet, B.; Aernouts, T.; Heremans, P., Long-term operational lifetime and degradation analysis of P3HT: PCBM photovoltaic cells. *Solar Energy Materials and Solar Cells* **2011,** *95* (5), 1303-1307.
73. Sivula, K.; Ball, Z. T.; Watanabe, N.; Frechet, J. M. J., Amphiphilic diblock copolymer compatibilizers and their effect on the morphology and performance of polythiophene: Fullerene solar cells. *Advanced Materials* **2006,** *18* (2), 206.
74. Yang, C.; Lee, J. K.; Heeger, A. J.; Wudl, F., Well-defined donor-acceptor rod-coil diblock copolymers based on P3HT containing C-60: the morphology and role as a surfactant in bulk-heterojunction solar cells. *Journal of Materials Chemistry* **2009,** *19* (30), 5416-5423.
75. Tsai, J. H.; Lai, Y. C.; Higashihara, T.; Lin, C. J.; Ueda, M.; Chen, W. C., Enhancement of P3HT/PCBM Photovoltaic Efficiency Using the Surfactant of Triblock Copolymer Containing Poly(3-hexylthiophene) and Poly(4-vinyltriphenylamine) Segments. *Macromolecules* **2010,** *43* (14), 6085-6091.
76. Li, C. Z.; Chien, S. C.; Yip, H. L.; Chueh, C. C.; Chen, F. C.; Matsuo, Y.; Nakamura, E.; Jen, A. K. Y., Facile synthesis of a 56 pi-electron 1,2-dihydromethano-[60]PCBM and its application for thermally stable polymer solar cells. *Chemical Communications* **2011,** *47* (36), 10082-10084.

77. Zhang, Y.; Hau, S. K.; Yip, H. L.; Sun, Y.; Acton, O.; Jen, A. K. Y., Efficient Polymer Solar Cells Based on the Copolymers of Benzodithiophene and Thienopyrroledione. *Chemistry of Materials* **2010,** *22* (9), 2696-2698.
78. Jamieson, F. C.; Domingo, E. B.; McCarthy-Ward, T.; Heeney, M.; Stingelin, N.; Durrant, J. R., Fullerene crystallisation as a key driver of charge separation in polymer/fullerene bulk heterojunction solar cells. *Chemical Science* **2012,** *3* (2), 485-492.
79. Li, L. G.; Tang, H. W.; Wu, H. X.; Lu, G. H.; Yang, X. N., Effects of fullerene solubility on the crystallization of poly(3-hexylthiophene) and performance of photovoltaic devices. *Organic Electronics* **2009,** *10* (7), 1334-1344.
80. Clark, J.; Chang, J. F.; Spano, F. C.; Friend, R. H.; Silva, C., Determining exciton bandwidth and film microstructure in polythiophene films using linear absorption spectroscopy. *Applied Physics Letters* **2009,** *94* (16).
81. Wu, W. R.; Jeng, U. S.; Su, C. J.; Wei, K. H.; Su, M. S.; Chiu, M. Y.; Chen, C. Y.; Su, W. B.; Su, C. H.; Su, A. C., Competition between Fullerene Aggregation and Poly(3-hexylthiophene) Crystallization upon Annealing of Bulk Heterojunction Solar Cells. *Acs Nano* **2011,** *5* (8), 6233-6243.
82. Kwiatkowski, J. J.; Frost, J. M.; Nelson, J., The Effect of Morphology on Electron Field-Effect Mobility in Disordered C60 Thin Films. *Nano Letters* **2009,** *9* (3), 1085-1090.
83. von Hauff, E.; Dyakonov, V.; Parisi, R., Study of field effect mobility in PCBM films and P3HT : PCBM blends. *Solar Energy Materials and Solar Cells* **2005,** *87* (1-4), 149-156.
84. Kim, Y.; Cook, S.; Tuladhar, S. M.; Choulis, S. A.; Nelson, J.; Durrant, J. R.; Bradley, D. D. C.; Giles, M.; Mcculloch, I.; Ha, C. S.; Ree, M., A strong regioregularity effect in self-organizing conjugated polymer films and high-efficiency polythiophene: fullerene solar cells. *Nature Materials* **2006,** *5* (3), 197-203.
85. Shrotriya, V.; Li, G.; Yao, Y.; Moriarty, T.; Emery, K.; Yang, Y., Accurate measurement and characterization of organic solar cells. *Advanced Functional Materials* **2006,** *16* (15), 2016-2023.
86. Scharber, M. C.; Wuhlbacher, D.; Koppe, M.; Denk, P.; Waldauf, C.; Heeger, A. J.; Brabec, C. L., Design rules for donors in bulk-heterojunction solar cells - Towards 10 % energy-conversion efficiency. *Advanced Materials* **2006,** *18* (6), 789.
87. Liang, Y. Y.; Xu, Z.; Xia, J. B.; Tsai, S. T.; Wu, Y.; Li, G.; Ray, C.; Yu, L. P., For the Bright Future-Bulk Heterojunction Polymer Solar Cells with Power Conversion Efficiency of 7.4%. *Advanced Materials* **2010,** *22* (20), E135.
88. Piliego, C.; Holcombe, T. W.; Douglas, J. D.; Woo, C. H.; Beaujuge, P. M.; Frechet, J. M. J., Synthetic Control of Structural Order in N-Alkylthieno[3,4-c]pyrrole-4,6-dione-Based Polymers for Efficient Solar Cells. *Journal of the American Chemical Society* **2010,** *132* (22), 7595.
89. Xiao, S. Q.; Zhou, H. X.; You, W., Conjugated polymers of fused bithiophenes with enhanced pi-electron delocalization for photovoltaic applications. *Macromolecules* **2008,** *41* (15), 5688-5696.
90. Zhou, H. X.; Yang, L. Q.; Stoneking, S.; You, W., A Weak Donor-Strong Acceptor Strategy to Design Ideal Polymers for Organic Solar Cells. *Acs Applied Materials & Interfaces* **2010,** *2* (5), 1377-1383.
91. Rieger, R.; Beckmann, D.; Pisula, W.; Steffen, W.; Kastler, M.; Mullen, K., Rational Optimization of Benzo[2,1-b;3,4-b ']dithilophene-Containing Polymers for Organic Field-Effect Transistors. *Advanced Materials* **2010,** *22* (1), 83.

92. Chen, C. H.; Hsieh, C. H.; Dubosc, M.; Cheng, Y. J.; Su, C. S., Synthesis and Characterization of Bridged Bithiophene-Based Conjugated Polymers for Photovoltaic Applications: Acceptor Strength and Ternary Blends. *Macromolecules* **2010,** *43* (2), 697-708.
93. Kim, M. S.; Kim, B. G.; Kim, J., Effective Variables To Control the Fill Factor of Organic Photovoltaic Cells. *Acs Applied Materials & Interfaces* **2009,** *1* (6), 1264-1269.
94. Mihailetchi, V. D.; Blom, P. W. M.; Hummelen, J. C.; Rispens, M. T., Cathode dependence of the open-circuit voltage of polymer : fullerene bulk heterojunction solar cells. *Journal of Applied Physics* **2003,** *94* (10), 6849-6854.
95. Wienk, M. M.; Kroon, J. M.; Verhees, W. J. H.; Knol, J.; Hummelen, J. C.; van Hal, P. A.; Janssen, R. A. J., Efficient methano[70]fullerene/MDMO-PPV bulk heterojunction photovoltaic cells. *Angewandte Chemie-International Edition* **2003,** *42* (29), 3371-3375.
96. Zheng, Q. D.; Jung, B. J.; Sun, J.; Katz, H. E., Ladder-Type Oligo-p-phenylene-Containing Copolymers with High Open-Circuit Voltages and Ambient Photovoltaic Activity. *Journal of the American Chemical Society* **2010,** *132* (15), 5394-5404.
97. Brabec, C. J.; Winder, C.; Sariciftci, N. S.; Hummelen, J. C.; Dhanabalan, A.; van Hal, P. A.; Janssen, R. A. J., A low-bandgap semiconducting polymer for photovoltaic devices and infrared emitting diodes. *Advanced Functional Materials* **2002,** *12* (10), 709-712.
98. Lim, S. C.; Kim, S. H.; Lee, J. H.; Kim, M. K.; Kim, D. J.; Zyung, T., Surface-treatment effects on organic thin-film transistors. *Synthetic Metals* **2005,** *148* (1), 75-79.
99. Tseng, H. R.; Ying, L.; Hsu, B. B. Y.; Perez, L. A.; Takacs, C. J.; Bazan, G. C.; Heeger, A. J., High Mobility Field Effect Transistors Based on Macroscopically Oriented Regioregular Copolymers. *Nano Letters* **2012,** *12* (12), 6353-6357.
100. Ezquerra, T. A., *Applications of synchrotron light to scattering and diffraction in materials and life sciences*. Springer: Berlin, 2009; p xvi, 318 p.
101. Chiu, M. Y.; Jeng, U. S.; Su, M. S.; Wei, K. H., Morphologies of Self-Organizing Regioregular Conjugated Polymer/Fullerene Aggregates in Thin Film Solar Cells. *Macromolecules* **2010,** *43* (1), 428-432.
102. Busch, P.; Posselt, D.; Smilgies, D. M.; Rauscher, M.; Papadakis, C. M., Inner structure of thin films of lamellar poly(styrene-b-butadiene) diblock copolymers as revealed by grazing-incidence small-angle scattering. *Macromolecules* **2007,** *40* (3), 630-640.

8. Appendix

8.1. Controlling Vertical Morphology Within the Active Layer of Organic Photovoltaics Using Poly(3-hexylthiophene) Nanowires and Phenyl-C_{61}-butyric Acid Methyl Ester

8.1.1. Experimental

8.1.1.1. Device Fabrication

The substrates used in this study were ITO-coated glass (15 Ω/m^2, supplied by Colorado Concept Coatings) cut into 1.5 × 1.5 cm squares. Substrates were cleaned *via* a series of ultrasonic baths in a mild detergent, deionized water, acetone, and isopropyl alcohol. The substrates were removed from the last bath and dried using N_2. They were then treated with air plasma for 10 min under vacuum (200 mTorr).

Once clean, substrates were coated with filtered PEDOT:PSS (Clevios PVP Al 4083). The PEDOT:PSS was spin-coated, in air, on top of the ITO surface from solution to obtain a layer roughly 40 nm thick. These films were annealed in air at 140 °C for 10 min. They were then stored under argon until the active layer was prepared.

Active layer preparation began by making the solvent, which was comprised of 80 vol % anisole combined with 20 vol % chloroform. P3HT (Rieke Metal, Sepiolid P100) and PCBM (American Dye Source Inc. ADS61BFB) were added to the solvent, and the solution was stirred in the dark inside the glovebox at 500 rpm for 3 h at 70 °C. The ratio between P3HT:PCBM was maintained at 1:0.8 (by weight). After 3 h, the solution was removed from heat and stored in the dark overnight (~18 h) to allow the nanowires to self-assemble in solution. The solution was then deposited on top of the PEDOT:PSS layer. At this point, the appropriate pre-spin drying time

was allowed. Deposition was completed by spin-coating at 1000 rpm for 60 s. Finally, electrodes were deposited on top of the active layer *via* thermal evaporation. A 1 nm layer of LiF followed by a 100 nm layer of Al were evaporated under vacuum (2×10^{-6} Torr) to form the electrodes.

8.1.1.2. Device Characterization

The *J*−*V* characteristics of the resultant devices were immediately tested after processing was completed. This was done in air using a Keithley 2400 source measurement unit and an Oriel Xenon lamp (450 W). An AM 1.5 filter was used as the light source. Calibration of the light intensity was completed using a standard silicon solar cell with a KG5 filter. A light intensity of 100 $mW \cdot cm^{-2}$ was used throughout this study. The series resistance and parallel resistance were calculated from the inverse of the slope of the *J*−*V* curve at 1 and 0 V, respectively. At least 24 devices were tested and averaged during *J*−*V* characterization. It should be noted that the objective of this work is to demonstrate trends in the data between different processes, not to produce champion data. For this reason, the spectral mismatch factor was not included in the measurements.

XPS spectra were generated using a PHI Versaprobe system with an Al Kα X-ray source and a 1 μm beam size. Measurements were taken while the sample was under ultrahigh vacuum (10^{-10} Torr).

8.1.1.3. Imaging

Tapping mode AFM images were taken on a Veeco multimode AFM with a Nanoscope III controller in tapping mode. The AFM tips used for this study were purchased from Veeco: model

RTESP ($f \approx 300$ kHz, $k \approx 40$ N/m) phosphorus doped-Si tips. Active layer thicknesses were measured using the scratch test.

Conductive and photoconductive AFM images were acquired using an atomic force microscope (MFP-3D-BIO, Asylum Research) mounted on an inverted optical microscope (Nikon Eclipse TE2000-U). Images were acquired using gold-coated silicon cantilevers (CONTE-GB, $k \approx 0.2$ N/m, Budget Sensors). Because of the soft nature of these samples, the samples were imaged in attractive contact mode rather than the typical repulsive-regime contact mode. All samples were mounted in a sealed fluid cell inside an oxygen/water-free glovebox and imaged under constant nitrogen flow to protect against photo-oxidation. For photoconductive AFM, a 532 nm laser (Crystal Laser GCL-005 L, 5 mW) was focused at the top of the sample, attenuated with neutral density filters, and coaligned with the apex of the tip. Therefore, the images acquired represent the short-circuit photocurrent. The laser intensity was kept constant between images using an adjustable neutral density filter and sampled at approximately 10^8 W/m^2. Currents observed here are lower than observed in previous polythiophene nanowire work;[52] we tentatively attribute this to the lack of tip penetration due to attractive imaging, therefore limiting the contact area. We did not notice any significant change in photocurrent with intensity; however, because photocurrents seem to be lower in the attractive contact method, we have a limited range of possible laser intensities. Attractive-mode pcAFM is highly sensitive to imaging conditions and feedback settings, and instability in the imaging parameters can cause the tip to drift out of contact with the surface. This effect is amplified if imaging occurs within the first 30 min of approaching, possibly due to piezo hysteresis.

8.1.2. Additional Figures

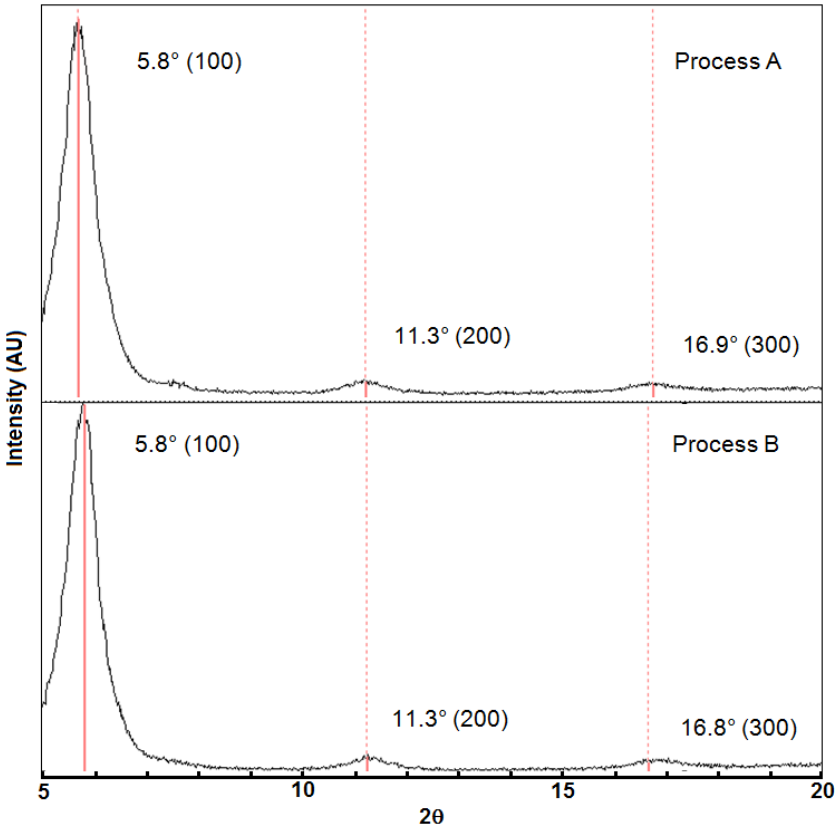

Figure 8.1 XRD spectra for films made with processes A and B.

Each spectra displays a fairly sharp peak around 5.8° 2θ ((100), representing intermolecular spacing) corresponding to a d-spacing of 1.5 nm. This main peak is followed by two significantly less intense, broader peaks around 11.3° 2θ (200) and 16.8° 2θ (300). The π- π stacking peak (010), which should be located around 23° 2θ, was not observed. It should be noted that the comparison spectra taken from the literature are from P3HT only samples; the fact that our spectra are similar to the literature suggests that PCBM is not likely changing the d-spacing within the nanowires. While we cannot say definitively that PCBM is not penetrating the nanowire structure to some degree, it is not likely that this is happening with any regularity. Additionally, because the spectra for processes A and B are virtually identical, there is no evidence of a physical difference between the microstructure of these two nanowire types.

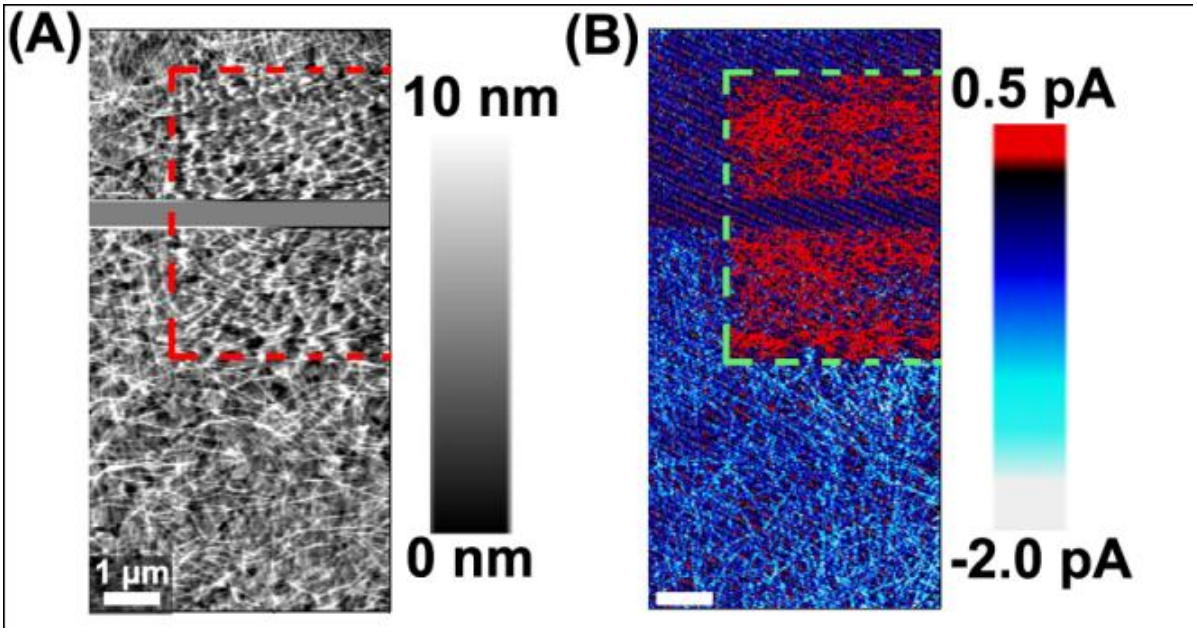

Figure 8.2 Image showing the (A) topography and (B) short-circuit photocurrent for both typical repulsive regime pcAFM and attractive regime pcAFM on the same area of the film.

The area outlined in red in (A) and green in (B) was imaged first in repulsive regime. The photocurrent is almost entirely positive, which is consistent with the tip penetrating the top PCBM layer and imaging the underlying P3HT nanowire region. After imaging this region, the scan area was expanded and carefully imaged in attractive mode pcAFM. The photocurrent is almost all negative in the areas that were not previously damaged by the repulsive regime pcAFM. Careful inspection of (A) reveals topographic damage within the dashed box region as well. The missing lines of data are due to the sensitive feedback conditions that can cause the tip to drift out of contact with the surface and thus not record a height or current. This set of data therefore show: why repulsive regime pcAFM is damaging and misleading for very soft samples, why attractive regime pcAFM poses some feedback-related experimental difficulties, and why we believe that there is a top layer of PCBM in these films.

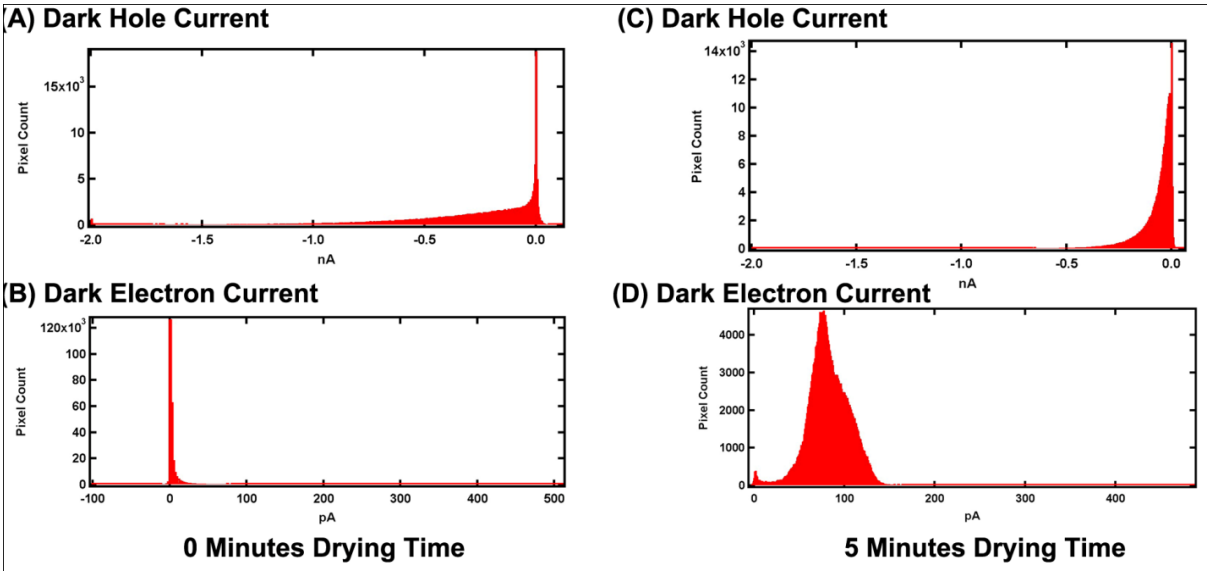

Figure 8.3 Histogram data of the current distributions, in this case for 0 minutes drying time (A-B) and 5 minutes drying time (C-D) for (A,C) dark hole current (B,D) dark electron current.

As noted in the main manuscript, the dark hole current decreases with increased drying time, as evidenced by a smaller distribution closer to 0 nA in 17D versus 17A. This is consistent with less P3HT material on the top surface. Similarly, the dark electron current increases significantly with increased drying time, as evidenced by the significant shift right and the broadened histogram data from 17B to 17D. That the peak current shifts away from 0 pA indicates a strong presence of PCBM, with the distribution of current indicative of the relative connectivity of acceptor pathways over the film.

8.2. The Effect of Regioregularity on Charge Transport and Coherent Domain Size in P3HT Nanowires

8.2.1. Experimental

8.2.1.1. Materials and Synthesis

To a dried schlenk flask was added LiCl (127 mg, 3 mmol), flask was dried by heating under vacuum, 2-Bromo-3-hexyl-5-iodothiophene (373 mg, 1 mmol) was added and the flask was pumped and purged with nitrogen. Dry THF (20 mL) was added via cannula and the reaction was cooled to 0 °C with stirring. 2 M isopropylmagnesiumchloride (0.5 mL, 1 mmol) was added dropwise over 5 min and stirring continued for 1 h. To a second dry schlenk flask was added bromo(*o*-tolyl)bis(triphenylphosphine)nickel(II) (6.3 mg (0.0084 mmol) and 1,3-bis(diphenylphosphino)propane (10.4 mg, 0.0252 mmol). Dry THF (20 mL) was added via cannula and the nickel catalyst complex was allowed to stir for 2 hours at room temperature. The prepared grignardized thiophene monomer solution was quickly transferred via cannula to the catalyst solution at 0 °C. The reaction was allowed to warm to room temperature and stirred for 2 hours. 5 M HCl (1 mL) was added to quench the polymerization. The reaction mixture was stirred for 15 minutes and poured to methanol. The polymer material was isolated by filtration and washed with methanol. The polymer was purified by soxhlet extraction with methanol followed by acetone followed by a final extraction with chloroform. The solution was concentrated and precipitated into methanol and filtered to yield the purified P3HT polymer product (~70 mg, ~40% yield).

8.2.1.2. Fabrication and Characterization of Nanowire Films

P3HT nanowire solution preparation began by first preparing the solvent, which is comprised of 80 vol % anisole combined with 20 vol % chloroform. P3HT was added to this solvent (at varying concentrations) and the solution was stirred overnight inside the glove box at 70 °C. Once stirring was completed and the P3HT was completely dissolved, the solution was removed from heat and left untouched for three days to allow the nanowires to self-assemble in solution.

During this period, solutions changed from a bright orange color to dark purple. Once self-assembly was complete, the nanowire solutions were deposited on top of the clean silicon substrates *via* spin-coating at 1000 rpm for 60 s. These substrates were cleaned by sequential ultrasonication baths in acetone, methanol, and isopropyl alcohol (15 min each), followed by an air plasma treatment under vacuum (200 mTorr) for 5 min. Finished films were characterized with AFM to examine nanowire size and film quality. Tapping mode AFM images were taken on a Veeco multimode AFM with a Nanoscope III controller. The AFM tips used for this study were purchased from Veeco: model RTESP ($f \approx 300$ kHz, $k \approx 40$ N/m) phosphorus doped-Si tips.

For the samples prepared for characterization by XRD, film preparation was a little different. Once the nanowire self-assembly was completed, solutions were taken and centrifuged at 2500 RPM for 30 min, causing the nanowires to separate from the solution. Nanowires were collected and dispersed in isopropyl alcohol. This new solution was drop cast onto clean, glass substrates to form a thick, dense, nanowire film. XRD patterns were obtained on Bruker AXS D8 Focus diffractometer using an accelerating voltage of 40 kV and a Cu Kα source.

8.2.1.3. Fabrication and Characterization of OFETs

Top-contact:bottom-gate field-effect transistors were fabricated on silicon substrates. Heavily doped *p*-type silicon <100> substrates from Montco Silicon Technologies Inc. with a 300 nm (±5 nm) thermal oxide layer served both as a common gate with dielectric layer and as a substrate. P3HT nanowire solutions were spin-coated (1000 rpm for 60 s) onto clean substrates (same cleaning process as described above) to make thin films. Gold source and drain electrodes (~50 nm thick) were deposited on top of the polymer films *via* thermal evaporation at 1.0 Å/s through a shadow mask from a resistively heated Mo boat under high vacuum (5.0×10^{-7} Torr). Device

fabrication and characterization was performed under nitrogen. The saturated charge carrier mobility for each polymer film was calculated using the saturation current equation: $I_{ds} = (\mu W C_0/2L)(V_g - V_t)$. A linear fit was applied to the saturation region of the $I_{ds}^{1/2}$ versus V_g curve of sample in order to calculate the charge mobility of the materials. At least 12 devices were tested for each processing condition. The average values are reported above with error bars representing the standard deviation.

8.2.2. Additional Figures

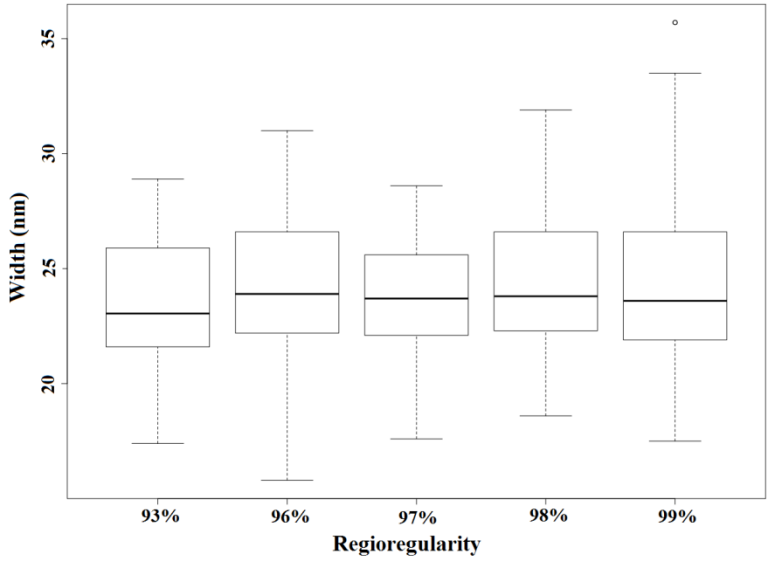

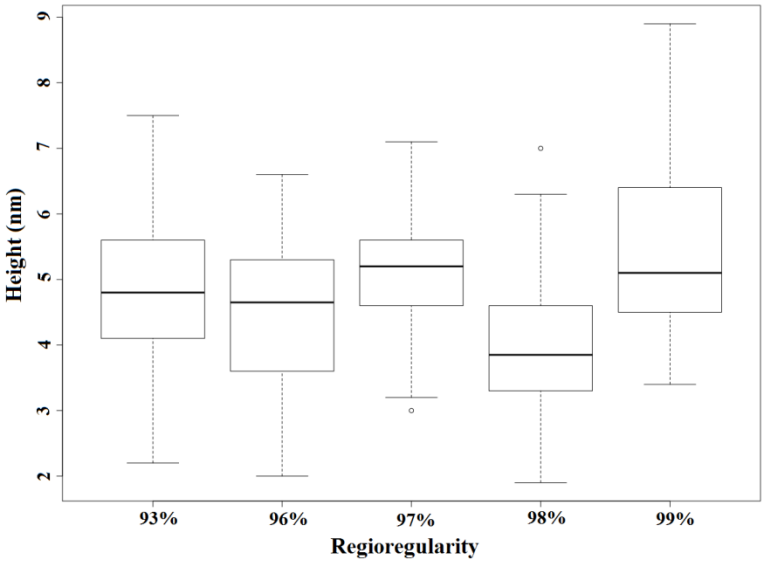

Figure 8.4 Boxplots showing the effect of P3HT regioregularity on A) nanowire width and B) nanowire height. At least 100 individual nanowires were measured to generate these values.

8.3. Modification of PCBM Crystallization via Incorporation of C_{60} in Polymer:Fullerene Solar Cells

8.3.1. Experimental

8.3.1.1. Materials

Poly(3-hexylthiophene) (Sepiloid P100) used in this study was purchased from Rieke Metals (Lincoln, NE). [6,6]-Phenyl C_{61} butyric acid methyl ester (PCBM) was purchased from SES Research (Houston, TX) for the open films studies and American Dye Source for OPVs (Quebec, Canada). PEDOT:PSS (PVP AL 4083) was supplied by Clevios (Germany). The ITO used for solar cells was supplied by Colorado Concept Coatings (15 Ω m^{-2}) and was cut into 1.5 cm × 1.5 cm squares. Chlorobenzene, anhydrous, 99.8% was supplied by Sigma Aldrich (St. Louis, MO).

8.3.1.2. Fabrication and Characterization of Films

Two active layer solutions were prepared with identical P3HT:fullerene weight ratios. The first consisted of P3HT (18 mg) and PCBM (12 mg) in chlorobenzene (1 mL). The second consisted of P3HT (18 mg), PCBM (6 mg), and C_{60} (6 mg) in chlorobenzene (1 mL). Intermediate compositions were prepared by mixing different ratios of these two stock solutions. Therefore all films possess the same P3HT content, but varying PCBM:C_{60} content. These differences are reflected by labeling the relative weight fraction of the fullerene phase comprised of PCBM (e.g., 75:25 PCBM:C_{60} refers to 75 wt% PCBM and 25 wt% C_{60} in the fullerene phase). Films were spin-coated onto clean glass slides at 1100 rpm for 60 s. Absorption spectroscopy measurements

were made over a wavelength range of 300 nm to 1000 nm using a Thermo Scientific Evolution 300 UV-Vis spectrophotometer. Scanning electron microscopy was performed using an FEI Sirion SEM. Optical microscopy images were obtained with using a Zeiss Axiovert 40 CFL Inverted Microscope.

8.3.1.3. Fabrication and Characterization of OFETs

Coating solutions were prepared by adding a mixture (10 mg total fullerene mass) of PCBM and C_{60} in chlorobenzene (1 mL) with different PCBM:C_{60} ratios except for a 0:100 PCBM:C_{60} solution which had a lower concentration of C_{60} (5 mg) in chlorobenzene (1 mL). Heavily n-doped silicon wafers were used as substrates as well as the gate electrode. Thermally grown SiO_2 (200 nm) on the wafer acted as a gate dielectric layer. The surface of the oxide was cleaned by O_2 plasma for 4 min, coated with dilute benzocyclobutene (BCB; 1:20 vol/vol in mesitylene) by spin-coating (3 krpm for 60 s) in air, and thermally cured at 250 °C on a hotplate for 2 h under argon environment. PCBM:C_{60} solution was then spin-coated onto the substrate (2000 rpm for 60 s). OFETs were finished by depositing 35 nm thick gold electrodes through a shadow mask defining a transistor channel with a width of 1000 μm and a length of 100 μm. Electrical characteristics of OFETs were measured by using an HP4145B semiconductor parameter analyzer under nitrogen.

8.3.1.4. Fabrication and Characterization of OPVs

ITO-coated glass substrates were cleaned *via* a series of ultrasonic baths in a mild detergent, deionized water, acetone, and isopropyl alcohol. The substrates were removed from the last bath and dried using N_2. They were then treated with air plasma for 10 min under vacuum (200

mTorr). Once clean, substrates were coated with filtered PEDOT:PSS. The PEDOT:PSS was spin-coated, in air, on top of the ITO surface from solution to obtain a layer roughly 40 nm thick. All solar cells maintained the same P3HT:fullerene weight ratio as was used for the open film microscopy studies. Active layer solutions were stirred at 60 °C overnight in an inert atmosphere and filtered before use through a 250 nm PTFE syringe filter. These solutions were spin-coated at 1000 rpm for 60 s onto the PEDOT:PSS layer. 100 nm of aluminum was deposited *via* thermal evaporation under high vacuum ($\approx 2 \times 10^{-6}$ torr). The devices were then annealed at 150 °C for varying times under nitrogen. Aging at 90 °C was also carried out under nitrogen. The completed devices were immediately tested in air upon their completion using a 100 W m^{-2} calibrated AM 1.5 light source.

8.3.2. Additional Figures

GISAXS measurements were acquired using Anton Paar SAXSess small angle x-ray scattering instrument. The sample to detector distance was calibrated (260.2 mm) and samples were run in point collimation. Figure 8.6 shows the GISAXS data collected from P3HT/fullerene films with 100:0 PCBM:C_{60} ratio.

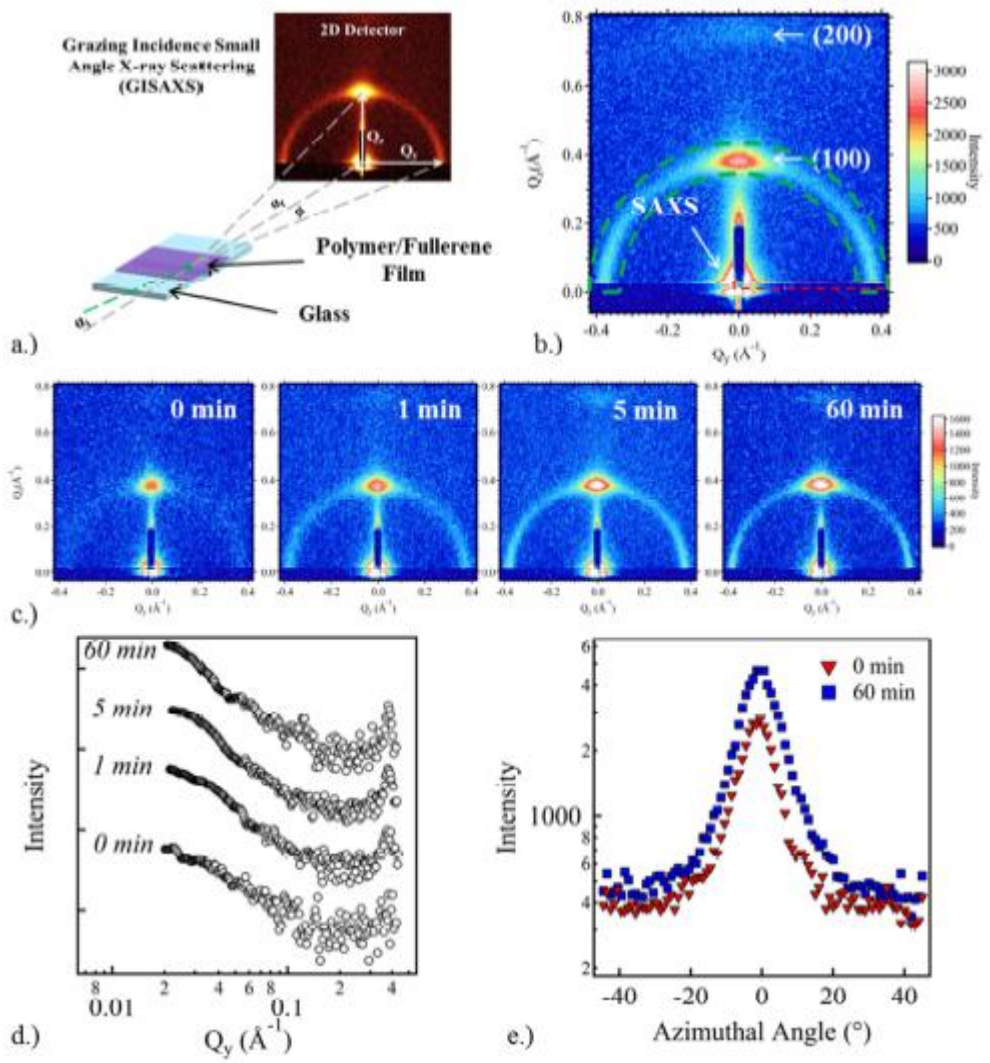

Figure 8.5 a.) Schematic of Grazing Incidence Small Angle X-Ray Scattering (GISAXS) measurements on blended films (αi=0.2°), b.) Representative GISAXS pattern for P3HT/fullerene blended film after annealing showing the typical P3HT (100) and (200) reflections and the off-specular small angle scattering signal, c.) 2D scattering patterns from P3HT/fullerene blends annealed at 150°C with 100/0 PCBM:C60 in the fullerene phase as a function of annealing time, d.) horizontal line cuts at Qz = 0.025 Å^{-1} (red box in Figure S.1.b) from the 2D profiles at the critical angle of the film showing changes in the in-plane structure of the films, and e.) radial integrations showing intensity vs. azimuthal angle of the (100) Bragg diffraction peak corresponding to the P3HT crystals (green arc in Figure S.1.b).

The samples were measured with an incident angle (α_i) of 0.2°. This is between the critical angles of the film ($\alpha_{c,film}$=0.16°-0.18°) and the underlying glass substrate ($\alpha_{c,glass}$=0.22°) and therefore is in the dynamic regime where the distorted-wave Born approximation is necessary for theoretical treatment of the data.[100] There are two main visible features in the 2D patterns that

can be used to analyze the nanostructures within P3HT:fullerene blends: *1.)* the small angle scattering intensity in the off-specular plane, which can be characterized by a horizontal line cut along the Q_y direction at constant Q_z at the Yoneda peak, and *2.)* the (100) crystal plane of P3HT crystallites that can be analyzed using a radial average at a constant magnitude of the scattering vector Q = 0.375 $Å^{-1}$.[101, 102] The results of these averages are shown in Figure 8.6.d and 8.6.e, respectively, as a function of annealing time for a P3HT:fullerene blend with 100:0 PCBM:C60 in the fullerene phase. For cuts at constant Q_Z = 0.026 $Å^{-1}$, we obtain primarily information about the lateral order of structures in the films. Figure 8.6.d shows that, as annealing time increases, the scattering profiles systematically shift towards lower angles and the intensity at low Q increases. This is consistent with the increases in size of the fullerene domains, located within the bulk heterojunctions that are observed in SEM and optical microscopy (Figure 4.2). The averages in Figure 8.6.e show that the overall P3HT crystal fraction increases with increasing annealing time and that the P3HT crystal fibers have strong preferential ordering parallel to the substrate surface.

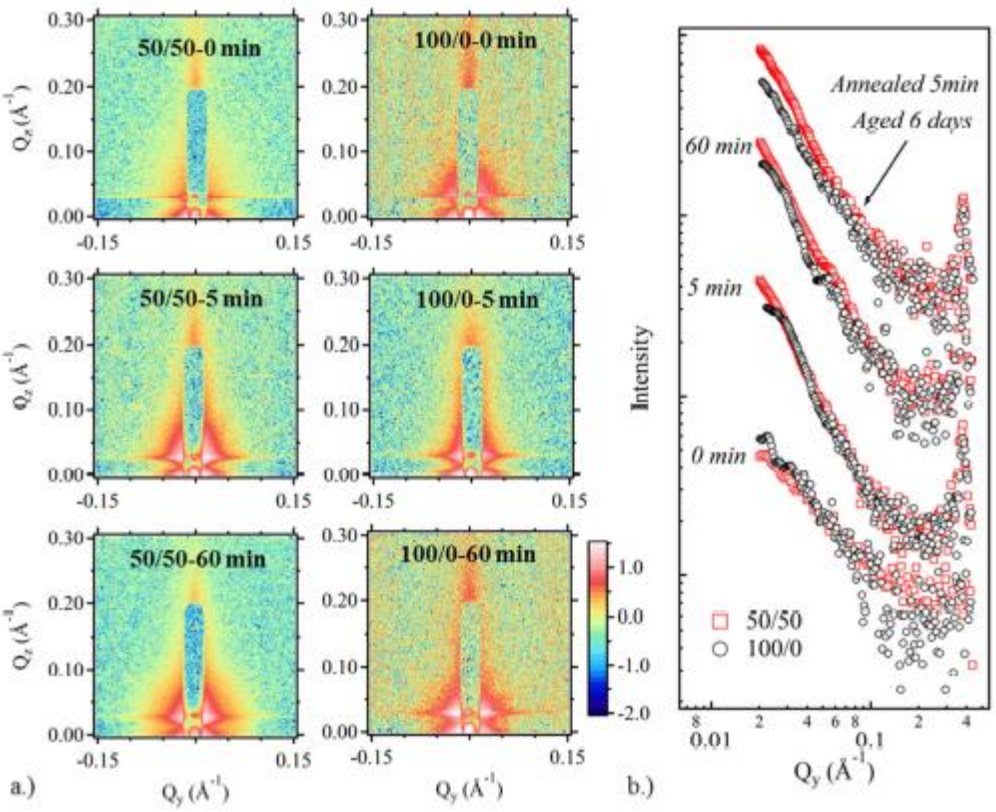

Figure 8.6 a.) 2D scattering patterns from P3HT:fullerene blends annealed at 150°C with 100:0 and 50:50 PCBM:C_{60} in the fullerene phase as a function of annealing time, b.) horizontal line cuts at Q_z = 0.026 Å^{-1} obtained from the 2D profiles showing the development of aggregates in the polymer matrix for both annealed and aged films with 100:0 and 50:50 PCBM:C_{60} in the fullerene phase.

GISAXS also provides a possible explanation for why the 50:50 PCBM:C_{60} blend outperforms a 100:0 PCBM:C_{60} blended film in terms of thermal stability at long times. Based on the horizontal line cuts shown in Figure 8.7.b, it is clear that for long annealing times and extensive aging, the 50:50 blends still maintain smaller fullerene aggregates than that of the 100:0 blend. This suggests that more P3HT:fullerene interface is also maintained as a result of the formation of smaller fullerene crystallites that are induced from the presence of C_{60}. These observations are also consistent with the SEM and microscopy observations. From the 2D profiles it is also clear that the off specular scattering intensity at small angles is larger for samples containing C_{60} impurities after annealing and aging. This implies that smaller aggregates are present in these

films. Unfortunately, the lowest Q values that can be accessed with our GISAXS are quite limited. Therefore, this technique is unable to characterize any aggregate growth once it exceeds more than ~45 nm.

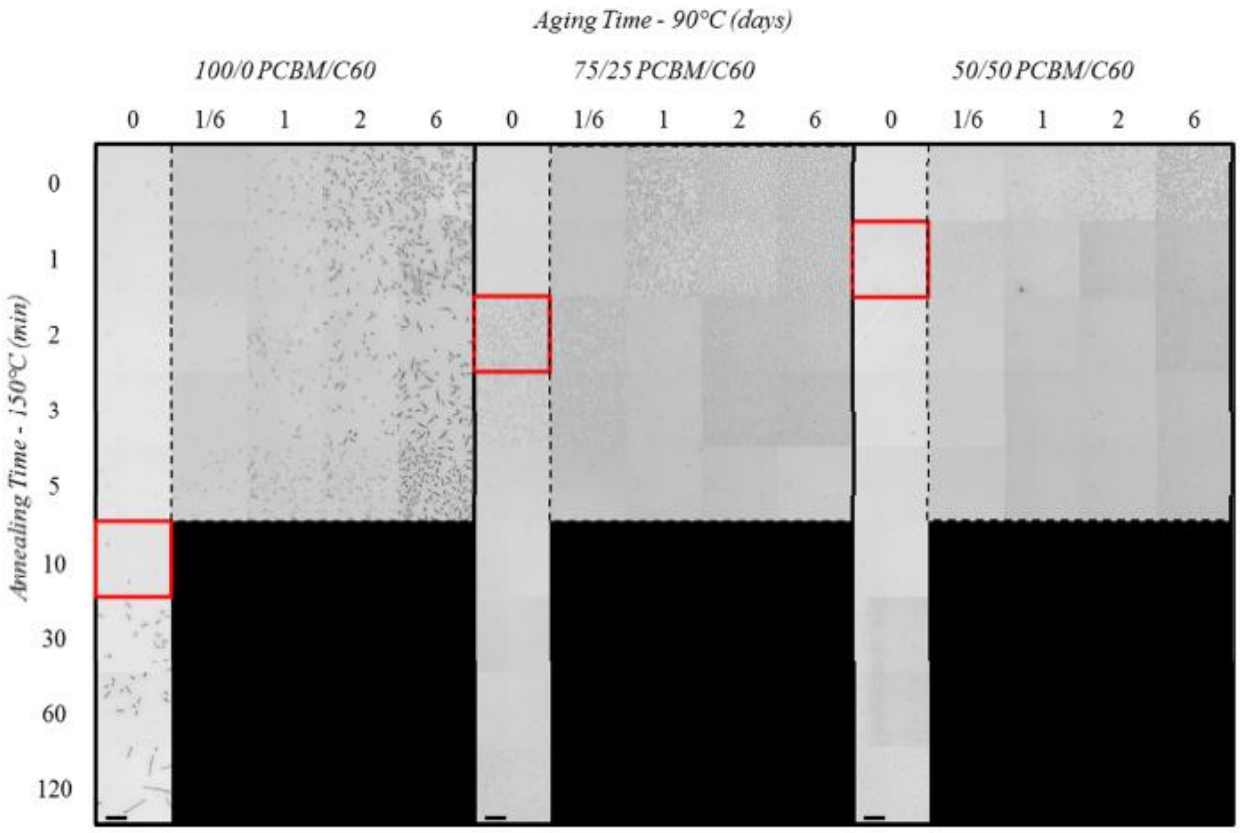

Figure 8.7 Optical micrograph array of annealing time and aging time studies. Grey boxes show regions not tested. The images outlined in represent the annealing time at 150°C where micronsized fullerene crystallites first become visible. The regions highlighted by the dotted gray boxes are films aged at 90°C. *(Scale Bar is 50 µm)*

8.4. Benzo[2,1-b;3,4-b']dithiophene-Based Low Bandgap Polymers for Photovoltaic Applications

8.4.1. Experimental

8.4.1.1. Materials and Synthesis

5,8-Dibromo-2,3-diphenylquinoxaline, 4,7-dibromobenzothiadiazole, 3,3′-diiodo-2,2′-bithiophene, 2,5-di(2-ethyldecyl)-3,6-bis(5-bromothiophen-2-yl)pyrrolo[3,4-c]-pyrrole-1,4-dione, and 5,7-dibromo-2,3-diphenyl-thieno[3,4-b]pyrazine were prepared according to the literature.[20] Unless otherwise stated, reagents were obtained commercially and used without further purification. Dry THF and toluene were obtained from an Innovative Technology, Pure Solv MD-2 solvent purification system.

8.4.1.2. Device Fabrication

BHJ solar cells were fabricated using PBDPTP, PBDPDPP, PBDPBT, and PBDPQU. Devices were made using ITO-coated glass substrates (15 Ω m^{-2}). Once cleaned, substrates were coated with PEDOT:PSS (Clevios PVP Al 4083) in air to obtain a layer ~40 nm thick. These films were annealed in air at 140 °C for 10 min. The active-layer solution contained a 1:1 polymer:PCBM (American Dye Source ADS61BFB) ratio (by weight), dissolved in 1,2-dichlorobenzene at 10 mg mL^{-1} of polymer. Active-layer deposition was completed via spin coating at 1000 rpm for 60 s in argon. Next, electrodes were deposited on top of the active layer via thermal evaporation. A 1 nm layer of LiF, followed by a 100 nm layer of Al were evaporated under vacuum (2×10^{-6} Torr) to form the electrodes. Finally, devices were annealed in argon at 140 °C for 10 min. Devices were made with both $PC_{71}BM$ and $PC_{61}BM$.

OFETs were fabricated as typical top-contact bottom-gate devices on silicon substrates. Heavily doped p-type silicon <100> substrates from Montco Silicon Technologies with a 500 ± 5 nm thermal oxide layer acted as a common gate with a dielectric layer as well as the substrate. After cleaning the substrates by sequential ultrasonication baths in acetone, methanol, and isopropyl alcohol for 10 min, the substrates were treated by air plasma. Polymer thin films were deposited

from a 5 mg/mL o-DCB solution by spin coating (1000 rpm for 60 s). Interdigitated source and drain electrodes (W = 9000 μm, L = 90 μm) made of gold (50-nm thick) were deposited on top of the polymer active layer by thermoevaporation at 1.0 Å/s through a shadow mask from a resistively heated Mo boat under high vacuum (5.0×10^{-7} Torr). After electrode deposition, devices were thermally annealed at 140 °C for 10 min.

8.4.1.3. Device Characterization

The J–V characteristics of OPVs were immediately tested after processing was completed. This was done in air using a Keithley 2400 source measurement unit and an Oriel Xenon lamp (450 W). An AM1.5 filter was used as the light source. Calibration of the light intensity was completed using a standard silicon solar cell with a KG5 filter. A light intensity of 100 mW/cm^2 was used throughout this study. At least 24 devices were tested under each set of processing conditions.

The devices were tested under nitrogen as p-type FETs using an Agilent 4155B semiconductor parameter analyzer. The source, drain, and gate electrodes of the devices were connected to the parameter analyzer using thin pin electrodes. Transfer curves were generated and analyzed for each sample. At least six devices were analyzed to generate the average mobility values reported in this article.

8.4.1.4. Imaging

AFM phase images were taken on a Veeco multimode AFM with a nanoscope III controller in tapping mode. Film thicknesses were also measured using a simple scratch test. The AFM tips used for this study were purchased from Veeco: model RTESP, phosphorus-doped Si tips.